Winter 12-15-2016

Novel contrasts in photoacoustic tomography

Ruiying Zhang
Washington University in St. Louis

Recommended Citation

Zhang, Ruiying, "Novel contrasts in photoacoustic tomography" (2016). *Engineering and Applied Science Theses & Dissertations*. 216.
https://openscholarship.wustl.edu/eng_etds/216

WASHINGTON UNIVERSITY IN ST. LOUIS

School of Engineering and Applied Science
Department of Biomedical Engineering

Dissertation Examination Committee:
Lihong V. Wang, Chair
Mark A. Anastasio
Gregory Lanza
Jin-Moo Lee
Jung-Tsung Shen

Novel Contrasts in Photoacoustic Tomography

by
Ruiying Zhang

A dissertation presented to
The Graduate School
of Washington University in
partial fulfillment of the
requirements for the degree
of Doctor of Philosophy

December 2016
St. Louis, Missouri

Table of Contents

List of Figures

List of Tables

Acknowledgments

I would like to express my sincere thanks to my advisor Prof. Lihong V. Wang, for his support, patience and guidance throughout all these years. It has been my great honor to be his student, and to learn the importance of an open and curious mind, a positive attitude, and great self-discipline in scientific endeavors. I have also received generous help and enormous support from Optical Imaging Lab members, including Konstantin Maslov, Bin Rao, Terence Wong, Junjie Yao, Junhui Shi, Lidai Wang, Lei Li, Chi Zhang, Chiye Li, and Yong Zhou. Their ingenuity and hard work have been a constant inspiration and encouragement to my research. Without them, I would not have accomplished my work.

I am gratefully indebted to my committee members, Dr. Gregory Lanza, Dr. Mark Anastasio, Dr. Jung-Tsung Shen and Dr. Jin-Moo Lee, for their guidance. Specially, I thank Dr. Gregory Lanza for his warm encouragement all the time. I thank Dr. Mark Anastasio for his valuable advice on my rotation project in my first year. I thank Dr. Jin-Moo Lee for the guidance on applying PAM for neural imaging. I also thank Dr. Jung-Tsung Shen for his advice on my research directions.

Last but not the least, I owe special thanks to my friends and family for their unconditional love, trust and encouragement, which have made this dissertation possible and the whole process rewarding.

Ruiying Zhang

Washington University in St. Louis

December 2016

Dedicated to my family

ABSTRACT OF THE DISSERTATION

Novel Contrasts in Photoacoustic Tomography

by

Ruiying Zhang

Doctor of Philosophy in Biomedical Engineering

Washington University in St. Louis, 2016

Professor Lihong V. Wang, Chair

Photoacoustic tomography (PAT) combines rich optical contrast and high ultrasonic resolution in optically scattering tissue at depths. Taking advantage of its 100% sensitivity to optical absorption, PAT has been widely applied to structural, functional and molecular imaging, with both endogenous and exogenous contrasts, at superior depths than pure optical methods. This dissertation explores novel absorption contrast mechanisms of PAT based on optical/thermal patterns, endogenous cellular chromophores, nanoparticles, small-molecule dyes and genetically-encoded proteins. With these novel contrasts, the proof-of-concept applications of PAT have been extended to include homogenous flow measurements, targeted angiogenesis imaging and therapy, label-free white blood cell imaging, 3D-whole-organ cell nuclei imaging with a subcellular resolution, and *in vivo* neural activity imaging with voltage/calcium-sensitive indicators.

Specifically, Chapter 1 introduces photoacoustic microscopy (PAM) and photoacoustic computed tomography (PACT) systems and discuss the motivation of the dissertation.

Chapter 2 describes two photoacoustic (PA) flow measurement methods with optical and thermal patterns, which are applicable to homogenous flowing medium. In the first method, a Doppler frequency shift in PA signals of the flow was detected and used to calculate flow speeds. In the

second method, unique features in an externally imposed thermal pattern of the flow, captured by repeated B-scans along the flow direction with a PAM system, revealed different flow speeds.

Chapter 3 explores the unique PA contrast of macrophages, an important type of white blood cells. Macrophages were imaged by PAM without any label, and their measured PA spectrum was distinctive from the hemoglobin spectrum, so they can be potentially differentiated from red blood cells in the blood stream. Next, with a microtomy-assisted PAM system, cell nuclei distribution in whole organs, including mouse brain and mouse lung, were imaged with subcellular resolution.

Chapter 4 introduces a type of target copper nanoparticles, which are less expensive and more biocompatible than its counterpart gold nanoparticles. The PA signals of neovasculature in the mouse flank were enhanced by the αvβ3-targeted copper nanoparticles. Moreover, the work shows the first example of a systemically targeted antiangiogenic drug delivery with a photoacoustic contrast nanoparticle *in vivo*.

Chapter 5 demonstrates the voltage imaging capability of PA. A voltage sensitive dye with sufficient signal change was discovered and used as a PA voltage indicator for the first time. The mechanism was characterized through both PA imaging and spectroscopic methods. Its use was explored in a mouse epilepsy model and cortical electrical stimulation model *in vivo*. Finally, the deep imaging potential of PA was realized by imaging the voltage response of cells under 4.5 mm thick slice of rat brain tissue using a PACT system.

Chapter 6 proves the neural calcium imaging capability of PA with a genetically encoded calcium indicator. In a fly model, I ambiguously demonstrated for the first time that PA can be used to imaging neural activities in the fly brain without the interference signals from hemoglobin. In the a live-mouse-brain-slice model, I successfully demonstrated the deep imaging capability of PA for calcium imaging by imaging through a 2-mm-thick scattering medium with a PACT system.

Chapter 1 Introduction

1.1 Introduction to Photoacoustic Tomography

In PAT, as tissues are excited by laser pulses, laser energy is absorbed by biochromophores and converted into heat through non-radiative relaxation. The heat is further converted to a pressure rise through thermoelastic expansion. The initial pressure rise propagates as an ultrasound wave in the tissue, which is referred to as a photoacoustic (PA) wave[1,2]. An ultrasonic transducer or transducer array is used to detect the PA waves, and the detected PA signals are used to reconstruct an image that maps the original optical energy deposition and tissue. By converting photons into ultrasonic waves, which are orders of magnitude less scattered, photoacoustic tomography (PAT), an emerging imaging modality, can break through the diffusion limit (~1 mm depth) by capitalizing on the low acoustic scattering in tissue. Moreover, the image resolution and penetration depth of PAT are highly scalable with ultrasonic frequency, which provides an unprecedented opportunity to bridge the gap between microscopic and macroscopic images.

Based on the image formation methods, PAT has two major implementations. The first combines mechanical scanning of a focused single-element ultrasonic transducer with direct image formation, and is commonly used in PAM. The second combines parallel detection by a multi-element ultrasonic transducer array or a mechanical/electronic scanning equivalent with image reconstruction, and is used in PACT. In both PAM and PACT, the PA amplitude is proportional to the optical absorption coefficient of the absorber in units of m^{-1}, to its non-radiative quantum yield (approximately equal to 1 – the fluorescence quantum yield if the photochemical channel is negligible), and to the local optical fluence (or exposure) in the unit of J/m^2.

1.2 Motivation

By using endogenous contrasts, PAT can provide structural and functional information, based on the absorption of DNA & RNA[3], cytochromes[4], hemoglobin[5], melanin[6], and lipids[7] at optical wavelengths ranging from ultra-violet (UV) to near-infrared. Among these absorbers, hemoglobin and melanin have relatively strong absorption coefficients, and they have been widely used in the study of cancer and hemodynamic-related parameters. Relatively weak absorbers at the visible wavelength, such as DNA/RNA and cytochromes, have been much less explored. However, their untapped potential could be fundamental for building a complete picture of tissue properties and dynamic physiological processes. Discovering more endogenous contrasts and advancing endogenous-contrast-based PAT to preclinical/clinical research are major goals of this work.

While endogenous contrasts are useful tools, they provide access to a limited range of biomedical applications[8]. Exogeneous contrasts, including nanoparticles, dyes, and genetically-encoded proteins, can enable the visualization of biological processes of interest and are still highly desired. In the imaging of exogenous contrasts, endogenous contrasts often serve as the background signals, making it difficult to distinguish them. Therefore understanding the merits of exogenous contrasts, and the difficulty they present, is a rewarding and challenging topic.

This dissertation aims to address the need and challenges presented above, and explore novel contrasts of PAT based on both endogenous and exogenous contrasts.

Chapter 2 Photoacoustic Flowmetry in Homogenous Media

This chapter describes techniques for homogenous flow measurement. When the absorber is at high concentration or its size is small enough, it cannot be resolved spatially due to the limited bandwidth of the transducer. With previous flow measurement methods, the medium was considered to be a static homogenous continuum[9]. In this chapter, we develop methods to measure the flow speed of a homogenous medium, and demonstrate PA Doppler effect in a homogeneous medium and the feasibility of calculating the flow speed based on a thermal pattern encoded in blood flow *in vivo*. Work in this chapter has been published in Applied Physics Letters[9] and Optics Letters[10].

2.1 Structured-illumination Photoacoustic Doppler Flowmetry of Axial Flow in Homogeneous Scattering Media

2.1.1 Background

Flow speed measurement plays an important role in biomedical research, such as the study of tumor and cardiovascular diseases. In biomedical imaging, Doppler ultrasound flowmetry[11,12], laser Doppler flowmetry[13] and Doppler optical coherence tomography[14] are all valuable tools for flow speed measurement. However, based on backscattered signals, these Doppler techniques require particle heterogeneity in the flowing medium[11-14], thus they cannot be used for flow measurement of a homogeneous medium. In comparison, photoacoustic imaging, based on optical absorption contrast[15], is not intrinsically limited by the heterogeneity of the flowing medium. A few recent studies have investigated photoacoustic Doppler (PAD) flowmetry of particle-based phantoms[16-23]. It has been reported that the traditional PAD signal strength decreases and eventually diminishes as the particle concentration increases[24,25]. In this paper, we propose a new flow measurement method based on the PAD effect in homogeneous media, where the distance between absorptive molecules is on the level of nanometers. Different from traditional PAD implementations, which use a temporally modulated CW or tone-burst laser excitation, our method uses a spatially modulated pulsed laser excitation to temporally modulate the received PA signals. The modulation frequency of the received PA signals is determined by the acoustic transit time between the neighboring pitches of the spatial modulation. Therefore, the flow of the medium changes the acoustic transit time and thus induces a frequency shift in the received PA signals. As in traditional PAD flow measurement[16-23,26,27], the flow direction determines the sign of the frequency shift.

In PA flow measurement of a homogeneous medium, a stationary ultrasonic detector receives signals from the excited region of the medium, which is the acoustic source. As shown in Figure 1(a), if both the acoustic source and the medium are stationary, the PA wave from the stationary acoustic source travels to the transducer surface at the speed of sound in the medium (~1480 m/s in water at $20\,°C$). If both the acoustic source and the medium are moving, the received PA signal will be compressed or stretched, depending on the flow direction. In the time domain, this compressing or stretching effect can be further decomposed into two parts: the arrival time shift induced by the moving medium and the signal duration scaling induced by the moving source. In the frequency domain, while the arrival time shift corresponds to the phase shift at each frequency, the signal duration scaling corresponds to the scaling of the frequency spectrum. Both the arrival time shift and the signal duration scaling can be used to measure flow speed. However, using the arrival time shift requires exact knowledge of the sound path between the acoustic source and the transducer, which is challenging to achieve in biological tissues. By contrast, the signal duration scaling relies only on the acoustic property of the moving source, even if the sound path between the source and ultrasonic transducer is uncertain. In this study, we explored four methods of PAD flowmetry of homogeneous media: (1) central frequency shift; (2) arrival time shift; (3) phase change at each frequency; (4) temporal scaling.

2.1.2 Methods

Central Frequency Shift Similar to traditional PAD flow measurement, if the PA signal generated by the moving source has a central frequency with a narrow bandwidth, then the scaling of the spectrum can be represented by its central frequency shift, from which the medium's flow speed and direction can be derived. In our method, the modulation frequency f_0 can be estimated as

$$f_0 = v_a / d_0 , \tag{2.1}$$

where v_a is the speed of sound in the stationary medium, d_0 is the fringe pitch of the spatially-modulated illumination.

Then, the central frequency shift can be expressed as

$$f_{PAD} = f_0 \frac{v_m}{v_a} , \tag{2.2}$$

where v_m is the flow speed of the medium projected along the acoustic beam axis. A positive frequency shift means the medium is flowing towards the transducer, and vice versa. Note that the PAD frequency shift in Eq. (2.2) is only half of the traditional ultrasound Doppler shift, due to the one-way emission of the PA signals. In practice, the central frequency of the PA signal can be estimated as the power-weighted mean frequency.[19, 20]

Arrival Time Shift This method is predicated on the assumption that both the flow speed and acoustic property along the path are uniform. The time shift Δt_m can be estimated by cross-correlation between the received PA signal $p_1(t)$ at flow speed v_1 and the PA signal $p_0(t)$ at a baseline flow speed v_0. If the flight time of the signal is much longer than its duration (i.e., the distance from the center of the illumination spot to the transducer is much larger than the size of the illumination spot), the contribution of the signal duration to the cross-correlation can be neglected. Thus, by finding the time delay Δt_m that maximizes the cross-correlation between $p_1(t)$ and $p_0(t)$, the relative flow speed Δv_m can be calculated as follows:

$$\Delta t_m = \underset{\Delta t}{argmax} \int_0^{t_{\max}} p_0(t) p_1(t + \Delta t) dt \ , \tag{2.3}$$

$$\Delta v_m = {v_a}^2 \frac{\Delta t_m}{L}, \tag{2.4}$$

where $t_{\max}$ represents the ending point of the signal and L is the distance between the transducer and the center of the illumination spot. A positive arrival time shift means the medium is flowing away from the transducer, and vice versa.

Phase Change Alternatively, in the frequency domain, the phase information of the cross-spectral density function of the signal can also be used to calculate the time delay Δt_m.[21] We have

$$\Delta t_m = \frac{1}{2\pi f} argS_{p_1 p_0}(f), \tag{2.5}$$

where $S_{p_1 p_0}(f)$ is the cross-spectral density of the received signals $p_1(t)$ and $p_0(t)$. After extracting the phase from $S_{p_1 p_0}(f)$, we can then fit for the arrival time shift Δt_m using Equation (2.5) and calculate the flow speed using Equation (2.4).

Temporal Scaling In the time domain, in addition to the approximate calculation method based on cross-correlation, the flow speed can also be estimated by a more accurate temporal scaling method. The scaling factor ε_m that maximizes the product of $p_1(\varepsilon_m t)$ and $p_0(t)$ can be calculated using Equation (2.6), and the flow speed is given by Equation (2.7):

$$\varepsilon_m = \underset{\varepsilon}{argmax} \int_0^{t_{\max}} p_0(t) p_1(\varepsilon t) dt, \tag{2.6}$$

$$\Delta v_m = (1 - \varepsilon_m) v_a \ . \tag{2.7}$$

A temporal scaling factor less than one means the medium is flowing towards the transducer, and vice versa.

2.1.3 Results

Here, photoacoustic flow sensing based on the PAD effect from a homogeneous medium was demonstrated in a laboratory setup, shown in Figure 2.1(b). A pump (Model 3386, Fisher Scientific and EW-72008-00, Cole Parmer) drove the flow in a clear PVC tube (ClearFlexTM 60 premium, 8 mm inner diameter) immersed in water. Nanosecond laser pulses of 570 nm wavelength were focused by a cylindrical lens (300 mm focal length), which generated a 3-mm-long illumination line along the tube axis. A Ronchi ruling (50 µm pitch size) was placed above the tube, which provided a spatial modulation of the illumination intensity. A diluted red ink solution (optical absorption coefficient: $\mu_a \approx 1.2$ cm^{-1}) was used as the flowing medium. The generated photoacoustic waves propagated in the flowing medium and were detected by a flat ultrasonic transducer (V2022 BC, Olympus-NDT). The distance between the illumination spot and the transducer surface was approximately 5.6 cm. The PA signals from the transducer were amplified by 40 dB and then sampled by an oscilloscope (TDS5034, Tektronix, Inc.). The recorded PA signals were averaged for 256 times. In a second experiment with a scattering medium, the tube was immersed in a 0.1% intralipid solution (optical scattering coefficient: $\mu_s \approx 6.18$ cm^{-1} at 570 nm). [22]

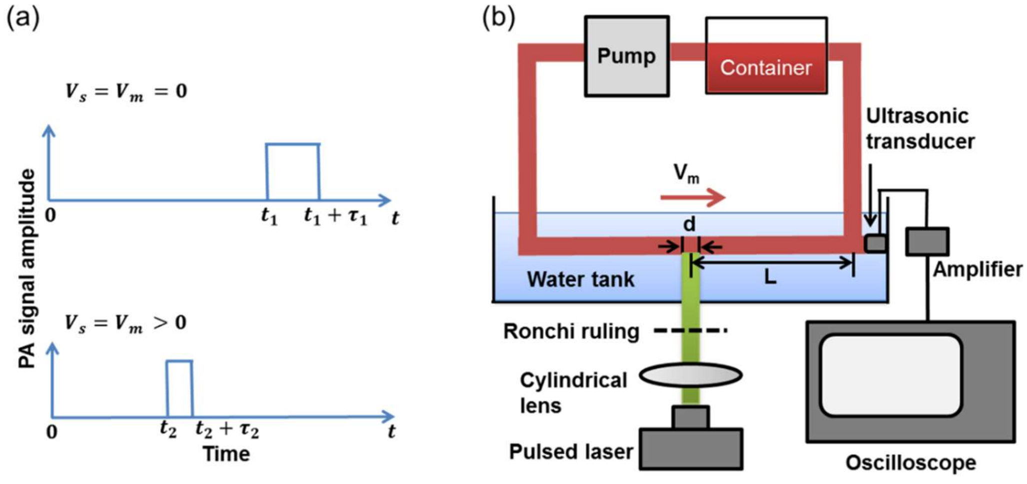

Figure 2.1 Flow measurement based on the PAD effect in a homogeneous medium. (a) Schematic of PA signals under different flow conditions. v_s and v_m are the flow speeds of the source and the medium,

respectively; t_1 and t_2 are the arrival times of signals under the two flow conditions; τ_1 and τ_2 are the signal durations under the two flow conditions. Both the arrival time and the signal duration decrease when $v_s = v_m > 0$ (flow is towards the transducer), compared with when $v_s = v_m = 0$. (b) Schematic of experimental setup. The homogenous flow with speed v_m is excited by structured illumination, and the generated PA signal is detected by a flat ultrasonic transducer placed in the axial direction of the tube. L is the distance between the illumination spot and the transducer surface, and d is the illumination spot size.

Figure. 2.2(a) shows the temporal profile of a typical photoacoustic signal from a stationary homogeneous medium, where the signal modulation is clear. The arrival time was about 37.5 μs, which corresponded to a distance of ~5.6 cm between the illumination spot and the transducer surface. The total duration of the signal was about 2 μs, which corresponded to an illumination spot size of ~3 mm. As shown in Figure. 2.2(b), a faster flow (0.63 m/s) of the medium towards the transducer induces a shorter arrival time of the signal than a slower flow (0.16 m/s), producing a time shift in the temporal profile of the received PA signal. Correspondingly, Figure. 2.2(c) shows the frequency spectrum of the PA signal acquired at a flow speed of 0.63 m/s. The signal has a central frequency of 29.8 MHz with a full-width at half maximum of 9.7 MHz. According to Eq. (2.2), the central frequency is related to the spatial modulation frequency of the illumination pattern, the propagation speed of sound in the homogeneous medium. The bandwidth is determined by the duration of the PA signal, which is also related to the propagation speed of sound in the medium. A faster flow of the medium towards the transducer shortens the signal duration and increases the central frequency of the received PA signal, as shown in Fig. 2.2(d).

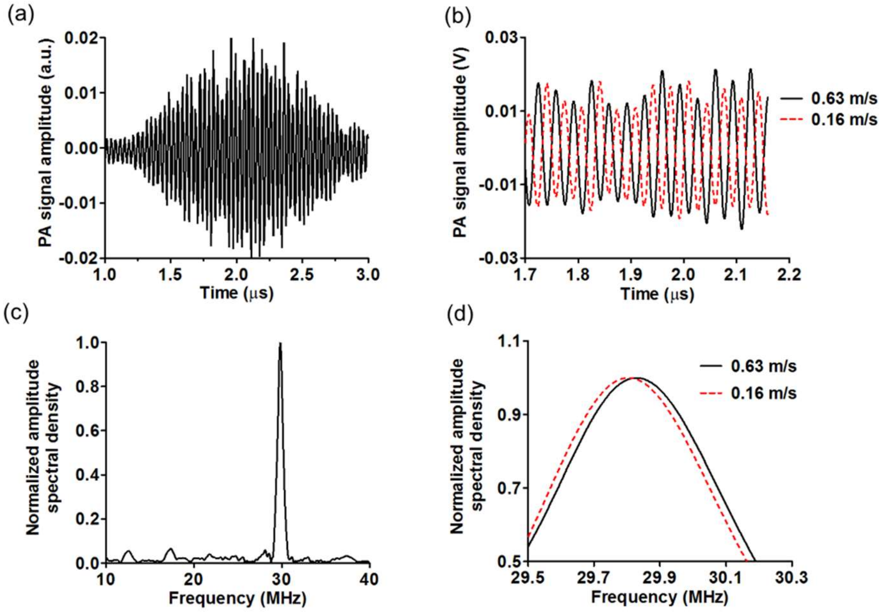

Figure 2.2 Representative PA signals in the time and frequency domains. The laser spot size was 3 mm, and the distance from the transducer surface to illumination spot was 5.6 cm. (a) Representative time-domain PA signal with zero flow speed, where the signal modulation is induced by the Ronchi ruling. (b) Close-up of the PA signals at flow speeds of $v_1 = 0.63$ m/s and $v_2 = 0.16$ m/s. (c) Representative PA signal spectrum at flow speed $v_1 = 0.63$ m/s with a central frequency at 29.8 MHz. (d) Close-up of the frequency spectra at flow speeds $v_1 = 0.63$ m/s and $v_2 = 0.16$ m/s.

In the first experiment, with the tube immersed in water, the flow speed of the ink solution was varied from 0.020 m/s to 1.4 m/s. The four methods introduced above were used to calculate the flow speeds. As shown in Figure 2.3, the measurements from all four methods agree well with the preset speeds. The root-mean-square-errors (RMSE) of the four methods were 0.089 m/s, 0.095m/s, 0.10 m/s, and 0.057 m/s, respectively.

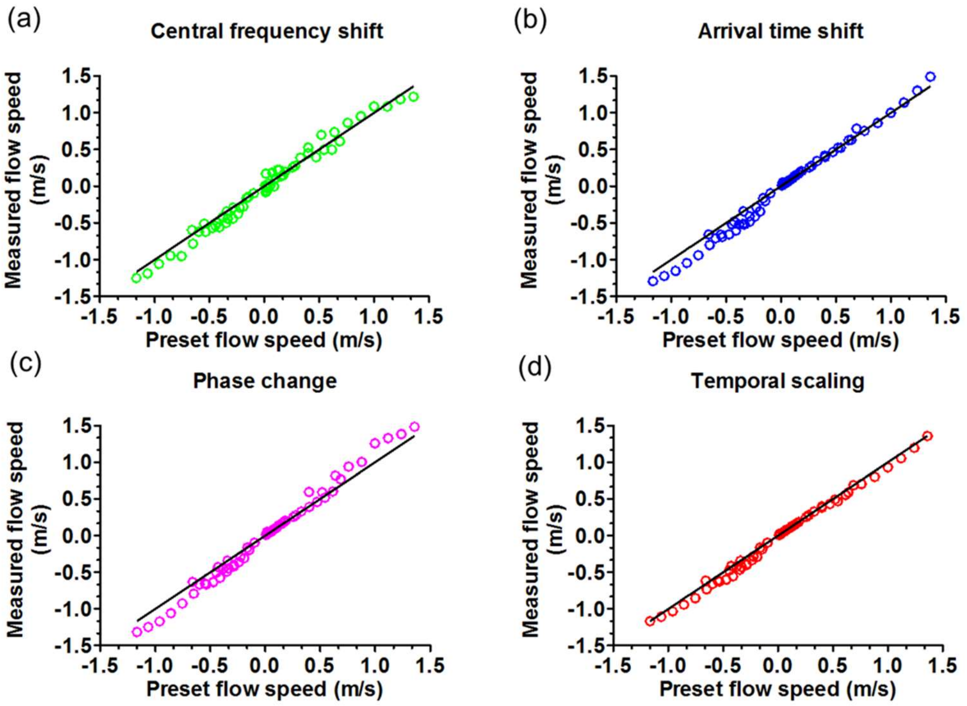

Figure 2.3 Flow speed measurements in a clear medium, based on four different methods. Solid lines: $y = x$. (a) Flow speed measurement based on central frequency shift, with $RMSE = 0.089$ m/s. (b) Flow speed measurement based on arrival time shift, with $RMSE = 0.095$ m/s. (c) Flow speed measurement based on phase change versus frequency, with $RMSE = 0.10$ m/s. (d) Flow speed measurement based on temporal scaling, with $RMSE = 0.057$ m/s.

In addition to the clear medium, PA flow measurements were also demonstrated in an intralipid scattering medium. The intralipid solution above the tube surface was ~3 mm thick. The flow speed was varied from 0.13 m/s to 0.63 m/s. The temporal scaling method and the central frequency shift method were used for flow speed quantification, as shown in Figure. 2.4. Compared with the measurements in the clear medium, the measured flow speeds in the scattering medium had greater errors for both methods. For the time domain method, optical scattering reduced the signal-to-noise ratio (SNR), which resulted in a greater error in the temporal scaling measurement (RMSE: 0.066 m/s). For the frequency domain method, in addition to the reduced

SNR, the scattering also degraded the PA signal modulation depth, thereby increasing the difficulty in measuring the central frequency (RMSE: 0.12 m/s).

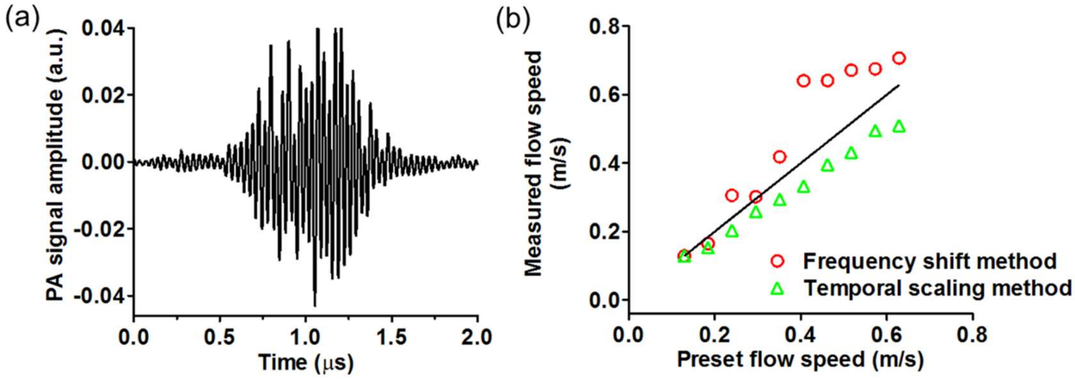

Figure 2.4 Photoacoustic flow measurement in a 0.1% intralipid solution. (a) PA signal in the time domain. (b) Flow speed measurements based on the central frequency shift method and temporal scaling method, with $RMSE = 0.12$ m/s and 0.066 m/s, respectively. Solid line: $y = x$.

Based on the translation and scaling properties of the Fourier transformation, the time shift in the time domain is equivalent to the phase shift in the frequency domain, and scaling in the time domain is equivalent to scaling in the frequency domain. Nevertheless, superior to the other three methods, the central frequency shift method can sense the absolute flow speed instead of a relative flow speed. Furthermore, the central frequency shift method does not assume uniform flow and homogeneous acoustic property along the sound path between the laser spot and the transducer surface. Instead, it requires only uniformity within the illumination spot, which is much easier to satisfy in practice.

It should be noted that the proposed method assumes a uniform flow speed over the depth direction of the tube that the laser can penetrate. However, this is not true for laminar flow, where the center of the tube has the fastest flow. For the absorption coefficient of the ink solution, the 1/e penetration depth of the light was approximately 8.3 mm, larger than the tube diameter. Therefore, the measured flow speed was an average of the actual flow distribution.

The modulated light illumination provides a central frequency for the received PA signal, which can help quantify the absolute flow speed. It transforms the otherwise wideband PA signal into a narrowband signal. Without the light modulation, the wideband spectrum would be compressed or stretched as well, depending on the flow direction. The scaling factor can also be used to estimate flow; however, it can detect only relative flow speeds.

In the central frequency shift method, the maximum measurable flow speed is limited by the frequency response of the transducer and SNR. Assuming the maximum frequency response of the transducer is ~105 MHz, the maximum measurable flow speed is ~ 3700 m/s (flow is towards the transducer), using Equation (2.2). Increasing the bandwidth of the transducer can increase the maximum measurable flow speed. However, since the acoustic signal is attenuated more at higher frequencies, higher frequency components have lower SNR, which will limit the maximum measurable flow speed.

The minimum measurable flow speed, which is the velocity sensitivity of the system, is limited by the signal length and SNR. Increasing the cycle number of the Ronchi ruling can improve the frequency resolution, and thus decrease the minimum measureable flow speed. In addition, zero-padding can be used in the Fourier transformation to improve flow sensitivity. While zero-padding cannot actually improve the frequency resolution, it can smooth the frequency spectrum and thus improve the accuracy of locating the central frequency.[23] If the noise is spectrally white, the minimum measurable flow speed can be derived from the Cramér–Rao lower bound, which gives an estimation accuracy of the central frequency as [24,25]

$$\sigma_f^2 = \frac{3f_s^2}{\pi^2 N(N^2 - 1)SNR}, \tag{2.8}$$

$$v_{\min} = 2\sigma_f v_a / f_0 , \tag{2.9}$$

where σ_f is the standard deviation of the central frequency computed from the measured PA spectrum, f_s is the sampling frequency, N is the number of sampling points, f_0 is the modulation frequency, v_a is the speed of sound within the medium, and $SNR = A^2/2\sigma_n^2$ (A is amplitude of the signal and σ_n^2 is the variance of the noise). In our experiment, given $SNR = 10000$, $N = 10^4$, and $f_s = 2.5$ GHz, we get $v_{\min} = 0.014$ m/s.

In conclusion, we have proposed a flow speed measurement method based on the photoacoustic Doppler effect in a homogeneous medium. Unlike the back-scattering based Doppler method, our method does not require heterogeneity of the flowing medium on the scale of the spatial resolution. As long as the medium is optically absorptive at a certain wavelength, such as pure water in the infrared region, its flow speed can be measured based on the photoacoustic Doppler effect. Although we emphasized the central frequency shift method, the other three methods can also be utilized for relative flow speed calculation. While the current experimental setup is more suitable for fast flow (>2.0 cm/s) measurement, the slow flow measurement capability can be improved, for example, by increasing the modulation frequency.

2.2 *In Vivo* Optically Encoded Photoacoustic Flowmetry

2.2.1 Background

Blood flow is an important physiological parameter and can be used to identify abnormal cell activities, such as hypermetabolism in cancers[28]. Major non-invasive blood flow measurement techniques include Doppler ultrasound flowmetry[12], laser Doppler velocimetry[17], and Doppler optical coherence tomography. All of these techniques rely on acoustic or optical scattering contrasts from moving media. Based on optical absorption contrast, photoacoustic (PA) microscopy has been recently applied to high-resolution blood flow imaging. In comparison to other techniques, PA microscopy provides inherently background-free detection and speckle-free imaging[19]. Several PA flow measurement techniques based on the PA Doppler effect have been explored[23,29,30], but it has been reported that the PA Doppler signal strength decreases as the particle concentration increases[30,31]. Additionally, the axial resolution achieved by tone-burst excitation with a continuous-wave (CW) laser was relatively low compared with the axial resolution achieved by pulsed excitation. Unlike the previous methods based on the PA Doppler effect, Sheinfeld et al. measured the flow speed based on PA detection of thermal clearance[32]. This method does not reply on the inhomogeneity of the absorbers in the flow, and thus can potentially measure the flow speed of homogenous media. However, the method was unable to separate thermal convection from conduction, leading to low accuracy for slow flow measurements.

Recently, ultrasound-encoded photoacoustic flowmetry has been demonstrated[26,33]. Based on a similar idea, we present here an *in vivo* optically encoded PA flowgraphy (OE-PAF) capable of high-resolution flow speed measurement of a homogeneous medium. As a heating source, an intensity-modulated CW laser—acting as a “writing” beam—generates temperature variations within the flowing medium. A pulsed laser is used as a “reading” beam to generate PA waves, which are detected by a confocally aligned ultrasonic transducer. Since PA signals are sensitive to the local temperature, the heated area generates higher PA signal amplitudes than nearby regions. By scanning the reading beam along the flow direction, we can acquire PA images of the flow that has been photothermally encoded by the writing beam. This method offers three advantages. First, the modulation of the heating beam can be changed to generate different patterns, i.e., we can “write” different “barcodes” into the flow, allowing the heating pattern to be optimized for the best contrast-to-noise ratio. Second, both the photothermal encoding and the PA detection employ endogenous optical absorption contrasts; thus, OE-PAF is label-free. Third, since OE-PAF directly measures the displacement of the encoded flowing medium, thermal diffusion does not directly impact the measurement. Therefore we do not need to calibrate the thermal diffusivity.

2.2.2 Methods

Mathematically, we assume that the temperature at the origin $x = 0$ is modulated by a sinusoidal heating beam, with a function $H(t)$:

$$H(t) = H_0 \sin(2\pi f_0 t) \tag{2.10}$$

where H_0 is a constant, f_0 is the heating frequency, and t is the heating time. The PA measurement is performed by linearly scanning the PA detection spot along the flow direction, i.e., an imaged blood vessel of interest. Along the motor scanning direction, the temperature change induced by the heating beam can be described as

$$\Delta T(x, t_b) = \Delta T_0(x) \sin\{2\pi f_0 [t_b - t_0 - x / (v_f \cos\theta)]\} \tag{2.11}$$

where $\Delta T_0(x)$ is the amplitude of the temperature change, x is the distance from the heating point to the PA measurement point, t_b is a point on the B-scan (cross-sectional scan) time axis, $2\pi f_0 t_0$ is the initial phase of the heating sinusoidal function (t_0 is a constant), v_f is the flow speed, and θ is the angle between the flow velocity and motor scanning velocity vectors. The amplitude of the detected PA signal, V, generated by the pulsed laser excitation, is proportional to the local pressure rise, which can be described by [1]

$$V(x,t_b) \propto [\gamma_0 + \gamma'_0 \Delta T(x,t_b)]\mu_a(x)F(x), \tag{2.12}$$

where γ_0 and γ'_0 are empirical constants related to the Grueneisen parameter, $\mu_a(x)$ is the optical absorption coefficient, and $F(x)$ is the optical fluence of the reading beam. Thus the time-variant part of the PA signal detected by the transducer can be written as

$$\tilde{V}(x,t_b) = \gamma'_1(x)\mu_a(x)F(x)\sin\{2\pi f_0[t_b - t_0 - x/(v_f\cos\theta)]\} \tag{2.13}$$

where $\gamma'_1(x) = \Delta T_0(x)\gamma'_0$. If the motor scans at a constant speed v_m, equation (2.13) becomes

$$\tilde{V}(x,t_b) = \gamma'_1(x)\mu_a(x)F(x)\sin\{2\pi f_0 t_b[1 - v_m/(v_f\cos\theta)] - 2\pi f_0 t_0\}. \tag{2.14}$$

Equation (2.14) shows that, due to the blood flow and the motion of the transducer, the frequency of the heating pattern has become $[1 - v_m/(v_f\cos\theta)]f_0$; thus the frequency shift from the heating frequency is

$$\Delta f = -\frac{v_m}{v_f\cos\theta} f_0. \tag{2.15}$$

When $v_m = v_f\cos\theta$, the PA signal becomes time-invariant:

$$\tilde{V}(x, t_b) = -\gamma'_1(x)\mu_a(x)F(x)\sin(2\pi f_0 t_0). \tag{2.16}$$

At position x, the PA signal amplitudes vary with the heating time t, which can be described as

$$\tilde{V}(x, t) = \gamma'_1(x)\mu_a(x)F(x)\sin\{2\pi f_0[t - t_0 - x/(v_f \cos\theta)]\}. \tag{2.17}$$

By performing cross-correlation between the time-variant PA signals at positions x_1 and x_2, the time delay Δt between the two signals can be calculated as follows:

$$\Delta t = \arg\max_{\Delta t'} \int_0^{t_{meas}} \tilde{V}(x_1, t)\tilde{V}(x_2, t + \Delta t')dt \tag{2.18}$$

where t_{meas} is the total measurement time. It can be seen that Δt is related to the flow speed as well as the motor scanning speed, a relationship which can be expressed as

$$\Delta t = \frac{\Delta x}{v_f \cos\theta} - \frac{\Delta x}{v_m} \tag{2.19}$$

where $\Delta x = x_2 - x_1$. If $v_m >> v_f \cos\theta$, or if we assume signals in the same B-scan are acquired at the same time point, then when $\theta = 0^\circ$, Equation (2.19) can be reduced to

$$v_f = \frac{\Delta x}{\Delta t} \tag{2.20}$$

2.2.3 Results

Figure 2.5(a) is a schematic of the experimental setup. A second-generation optical-resolution photoacoustic microscopy system (OR-PAM)[34] imaged the heat propagation. A pulsed laser beam (532 nm) with a spot size of ~2 μm was focused onto the sample. The generated PA signals were detected by an ultrasonic transducer with a central frequency of 50 MHz. To achieve high sensitivity, the ultrasound focus was coaxially and confocally aligned with the optical focus. The B-scan rate was 8.3 Hz over a transverse range of 3 mm with 1600 A-lines. An intensity-modulated CW laser light (532 nm wavelength; MLL-III-532, General Optoelectronic) with a spot size of ~0.4 mm heated the flow medium to generate temperature variation. The CW laser (100 mW) was intensity-modulated at 0.5 Hz. The maximum distance between the heating and detection beam was 3 mm, jointly limited by thermal diffusion, signal-to-noise ratio, and scanning range of the PAM system used in the experiment. The minimum distance between the two beams was zero when the centers of the two beam spots coincide. A tube (300 μm inner diameter, VWR® International) filled with red ink solution was connected to a syringe. Flow speeds were set by a syringe pump (BSP-M99, Braintree Scientific Inc.). Figure 2.5(b) is a schematic of an OR-PAM scan for thermal flow measurement in a tube.

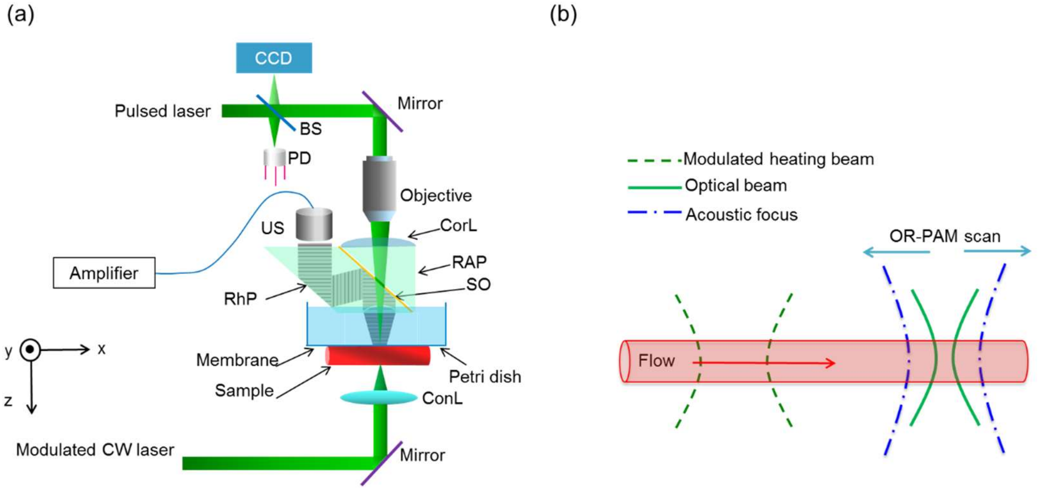

Figure 2.5 Schematic of optically encoded photoacoustic (PA) flowgraphy. (a) Schematic of second-generation OR-PAM system. BS, beam splitter; CCD, charge-coupled device; ConL, condenser lens; CorL, correction lens; CW, continuous wave; PD, photodiode; ; RAP, right-angle prism; RhP, rhomboid prism; SO, silicone oil; US, ultrasonic transducer; . (b) Schematic of OR-PAM scan for thermal flow measurement in a tube.

As shown in Figure 2.6(a), the PA amplitudes from a tube image without heating were relatively evenly distributed. Figure 2.6(b) shows space-time PA images acquired with heating on at three different flow speeds. The images in Figure 2.6(b) were obtained after subtracting the signals averaged over the total measurement time. To increase the signal-to-noise ratio (SNR), the PA images were averaged over 8 heating cycles. From Figure 2.6(b), it can be seen that the PA signals were modulated by a sinusoidal wave both at the scanning axis (denoted by x) and the heating time axis (denoted by t), as indicated by Equation (2.14) and Equation (2.17). Along the heating time axis of the thermal pattern, the slope of the pattern, $\Delta t / \Delta x$, is the inverse of the flow speed, $1/v_f$, as indicated by Equation (2.20). Thus it can be inferred that the slope was steeper for slower flow speeds, and vice versa.

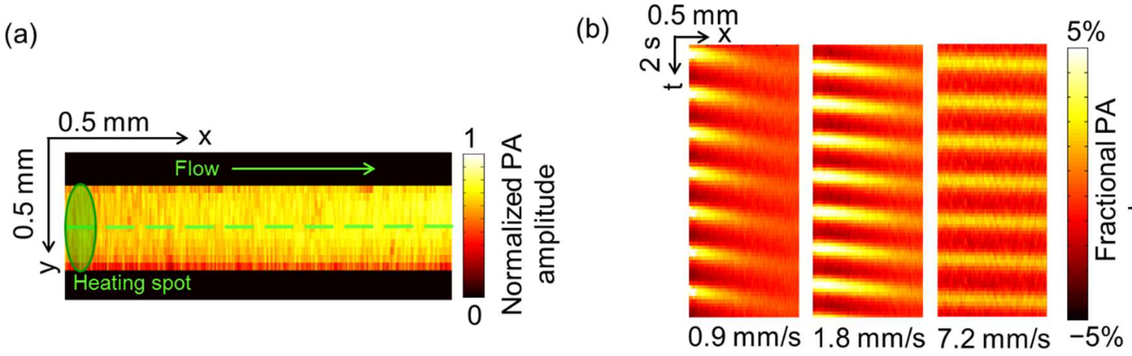

Figure 2.6 PA flow images of ink solution in a tube with a modulated heating frequency of 0.5 Hz. (a) Maximum-amplitude projection (MAP) image of a silicone tube filled with red ink solution. Dashed line: B-scan range. (b) Representative space-time images of a tube along the dashed line in (a) at different flow speeds.

During heating, the maximum PA amplitude was 10.8% greater than the average PA amplitude, corresponding to a 2.2 ºC temperature rise (room temperature 20 °C)[1]. During the measurement, the flow speeds were varied from 0.23 mm/s to 11.00 mm/s. The measured flow speeds were shown in Figure 2.7. The straight line is a linear fit of the measurement points with a fitting equation of $y = kx$. The coefficient k was found to be 0.998. The measurement errors were estimated using the normalized RMSD, which was 2.0%

.

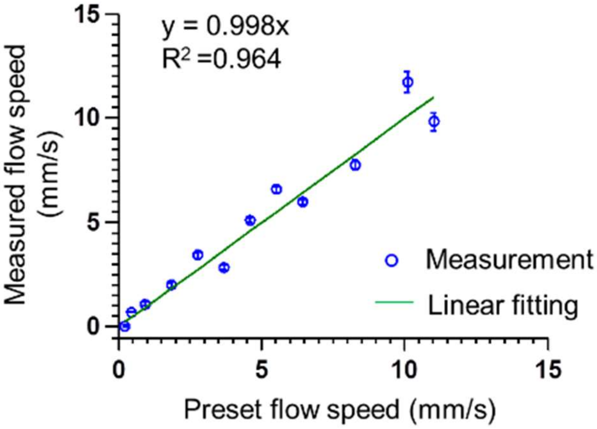

Figure 2.7 Measured flow speeds based on optically encoded PA flowgraphy in a silicone tube. Modulated heating frequency: 0.5 Hz. Error bars represent standard errors. N = 10 for each flow speed.

In vivo blood flow measurement was conducted in a nude mouse ear. The heating frequency was 0.5 Hz. The signals were averaged over 16 heating cycles to increase the SNR. Figure 2.8(a) shows a MAP image of a mouse ear. The diameter of the vessel of interest is about 100 µm. The motor scanned from A to B. We used an arbitrary-trajectory scanning technique[35], so that B-scans could follow the paths of curved blood vessels. The heating spot was located at position B. The space-time PA image of the heating pattern is shown in Figure 2.8(b). The image was obtained after the signals averaged over the total measurement time were subtracted. By comparing the signals between position A and position B (marked by the dashed line), we calculated the time delay, from which we determined the flow direction as from position B to position A. Then using Equation (2.20), the flow speed in the mouse ear was calculated to be 0.90 mm/s. During heating, the maximum PA amplitude was 6.6% greater than the average PA amplitude, corresponding to a temperature rise of 2.5 ºC (a body temperature of 37 °C was assumed)[1]. In a second *in vivo* experiment, the dynamic change in the PA amplitude from the mouse ear vessels was imaged with 0.1 Hz heating. The area near the heating spot shows stronger PA amplitude during the heating duty cycle, verifying the thermal effect. The 2D imaging frame rate was 1 Hz over a $0.8\times\ 1.6\ \text{mm}^2$ area, using a MEMS-PAM system[36]. All the animal experimental procedures were in conformance with the laboratory animal protocol approved by Washington University in St. Louis.

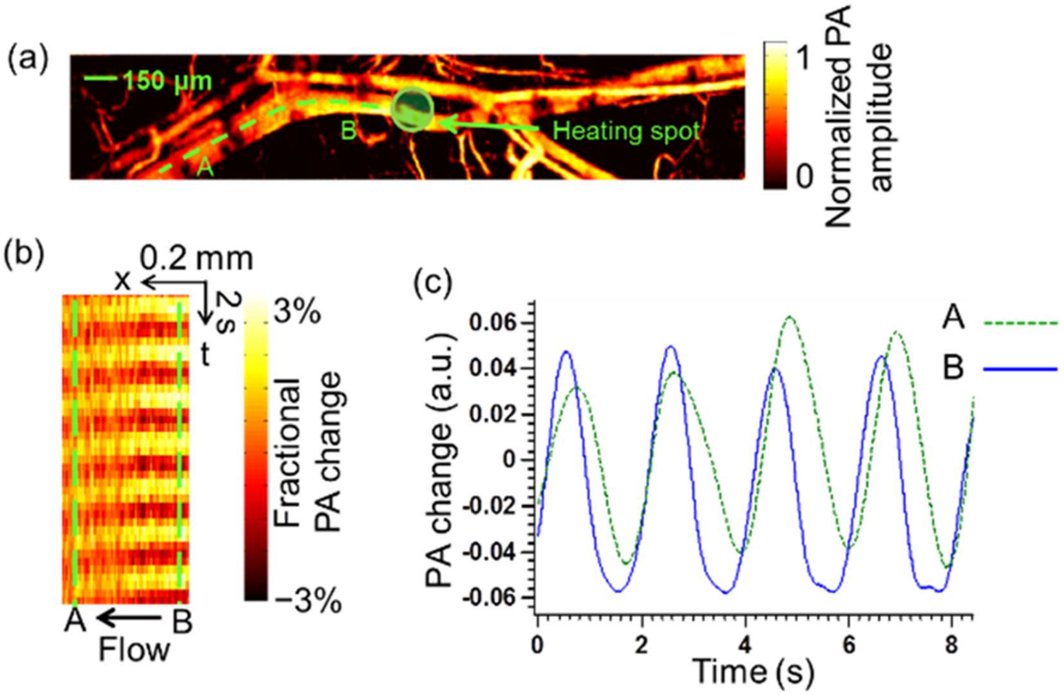

Figure 2.8 *In vivo* flow measurement in a mouse ear with a modulated heating frequency of 0.5 Hz. (a) PA image of vessels in a mouse ear. A, starting point for B-scan following the curvature of the vessel. B, ending point of B-scan. Dashed line, B-scan range. (b) Space-time image along the dashed line in (a). (c) PA signal change with time at point A and B.

To achieve repeating heating patterns with sufficient contrast-to-noise ratio, before the next heating cycle, the heating pattern “written” in the previous cycle has to flow fast enough to get out of the original heating spot. i.e., $(v_f \cos\theta)\cdot T \le d$, where T is the heating period and d is the heating spot size. Given $d = 0.4$ mm, $T = 2$ s, and $\theta = 0^\circ$, then $v_f \le 0.2$ mm/s. From the equation, it can be seen that decreasing the heating frequency and minimizing the heating spot size could reduce the minimum measureable flow speed. Increasing the sensitivity of the PA system and improving the contrast-to-noise ratio of the heating pattern (e.g., by increasing the heating power) could make the minimum measurable flow speed closer to the theoretical value. Contrariwise, thermal diffusion could smooth out the heating pattern and decrease the contrast-to-noise ratio, which would increase the minimum measurable flow speed.

From Equation (2.19), it can be inferred that the time delay Δt should be positive, i.e., $\Delta t = \frac{\Delta x}{v_f \cos\theta} - \frac{\Delta x}{v_m} > 0$, thus $v_f \leq v_m / \cos\theta$. For our current experimental setup, $v_m = 25$ mm/s, $\theta = 0^\circ$, and thus the maximum measurable flow speed is 25 mm/s.

Though the current experiment setup used a CW laser to generate the sinusoidal thermal pattern, the heating beam could also come from a pulsed laser, and different heating functions could be applied as long as adequate contrast-to-noise ratio is achieved. Note that the proposed method is sensitive to all thermal carriers and can be applied to homogeneous media. With the current setup, the heating beam and detection beam are on the opposite sides of the sample, imposing limitations on the thickness and absorbance of the sample. In the future, an improved setup with the two beams at the same side could be utilized.

In summary, we present an optically encoded photoacoustic flowgraphy *in vivo*. In this method, the flow was encoded by a thermal pattern. Then, we “read” the pattern using an optical-resolution photoacoustic microscopy system. The flow speed was calculated from PA images by cross-correlation. The proposed technique enabled high-resolution measurement of flow speed as slow as 0.23 mm/s in phantoms and *in vivo* measurement of blood flow in a mouse ear.

2.3 Conclusions

For homogenous flow measurement, we encoded the flow with structured illumination and with a thermal pattern to create a “virtual” contrast for PA flowmetry. We “read” the grating pattern and the thermal pattern with an ultrasonic transducer. The calculated difference between the original pattern we input and the pattern “read” by the transducer was generated by the flowing medium. These methods do not require the presence of absorbers with sizes larger than the system resolution. Although demonstrated *in vivo* in the mouse ear, the applications of the proposed methosd are limited to shallow flow media due to the limited depth that can be reached by the structured illumination or the thermal pattern induced by the CW laser.

Chapter 3 Photoacoustic Microscopy of Cells with Endogenous Contrasts

Photoacoustic microscopy has been widely used for structural and functional imaging based on the absorption contrast of red blood cells. In this chapter, we demonstrate the feasibility of label-free imaging of one type of white blood cells, macrophages, which play an important role in the immune system. We also extend the previous study of cell nuclei imaging of thin samples to 3D whole organ imaging with subcellcular resolution. The cell nuclei imaging is based on the joint work of Terence Wong and Chi Zhang.

3.1 Label-free Photoacoustic Imaging of Macrophages

3.1.1 Background

Macrophages play key roles in host defense, removing cellular debris generated during tissue remodeling, and rapidly and efficiently clearing cells that have undergone apoptosis [37]. Some macrophages, called wandering macrophages, travel throughout blood and lymph streams to reach infectious sites and kill microbes. Others are stationed at critical locations in the body, such as the lymph nodes, bone marrow, spleen, and liver. In diseased tissues, the number of macrophages can increase profoundly. Thus the ability to quantitatively monitor macrophages in lymph flow and to image tissue macrophages (their density, flux rates, function, and subtypes) is important in the diagnosis and treatment of cancer, atherosclerosis, and myocardial infarction. The optical absorption of white blood cells (including macrophages, monocytes, and lymphocytes) is much weaker than that of red blood cells, thus they are often regarded as negative contrast for photoacoustic imaging. While numerous photoacoustic imaging studies are based on the absorption of hemoglobin[19], and some studies focus on the imaging of white blood cells (macrophages) with exogenous biomarkers, label-free photoacoustic imaging based on the intrinsic absorption of macrophages has not been performed. It should be noted that although a spectrophotometer can measure the optical absorption spectrum of a solution easily, it cannot provide an accurate spectrum of intact cells. Here, using an optical resolution transmission-mode photoacoustic system, we explored the intrinsic absorption of macrophages over the visible spectrum range, and monitored the flow of macrophages in a phantom tube. With multiple wavelengths, it is possible to differentiate macrophages from red blood cells in the blood stream, or to spectrally identify them in the lymph flow, which can be used for macrophage monitoring and cell counting *in vivo*. In diseased tissues, photoacoustic imaging of the distribution and density of macrophages may provide helpful information to physicians for the diagnosis and therapy of diseases.

3.1.2 Methods

Mouse macrophage RAW264.7 cells from the American Type Culture Collection were cultured in Dulbecco's modified Eagle's medium supplemented with 10% fetal bovine serum at 37 °C in a 5% CO_2 air atmosphere. For PA imaging, we placed macrophages suspended in phosphate buffered saline solution (~ 20 μL) onto a microscopic glass slide. To study flowing macrophages, the macrophages suspended in the phosphate buffered saline solution were circulated by a syringe pump in a silicone tube (300 um ID, VWR Inc.).

An integrated diode-pumped Q-switched laser and optical parametric oscillator system (NT 242-SH, Ekspla) generated laser pulses (5 ns pulse width, 1 kHz repetition rate) with a tunable wavelength range from 210 to 2600 nm. The laser pulses were sequentially filtered by an iris (2 mm aperture), focused by a condenser lens, filtered by a 50 µm pinhole, and focused again by an objective. The objective for visible light (460715, Zeiss) had a 0.6 numerical aperture (NA). The focused laser pulse generated a spatially and temporally abrupt temperature rise, which generated photoacoustic waves through thermoelastic expansion. The photoacoustic waves were coupled by water and detected by a focused ultrasonic transducer with a 40 MHz center frequency (80% bandwidth, 0.50 NA). Then they were amplified, digitized at 1GS/s (PCI 5152, National Instruments), and finally recorded by a computer. A 2D maximum amplitude project image was formed by raster scanning the sample along the x and y directions, as shown in Figure 3.1.

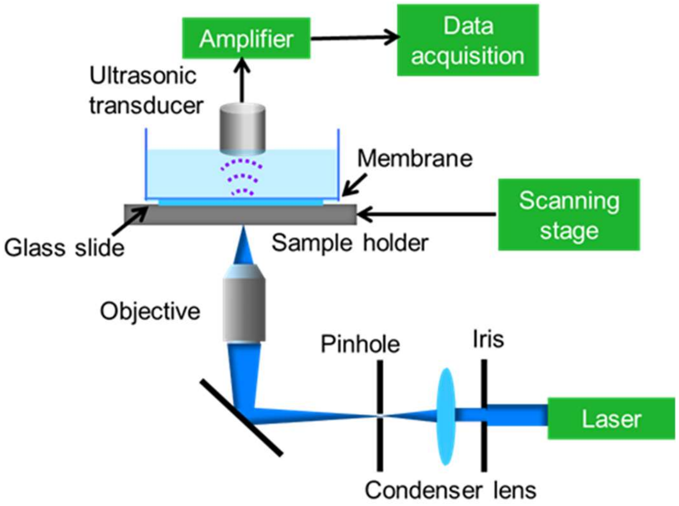

Figure 3.1 Transmission-mode PAM for multispectral imaging of macrophages.

For the spectrum measurement, the wavelength was tuned from 405 nm to 610 nm with a 5 nm step size. At every wavelength, the amplitudes of photoacoustic signals from 10^4 A-lines of macrophages on a glass slide were recorded and averaged. The standard error was calculated for each point, as indicated in Figure 3.2. To monitor flowing macrophages, m-mode at 1 kHz was used to capture the motion of the macrophages. A 2D image of macrophages in a tube was formed by converting the time axis to the distance axis.

3.1.3 Results

The normalized absorption spectrum of macrophages was calculated (Figure 3.2(a)) in the visible range, showing that the absorption peak is around 420 nm. We also compared the spectrum of macrophages with that of hemoglobin, which is a predominant optical absorber in the visible range (Figure 3.2(b)). It can be seen that the spectra of macrophages, oxy-hemoglobin, and deoxy-hemoglobin have very distinctive spectrum peaks, indicating the potential of photoacoustics to spectrally distinguish them in diseased tissue or in lymph flow. Individual macrophages fixed on a microscopic glass slide can be clearly visualized as a circular shape by the transmission-mode photoacoustic system, as shown in Figure 3.3. Flowing macrophages were imaged using M-mode as shown in Fig. 3.4. The cross-sections of two flowing macrophages can be observed in the tube at 1 kHz imaging rate.

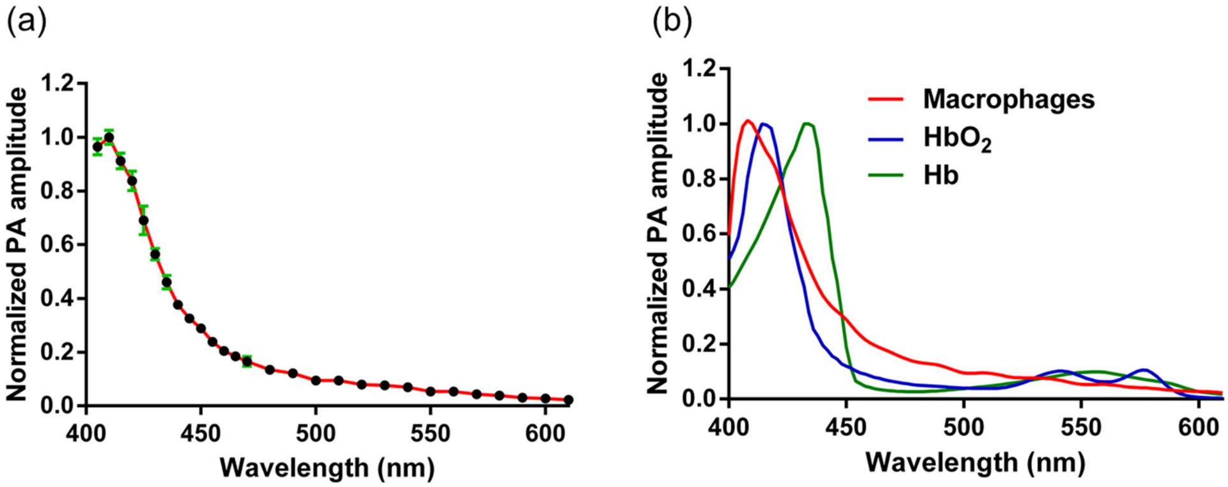

Figure 3.2 Photoacoustic spectrum of live macrophages. (a) Normalized photoacoustic spectrum of macrophages from 405 nm to 610 nm. (b) Normalized photoacoustic spectra of macrophages, oxy-hemoglobin, and deoxy-hemoglobin. The spectra of oxy- and deoxy-hemoglobin are from the reference[38].

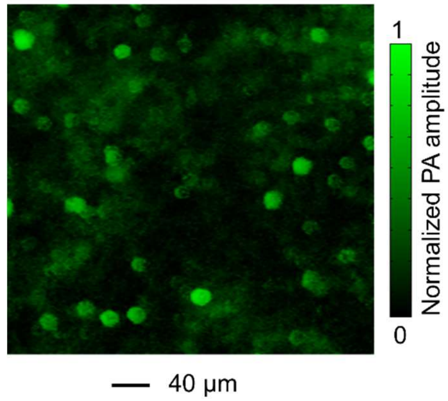

Figure 3.3 PAM at 420 nm of macrophages fixed on a microscopic glass slide

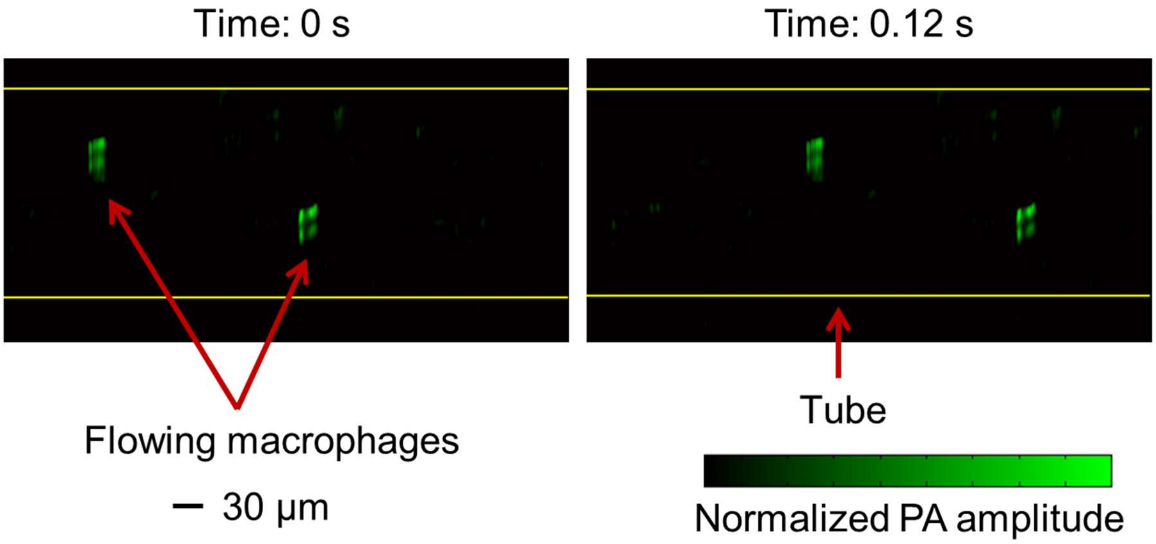

Figure 3.4 Cross-sectional images of macrophages flowing in a silicone tube. The macrophages were suspended in a phosphate buffered saline solution.

In conclusion, the absorption spectrum of macrophages was characterized using a transmission-mode photoacoustic microscope system. Based on the spectrum information, the macrophages could be potentially spectrally differentiated from red blood cells because they have a distinctive absorption spectrum from that of the deoxy- and oxy-hemoglobin. The imaging of flowing macrophages also indicates the possibility of monitoring macrophages in the lymph flow *in vivo*, which will be a value tool for clinical applications in the future.

3.2 Label-free Microtomy-assisted Photoacoustic Microscopy of Whole Organs

3.2.1 Background

Histologic analysis of tissue has been widely used in both preclinical and clinical settings because it can provide information about the tissue down to the organelle level. To acquire histology images of a thick sample (e.g., a whole organ from a mouse) requires sectioning of the sample before imaging by optical microscopes. The registration of the images from different slices performed after the imaging often leads to different levels of inaccuracy and distortion of the volumetric image despite rectification efforts [39-44]. Also, for histology imaging, the tissue needs to be stained with H&E to image cell nuclei. In previous work, PAM has been used for UV imaging of cell nuclei in thin tissue samples[3,45]. It has also been shown that PAM can provide histology-like images at UV wavelengths. Here we demonstrate 3D label-free photoacoustic imaging of the cell nuceli distribution in whole organs with subcellular resolution, enabled by a microtome.

We imaged formalin-fixed mouse brain tissue and mouse lungs embedded in paraffin with microtomy-assisted photoacoustic microscopy (mPAM). In H&E staining, cell nuclei are identified by the color difference between the cell nuclei and cell cytoplasm in the histology images after staining. Similarly, in mPAM, because the cell nuclei absorbed much more strongly than the cytoplasm at the UV wavelength, cell nuceli had much stronger signals than the cytoplasm. This difference provided the photoacoustic contrast between cell nuclei and cytoplasm and enabled histology-like photoacoustic images.

3.2.2 Methods

Mouse brains and lungs were extracted from Swiss Webster mice (Hsd: ND4, Harlan Laboratories) immediately after the animal was sacrificed. Then the organs were fixed in 10% neutral-buffered formalin for several days before they were embedded in paraffin as block specimens for photoacoustic imaging. All experimental animal procedures were carried out in conformity with laboratory animal protocols approved by the Animal Studies Committee of Washington University in St. Louis.

The mPAM system (Figure 3.5) is controlled by the user through a LabVIEW program. A central controller with a real-time processor (400 MHz) and a reconfigurable field-programmable gate array receives the parameter input from the LabVIEW program and sends out a corresponding trigger to a Nd:YLF Q-switched UV laser (266 nm wavelength, 7 ns pulse width, QL266-010-O, CrystaLaser,Inc) at a 10 kHz pulse repetition rate. The laser beam is expanded by a pair of lenses and filtered by a pinhole. Then a custom-made water immersion UV objective lens with a NA of 0.16 focuses the laser beam onto the specimen. The lateral resolution defined by the optical focal spot was measured to be 0.91 μm. As the specimen absorbs the UV light, the resulting photoacoustic waves are detected by a custom-made ring-shaped ultrasonic transducer (42 MHz central frequency, 76% bandwidth). A hole in the center of the ring-shaped transducer allows the delivery of light directly to the specimen. The axial resolution of the system, determined by the penetration depth of UV light, was around 20 μm.

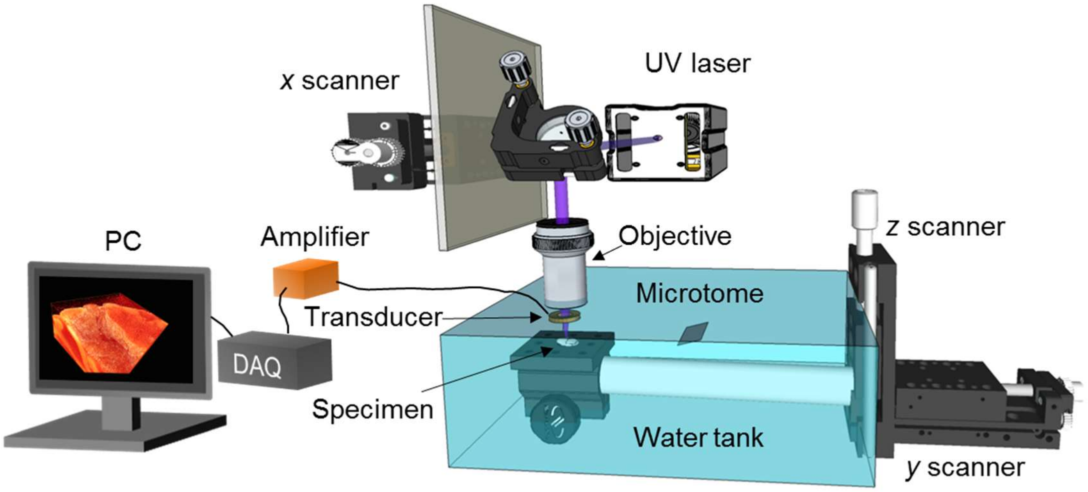

.

Figure 3.5 System schematic of microtomy-assisted PAM

The detected photoacoustic signals are then amplified and acquired by a data acquisition card. Two-dimensional raster scanning is realized by a two-axis scanning stage, which is controlled and synchronized with the laser by the central controller. After each imaging scan of the surface of the specimen, a microtome blade controlled by the central controller automatically sections the surface of the specimen while the specimen stays in the original position. The imaging and sectioning processes repeat until the entire specimen is imaged. To generate the nuclear density map, we first generated a nuclear image by Hessian filtering. Each nucleus in the image was reduced to one pixel with unit amplitude, and the background was set to zero amplitude. Then each pixel of this new image was replaced by the average of the 50 × 50 μm^2 surrounding area, creating a nuclear density map where each pixel value equaled the relative nuclear density of the 50 × 50 μm^2 surrounding area. Next, we used mPAM to image a formalin-fixed unstained mouse brain embedded in a paraffin block. The block was imaged on the surface and sectioned repeatedly and re-imaged at 20 μm thickness by mPAM. The imaged volume of 3.0 mm by 3.8 mm by 2.0 mm, which covers both the cerebrum and the cerebellum. A series of PA images were acquired at the block surface before sectioning, and a 3D volume was reconstructed without the need for image registration.

3.2.3 Results

As shown in Figure 3.6, the reconstructed 3D photoacoustic image did not present distortion artifacts or discontinuous structures, which are common problems in 3D histology. Figure 3.6(a)-(b) show the volume at different angles, with coronal and sagittal views of the mouse brain. The cell nuclei, extracted and enhanced by Hessian filtering, appear as bright dots in the images (Figure 3.6(c)).

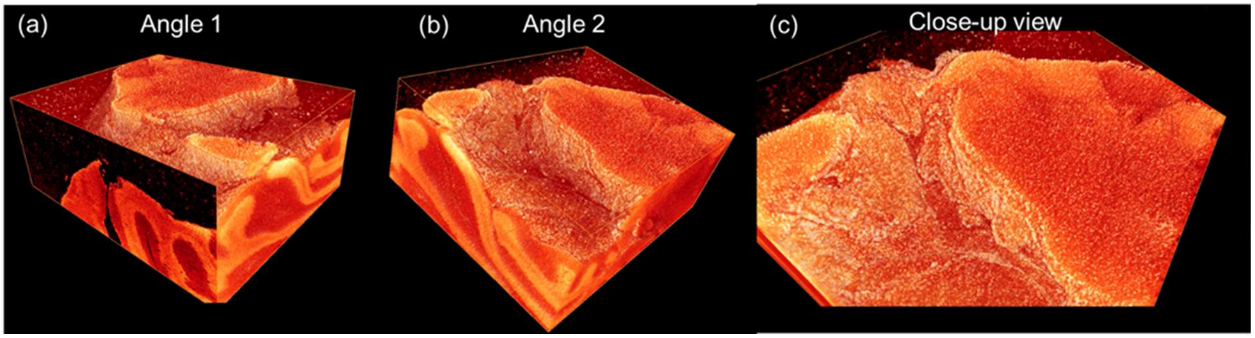

Figure 3.6 Volumetric mPAM image of a fixed mouse brain specimen embedded in a paraffin block. (a)(b) Individual cell nuclei are highlighted as bright dots and shown from different viewing angles. (c) A close-up view of the specimen shown in (b).

In addition to mouse brain sample imaging, a formalin-fixed mouse lung was embedded in paraffin and imaged by mPAM. mPAM images of mouse lung sections at different layers of the specimen show different alveoli structures (Figure 3.7). Similar to the mouse brain imaging, individual cell nuclei can be extracted (bright dots). The imaged volume was 1.5 mm by 1.0 mm by 1.2 mm, with 61 sections and a 20 μm section thickness. These results demonstrate that mPAM can provide histology-like imaging of whole organs with subcellular resolution.

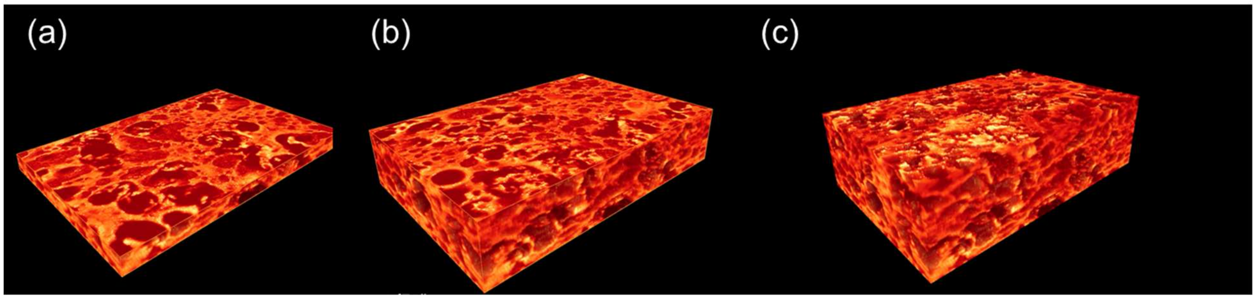

Figure 3.7 Volumetric mPAM image of a fixed mouse lung specimen embedded in a paraffin block. (a)-(c) Mouse lung specimen at different layers, revealing various alveoli features and individual cell nuclei distribution.

3.3 Conclusions

In this chapter, the imaging of macrophages demonstrates the potential of PAM to image weakly absorbing endogenous proteins within the cytoplasm in the visible range. This method can potentially be extended to other weakly-absorbing cell types. Moreover, with UV light, we demonstrated automated three-dimensional cell nuclei imaging of whole organs with subcellular resolution. When combined, the visible and UV light can potentially be used to excite any cell types for PA imaging of the cytoplasm and nuclei without staining of the specimen.

Chapter 4 Photoacoustic Neurovascular Imaging and Therapy with Copper Nanoparticles

Nanoparticles represent the largest class of contrast agents for molecular PA imaging[8]. Previously, gold nanoparticles were the main research focus. Here, we apply more biocompatible and more affordable copper nanoparticles to targeted imaging and therapy of angiogenesis. The copper nanoparticles were synthesized and provided by Dr. Gregory Lanza's lab. The work described in this chapter was published in Theranostics[46].

4.1 Background

As an important component of an expanding vascular network the neovasculature can be viewed as a biomarker of inflammation associated with tumor aggressiveness or atherosclerotic plaque progression. [47-49] To date, noninvasive imaging of angiogenesis has been essentially a preclinical endeavor, although imaging candidates have reached the clinical testing level for MRI and nuclear medicine. Nuclear medicine probes, although exquisitely specific for neovascular biosignatures, such as the $\alpha_v\beta_3$-integrin, are not specific to angiogenesis, since this adhesion molecule is activated on numerous cell types present in tumors or atherosclerotic lesions. [50-52] By comparison, MRI paramagnetic nanoparticle agents are often vascular-constrained by size and very specific for neoendothelial expression of $\alpha_v\beta_3$-integrin, but such agents have experienced other roadblocks in the clinic. [53] Photoacoustic molecular imaging offers noninvasive vascular-constrained detection of angiogenic biomarkers with very high resolution imaging of the neovasculature.

Different imaging modalities have different characteristic resolution limits, with microscopic images having the highest resolution for thin specimens. For biomedical instrumentation, ultra-high spatial resolution MRI at 3.0T and high resolution CT provide *in vivo* blood vessel images but with a poorer resolution, in the range of 200 to 500 µm, which is inadequate for discrete neovessel imaging. [54-58] Photoacoustic (PA) imaging combines the advantages of ultrasound imaging and optical imaging and offers high depth-to-resolution ratios at different spatial scales, ranging from organelles to organs, [59] as well as unique and important physiological assessments, such as differential circulating blood oxygenation levels.

Previous studies have confirmed that PA imaging's utility can be markedly extended with exogenous contrast agents. [60-62] In many instances, these contrast agents have been based on gold cubes, spheres, or rods with particle sizes greater than the renal clearance threshold (<8 to 10 nm), creating difficult translational challenges when proving long-term safety in man. Gold nanobeacons (120-160 nm) were developed to achieve the large absorption cross-sections of bigger solid gold particles by suspending a multitude of small gold nanoparticles (3-5 nm) in a hydrophobic matrix encapsulated with phospholipid (160 nm). [63] Moreover, the optical absorption wavelength of nanoparticles was tunable well into the NIR optical window, minimizing endogenous absorption and maximizing PA imaging depth.

However, the pressure of healthcare economics has placed an emphasis on driving the costs of imaging studies down, and we have thus sought lower cost biocompatible alternatives to gold. We hypothesized that nanoparticles entrapping high densities of organically soluble small molecular weight copper complexes could provide an inexpensive and effective approach to neovascular targeted PA imaging. The choice of copper as a cheaper, biocompatible alternative to gold was independently supported by a recent report describing nontargeted crystalline copper sulfide nanoparticles as PA contrast agents for deep tissue imaging at 1064 nm. [64] In this research, a soft noncrystalline $\alpha_v\beta_3$-targeted copper-oleate nanoparticle ($\alpha_v\beta_3$-CuNP) was developed and its PA imaging signal with respect to blood and the previously reported gold nanobeacons was characterized [63] as a function of NIR wavelength and with varying nanoparticle concentrations. The *in vivo* efficacy of $\alpha_v\beta_3$-CuNPs for high-resolution imaging of mouse neovasculature was examined in a Matrigel™ model of angiogenesis. Furthermore, the theranostic antiangiogenic potential of $\alpha_v\beta_3$-CuNPs incorporating a novel Sn 2 lipase-labile fumagillin prodrug (Fum-PD) was also studied. [65]

4.2 Material and Methods

Reagents Unless otherwise listed, all solvents and reagents were purchased from Aldrich Chemical Co. (St. Louis, MO) and used as received. Anhydrous chloroform and methanol were purchased from Aldrich Chemical Co. Poly(styrene-*b*-acrylic acid) (PS-*b*-PAA) was purchased from Polymer Source Inc. (Montreal, Canada). High purity egg yolk phosphatidylcholine was purchased from Avanti Polar Lipids, Inc. Cholesterol and cooper oleate were purchased and used as received from Aldrich Chemical Co. (St. Louis, MO). Sorbitan monolaurate was purchased from Aldrich. Argon and nitrogen (Ultra High Purity: UHP, 99.99%) were used for storage of materials. The Spectra/Por membrane (Cellulose MWCO: 20,000 Da) used for dialysis was obtained from Spectrum Medical Industries, Inc. (Laguna Hills, CA).

Preparation of Sn 2 lipase labile Fumagillin prodrug Synthesis of the Sn 2 prodrug was accomplished in two steps: 1) saponifying fumagillin dicyclohexylamine salt to fumagillol, and 2) esterifying the product with 1-palmitoyl-2-azelaoyl-sn-glycero-3-phosphocholine (PAzPC). [65] Briefly, fumagillin dicyclohexylamine salt (NCI) in 1:1 methanol:water was treated with 35% NaOH, stirred in an ice bath for 2 h, warmed to room temperature, treated with another equivalent of 35% NaOH, and then stirred in an ice bath until the starting material was not detected by TLC (~4 h). After evaporating the methanol and solubilizing in ethyl acetate, the mixture was extracted with 5% citric acid, brine, bicarbonate, and brine again, then dried with $MgSO_4$ and concentrated *in vacuo*. The crude product was purified with activated charcoal in acetonitrile and then filtered through a celite pad. (Yield: a colorless solid, 59 mg (70%). 1H NMR (CD_3OD): δ 5.20 (t, 1H), 4.3 (m, 1H), 3.42 (m, 1H), 3.38 (s, 3H), 2.88 (d, 1H), 2.63 (t, 1H), 2.51 (d, 1H), 2.1–2.3 (m, 2H), 2.2 (m, 1H), 1.89 (d, 1H), 1.7–1.9 (m, 2H), 1.8 (d, 3H), 1.7 (d, 3H), 1.17 (s, 3H), 0.96 (m, 1H). HR-MS found: MH+ (283.3).

A solution of C16-09:0 (COOH) PC 1-hexadecyl-2-azelaoyl-sn-glycero-3-phosphocholine, followed by 4-dimethylaminopyridine (DMAP) and N, N'-dicyclohexyl-carbodiimide (DCC), was added to fumagillol in dry dichloromethane. The reaction mixture was stirred overnight at ambient temperature then passed over a short pad of silica gel using EtOAc/n-hexane. The filtered solvent was removed *in vacuo*, and the oil residue was purified by column chromatography on SiO_2 using EtOAc/n-hexane for elution to yield the fumagillin prodrug (Fum-PD) compound as a pale yellowish solid (yield: 54%). 1H NMR ($CDCl_3$): δ 0.88 (t, 3H), 1.22–1.37 (m, 37H), 1.58–1.96 (m, 20H), 2.26–2.60 (m, 7H), 3.40 (m, 12H), 3.48 (m, 3H), 3.86–4.00 (m, 4H), 4.10–4.37 (m, 5H), 5.21 (m, 1H). HR-MS found: 930.6 (MH+).

Preparation of copper nanoparticles Copper-oleate (260 mg) dissolved in toluene was suspended in almond oil (4 ml), gently vortexed to homogeneity, and filtered through a small bed of cotton. The solvent was evaporated under reduced pressure at 45°C, leaving a mixture containing 65 mg of copper oleate per ml. The surfactant co-mixture included high-purity egg yolk phosphatidylcholine (91.9 mol%), cholesterol (8 mol%), and $\alpha_v\beta_3$-peptidomimetic antagonist conjugated to PEG_{2000}-phosphatidylethanolamine (0.1 mol%; Kereos, St. Louis, MO, USA). Therapeutic $\alpha_v\beta_3$-CuNPs incorporated the Sn 2 lipase labile fumagillin prodrug (2.28 mol%) at the equimolar expense of phosphatidylcholine. The surfactant co-mixtures were dissolved in chloroform, evaporated under reduced pressure, dried in a 40°C vacuum oven overnight, and dispersed into water by probe sonication. This suspension was combined with the copper oleate-almond oil mixture (20% v/v), distilled deionized water (77.3% w/v), and glycerin (1.7%, w/v) and continuously processed at 20,000 psi for 4 min with an S110 Microfluidics emulsifier (Microfluidics, Newton, MA, USA) at 4°C. The copper nanoparticles (CuNPs) were dialyzed against water using a 20-kDa MWCO cellulose membrane for a prolonged period of time and then passed through a 0.45 µm Acrodisc syringe filter (Pall Life Sciences, East Hills, NY, USA). To inhibit lipid oxidation, the CuNPs were stored under an argon atmosphere, typically at 4°C (Figure 4.1).

The nominal hydrodynamic diameter (D_h) of the $\alpha_v\beta_3$-CuNPs and the fumagillin prodrug CuNPs was determined by dynamic light scattering (DLS) measurements (Brookhaven ZetaPlus, Brookhaven Instruments Corporation) in aqueous solution, were typically 190 nm ± 15 nm (std error), with a polydispersity of 0.09 ± 0.01, and a zeta potential of -23 ± 06 mV. Incorporation of the prodrug at 2.28 mol% (~0.5 mM) within the surfactant co-mixture had negligible impact on particle sizes.

The $\alpha_v\beta_3$-integrin antagonist was a quinalone nonpeptide developed by Lantheus Medical Imaging (Billerica, MA, USA) and synthesized by Kereos (U.S. Patent 6,511,648 and related patents). The vitronectin antagonist was reported and characterized as the ^{111}In-DOTA conjugate RP478 and cyan 5.5 homologue TA145. [66] The homing specificity of the ligand was demonstrated and characterized with Matrigel plug implanted in *Rag1*^{tm1Mom} Tg (Tie-2-lacZ)182-Sato and C57Bl/6 mice. [60]

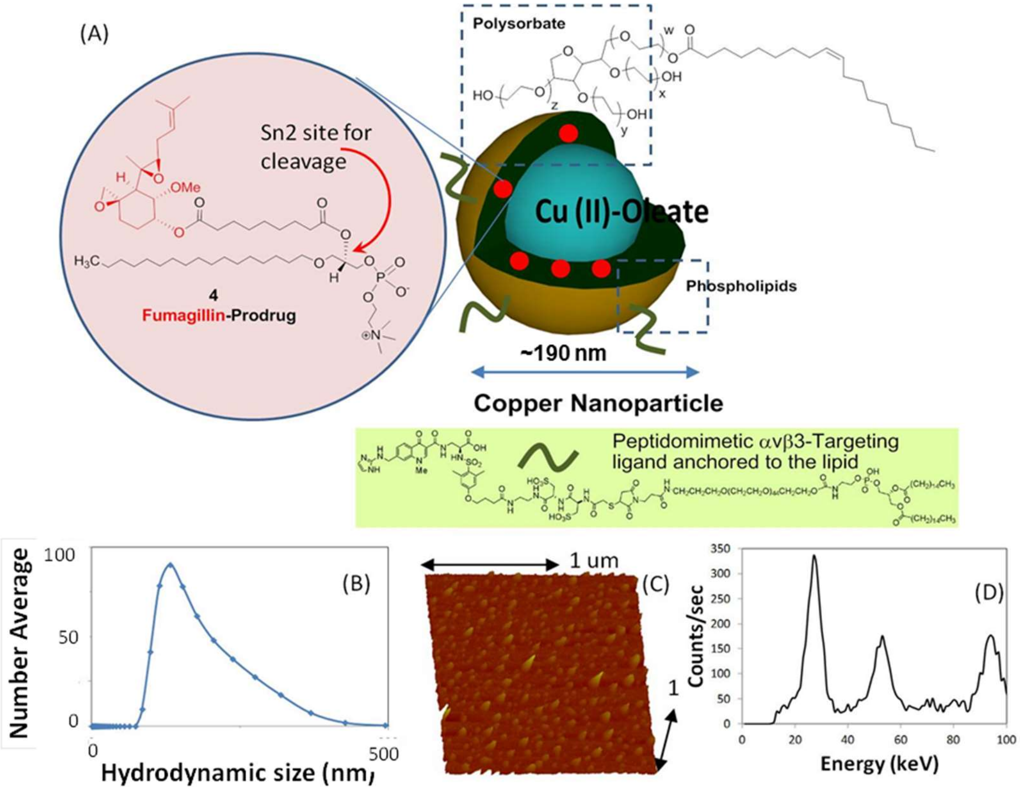

Figure 4.1 Synthesis and physiochemical characterization of CuNPs. (a) schematic of the concept of CuNPs with fumagillin prodrug; (b) hydrodynamic particle size distribution from DLS. The nominal hydrodynamic diameters of αvβ3-CuNPs and fumagillin prodrug CuNPs were typically 190 nm ± 15 nm, (c). Anhydrous state atomic force microscopy (AFM) image of CuNPs (drop-deposited on glass) Average height: 80 nm ± 12 nm. (d). EDX spectrum generated from the SEM image

The reference gold nanobeacons (GNBs) used in this study were prepared and characterized as previously described. [60] The GNBs were in a 20 vol% suspension with a nominal particle size of 160 nm, containing 6120 gold-oleate particles (3-5 nm)/nanobeacon, with a gold content of 1080 μg/g.

Matrigel™ plug mouse model of angiogenesis All animal studies were conducted in accordance with protocols approved by the Animal Care and Use Committee of Washington University Medical School.

Athymic nude-mice (Harlan Labs, Indianapolis, IN) with body weights ranging from 23 to 27 g were obtained. Anesthesia was induceod by ketamine (100 mg/ml) and xylazine (20 mg/ml), which were maintained with 0.5% to 1% isoflurane in oxygen, with ventilator support and supplemental temperature support. Matrigel (0.5 ml, BI, Biosciences, San Jose, CA, USA) enriched with fibroblast growth factor-2 (500 nm/ml; Sigma-Aldrich, St. Louis, MO, USA) and heparin was implanted subcutaneously along the mouse flank. The nude mice (n = 12) were randomly distributed into four groups to test (1) the efficacy of $\alpha_v\beta_3$-CuNPs for PA molecular imaging of angiogenesis *in vivo* and (2) the efficacy of $\alpha_v\beta_3$-CuNPs with Fum-PD as a theranostic agent. For the first test, three groups were compared on day 18 using PA imaging: (1) $\alpha_v\beta_3$-CuNPs without Fum-PD (integrin targeted, n=3); (2) nontargeted CuNPs (nonspecific entrapment, n=3) and (3) $\alpha_v\beta_3$-almond oil nanoparticle (NP) followed after 10 min by $\alpha_v\beta_3$-CuNPs without Fum-PD (specific competition, n=3). To address the second question within the same experimental design, (4) $\alpha_v\beta_3$-CuNPs with Fum-PD were administered on days 11 and 15, following Matrigel implantation, and the effect on angiogenesis was assessed on day 18 with $\alpha_v\beta_3$-CuNPs without Fum-PD (n=3). All treatments were injected via tail vein at 2 μl/g body weight of the 20 vol% nanoparticle suspensions. For each animal dynamic PA imaging was performed before injection (baseline, 0 min) and then repeated every 30 min over 270 minutes post-injection.

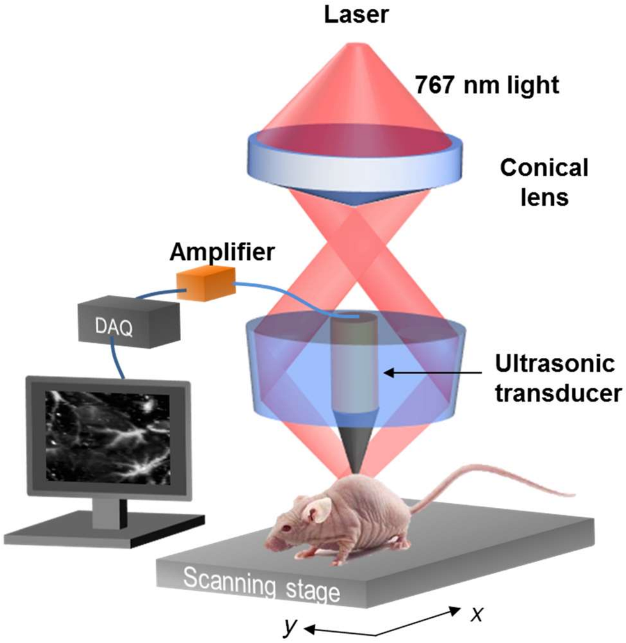

Figure 4.2 System schematic of a reflection-mode dark-field illumination PA system

Photoacoustic imaging A reflection-mode PA imaging system (Figure 4.2) using dark-field ring-shaped illumination [67] was pumped by a Q-switched Nd:YAG (LS-2137; Lotis TII) laser with <15-ns pulse duration and a 10-Hz pulse repetition rate. The light energy on the sample surface was controlled to conform to the American National Standards Institute (ANSI) standard for maximum permissible exposure. A 10 MHz central frequency, spherically focused (2.54 cm focus length, 1.91 cm diameter active area element, and 68% nominal bandwidth (One way -6 dB bandwidth is ~96%) ultrasonic transducer (V315; Panametrics-NDT, Waltham, MA, USA) acquired the generated PA signals. The signal was amplified by a low-noise amplifier (5072PR; Panametrics-NDT), and recorded using a digital oscilloscope (TDS 5054; Tektronix, Beaverton, OR, USA) with 50-MHz sampling. PA signal fluctuations due to pulse-to-pulse energy variation were compensated for by signals from a photodiode (DET110; Thorlabs, Newton, NJ, USA), which sampled the energy of each laser pulse.

Prior to *in vivo* imaging, two preliminary experiments were performed. In preliminary experiment 1, individual samples of CuNPs (20 vol%) and bovine blood (hct. ~45%) were placed into individual transparent plastic tubes (ID, 510 μm) and imaged by the PA system at 767 nm. The A-line signals from these two tubes are presented in Figure 4.3 as superimposed waveforms.

In preliminary experiment 2, the transparent Tygon tubes (ID, 510 μm) were filled with CuNPs (20 vol %), GNBs (20 vol%), and whole bovine blood (hct. ~45%). They were imaged at varying wavelengths between 730 nm and 830 nm. As an extension of this experiment, CuNPs were serially diluted from 6.0 μM to 0.17 μM and imaged at 750 nm, 760 nm, 770 nm, 780 nm, and 790 nm. In each experiment, the maximum amplitudes of the A-line signals (n=5) at each wavelength were averaged.

Finally, *in vivo* imaging of angiogenesis in the Matrigel Plug model was performed. A linear translation stage (XY-6060; Danaher Motion, Rad ford, VA, USA) was used for raster scanning to obtain 3-D PA data. A computer controlled the stage and synchronized it to the data acquisition. To shorten the data acquisition time, a continuous scan was used without signal averaging. Typical scanning values are as follows: voxel dimensions, 0.1 × 0.2 mm; laser pulse repetition rate, 10 Hz; acquisition time, ~20 min.

In vivo imaging was performed using ventilated anesthetized mice with shaved flanks, constantly warmed to 37°C by a heating block and positioned immediately beneath the transparent clear membrane. PA imaging was performed at 767 nm, as previously used for GNB *in vivo.* [60] Similarly, the vessel-integrated PA amplitude, calculated by integrating the enveloped PA signal amplitude over the blood vessel region , was used to quantify the degree of angiogenesis. The vessel-integrated PA amplitude was normalized to that of the pretreatment level during the analysis.

Statistical Analysis Data were analyzed using analysis of variance (GraphPad Prism Ver. 6.03) ($p < 0.05$). Data are presented as the mean ± standard error of the mean unless otherwise stated.

4.3 Results

Given the inherently strong PA signal of hemoglobin, the efficacy of PA contrast agents for targeted molecular imaging of neovascular integrin expression is dependent on the strength and differentiation of its signal from the blood background. The PA signal of CuNPs (20 vol%) was compared with whole bovine blood (45% hct.) at 767 nm. As seen in Figure 4.3, the time-aligned PA signal of the copper NP emulsion was markedly greater than that of the bovine blood at 767. The peak-to-peak signal of the CuNPs (2.3 a.u.) was 4-fold greater than that of blood (0.58 a.u.) at 767 nm, suggesting that the PA signal of neovascular bound CuNPs could be readily detectable *in vivo*.

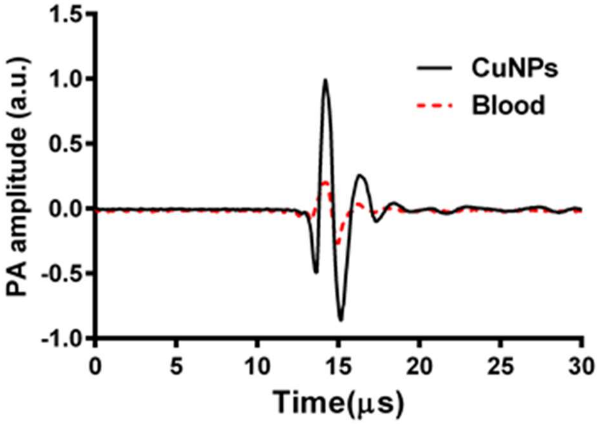

Figure 4.3 Overlay of PA signals from CuNPs and blood. CuNPs(20 vol%) and blood samples (whole bovine blood, hct. 45%;)were placed into transparent TygonTM tubes (ID = 510 µm) and imaged by the PA system at 767 nm. The peak-to-peak PA signal from the CuNPs was 4 times greater than that of the blood at 767 nm.

GNBs have been previously shown to produce strong PA contrast *in vivo* when applied to sentinel lymph node imaging or when targeted to neovasculature *in vivo.* [60,63,68,69] The PA signal enhancement of CuNPs relative to blood (45% hct.) was compared to the signal of GNBs relative to blood across a NIR frequency range of 730 nm to 830 nm (Figure 4.4) on an equal nanoparticle number basis. Over almost the entire spectrum, the CuNPs signal strength relative to blood was around 5-fold greater with a noticeable decline beyond 820 nm. In general, the PA ratios of GNBs and CuNPs were very similar except between 760 nm and 790 nm, with the greatest divergence between GNBs and CuNPs at 770 nm, at which point the gold contrast result was nearly twice that of copper. GNB particles experienced the same declining results as CuNPs from 800 nm and beyond.

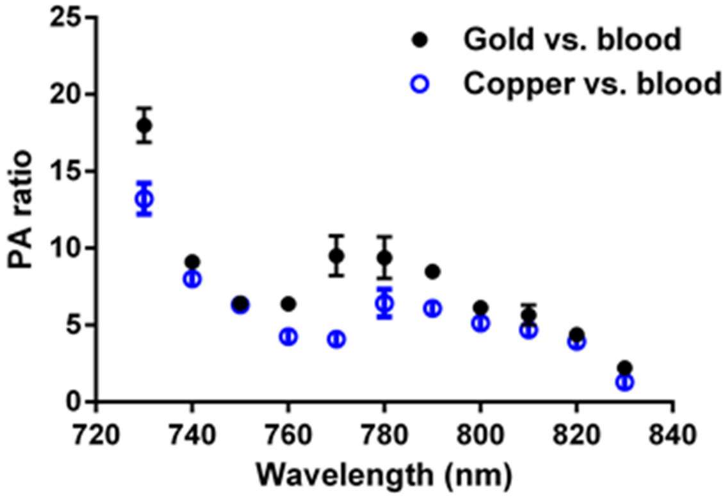

Figure 4.4 Equal-nanoparticle-based ratio of peak-to-peak PA signal amplitudes from previously reported gold nanobeacons (20 vol%) and CuNPs (20 vol%) to those of whole bovine blood (hct. 45%) over the 730 – 830 nm range. Over the whole spectrum, PA signals of CuNPs were markedly greater than those of the blood. In general, the PA ratios of GNBs and CuNPs relative to blood were similar.

The concentration dependence of CuNPs' signals as a function of frequency was examined. CuNPs were serially titrated from 6.0 µM to 0.17 µM and studied at NIR wavelengths between 750 nm and 790 nm (Figure 4.5(a)). PA amplitude decreased with reductions in CuNP concentration level, but the magnitude of signal diminishment was generally less than the percent change in CuNP level. This was particularly notable for the higher concentrations, between 6.0 µM and 1.5 µM. The magnitude of the CuNP's PA signal was greatest at 750 nm and 760 nm. At higher wavelengths, the magnitude of the CuNP signal trended lower, with the greatest contrast loss seen at the lower CuNP concentrations. It can be calculated from the extinction coefficient spectrum shown in Figure 4.5(b) that the extinction coefficient of CuNPs at 700 nm was 1.3 times as strong as that at around 770 nm. However, the laser energy at 767 nm (the peak of laser energy) is an order of magnitude stronger than that at 700 nm. Therefore, neovascular imaging signal peaks around 767 nm.

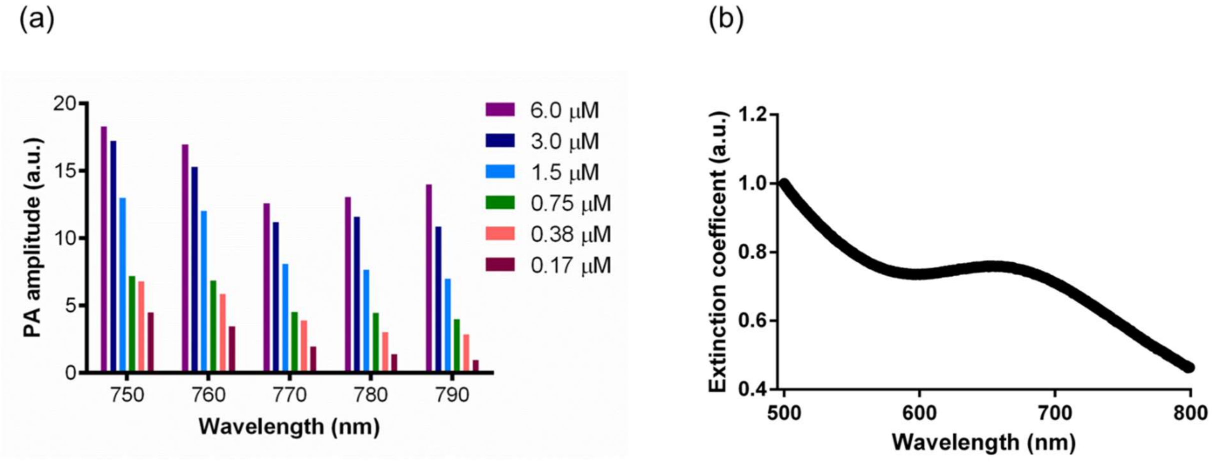

Figure 4.5 Photoacoustic spectrum characterization of copper nanoparticles. (a) PA signals from copper nanoparticles (20 vol%) in a transparent Tygon tube filled with serially diluted copper nanoparticles (0.17 µM, 0.38 µM, 0.75 µM, 1.5 µM, 3.0 µM, 6.0 µM) at laser wavelengths from 750 nm to 790 nm, with 10 nm step size. A nonlinear relationship between the PA amplitude and CuNP concentration was observed. (b)The extinction coefficient spectrum of the CuNPs (20 vol%) at laser wavelengths from 500 nm to 800 nm.

To provide robust assessment of PA signal enhancement due to the CuNPs, *in vivo* neovascular imaging was studied in the Matrigel plug model in mice. Mice implanted with Matrigel™ 18 days previously received either $\alpha_v\beta_3$-CuNPs, nontargeted CuNPs, or $\alpha_v\beta_3$-CuNP preceded by 10 minutes with a competitive dose $\alpha_v\beta_3$-oil only NPs (1:1). As seen in Figure 4.6, at 0 min, forming neovessels were observed by the inherent PA contrast imparted by erythrocyte hemoglobin. The magnitude of the signal varied among animals with the extent of neovascular proliferation. Following $\alpha_v\beta_3$-CuNP injection, the magnitude of the PA signal in these immature tubules clearly increased, and numerous incomplete vascular sprouts appeared, as we have previously reported for GNBs. [60] The formation of the neovessel shoots depicted an early evolution stage of a dense and irregular microvasculature. In contradistinction to the animals receiving $\alpha_v\beta_3$-CuNPs, those given nontargeted-CuNPs had very little increase in the vessel-integrated PA amplitude. As shown, a minimal passive accumulation of the CuNPs in the forming bridges and sprouts combined with a modest amount of blood pool enhancement relative to the neovessel tubules at 0 min. We have previously reported that blood pool enhancement for GNBs in the intact microvasculature surrounding the Matrigel implant was negligible, [60] but within the plug, the slow moving blood may be associated with very slow washout. In the competition group at 170 min, very little change in the PA signal from the forming vascular tubules or sprouts was observed. In this group, the pretreatment binding of the $\alpha_v\beta_3$-oil NPs appeared to have blocked most of the receptors for the $\alpha_v\beta_3$-CuNP and even precluded significant passive accumulation.

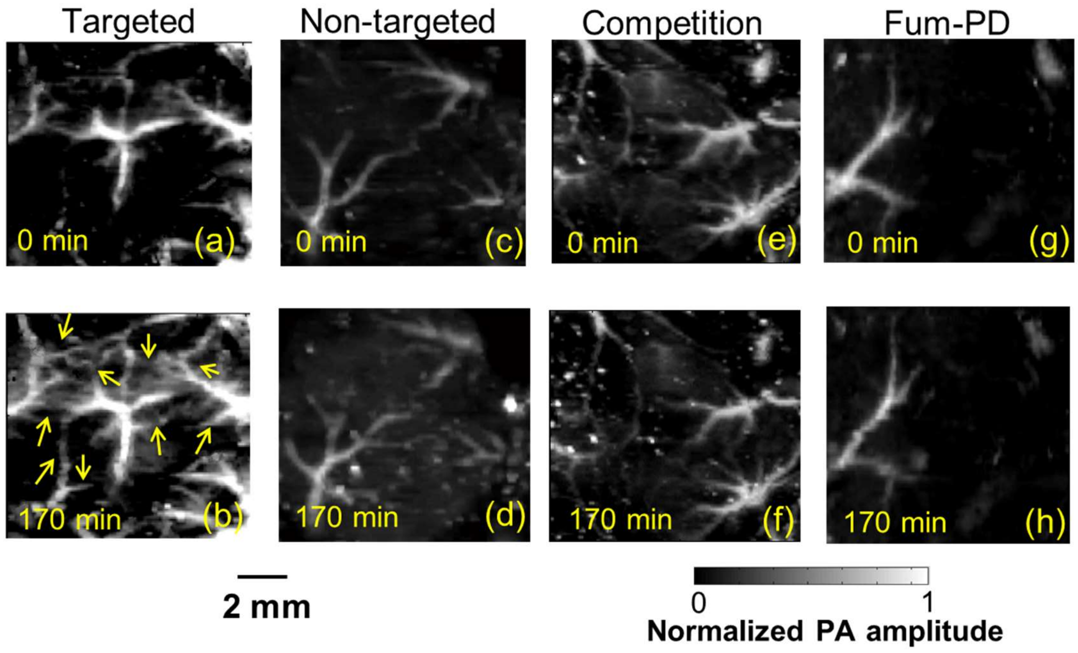

Figure 4.6 *In vivo* PA images of the Matrigel plug area implanted in 4 groups of mice 18 days prior to imaging. (a)-(b) Targeted CuNPs group: mice received αvβ3-CuNPs just before PA imaging. The enhanced neovasculature is marked by arrows in B. (c)-(d):Nontargeted CuNPs group: mice received nontargeted CuNPs right before PA imaging. (e)-(f):Competition group: mice received a competitive dose of αvβ3-oil only NP (1:1) 10 minutes prior to imaging, followed by αvβ3-CuNPs right before imaging. (g)-(h) Fum-PD group: mice received αvβ3-CuNPs with Fum-PD 11 and 15 days after the Matrigel implantation, and αvβ3-CuNPs w/o Fum-PD right before PA imaging. Comparing the PA images of the nontargeted, competition, and Fum-PD groups at 0 min and 170 min, very little change in PA signals can be found. For all PA images, laser wavelength = 767 nm.

Figure 4.7 presents the average change in the vessel-integrated PA amplitude between the three treatment groups, showing that the $\alpha_v\beta_3$-CuNPs increased PA contrast, while the nontargeted-CuNP did not (p<0.05). Moreover, the specificity of targeting the neovasculature was again demonstrated by the low vessel-integrated PA amplitude measured in the competition group versus the $\alpha_v\beta_3$-CuNP group (p<0.05), and even relative to the nontargeted control. Dynamic accumulation of PA contrast measured in the $\alpha_v\beta_3$-CuNP group increased progressively over the 230 minutes post injection interval (Figure 4.8).

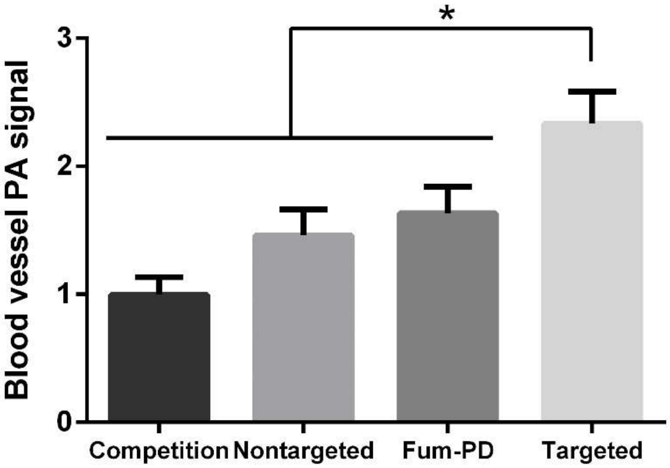

Figure 4.7 Blood vessel PA signal at 170 min post-injection for four groups of mice. The blood vessel PA signal (normalized to the baseline, i.e., blood vessel PA signals at 0 min) increase for the αvβ3-targeted group was greater (*$P<0.05$) than that of the other three groups. Almost no blood vessel signal increase was measured in the competition group, and a slight increase of blood vessel signal was observed in the non-targeted and Fum-PD groups.

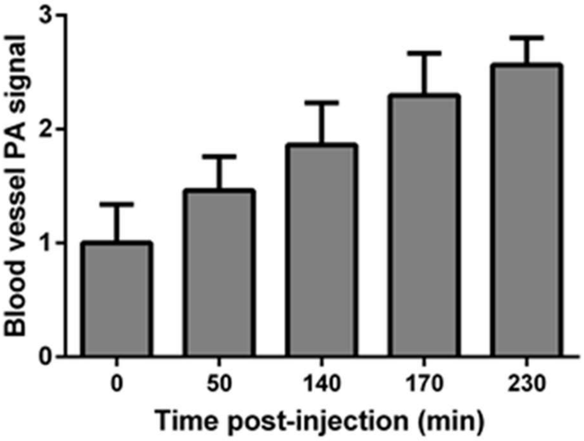

Figure 4.8 Blood vessel PA signal vs. post-injection time for the αvβ3-CuNPs group. The blood vessel signal increased progressively over the 230 min post injection interval.

In a second aspect of the Matrigel™ angiogenesis experiment, fumagillin-prodrug (Fum-PD), [70,71], was incorporated into the phospholipid surfactant at 2.28 mol%. The chemical synthesis, characterization, and *in vivo* effectiveness of Fum-PD incorporated into perfluorocarbon nanoparticles has been previously reported. [65,72] $\alpha_v\beta_3$-CuNP (2 µl/g) incorporating Fum-PD was administered on days 11 and 15 post Matrigel™ implant, and the vessel-integrated PA amplitude in these animals was determined on day 18. At baseline, the amount of neovasculature observed by PA imaging was sparse, but no more so than that in the other groups. Moreover, following $\alpha_v\beta_3$-CuNP injection there was little sprout enhancement at 170 minutes. As shown collectively in Figure 4.6 and Figure 4.7, the vessel-integrated PA amplitude change was similar to that measured in the nontargeted-CuNP group, and appeared related to modest particle accumulation in the nascent tubules, with less signal related to sprout formation. Although drug delivery and imaging were not performed simultaneously to minimize the differential animal handling between the groups, these results illustrated the potential of CuNPs as vehicles for drug delivery and diagnosis.

4.4 Discussion

Photoacoustic imaging has demonstrated broad applications in the imaging and physiological characterization of the vasculature, particularly the microvasculature [59,73], and microvascular expansion driven by brain tumor hypoxia [74]. The vascular endothelium provides numerous "road-signs" reflecting its developmental stage, as seen for the neovasculature, or its state of activation, as seen with inflammation. In each instance, specific PA characterization depends on molecular imaging through the recognition of unique endothelial biomarkers. [61,62,68,75-79] In the present study, sparse activated $\alpha_v\beta_3$-integrin was selected as a biomarker of angiogenesis. While we have previously reported dynamic imaging of the forming neovasculature with gold nanobeacons, the high and unpredictable cost of gold, and the unclear long-term safety of larger nonmetabolizable nanoparticles, such as carbon fullerenes or nanotubes, led to the design and development of CuNPs. While free copper can elicit systemic toxicity, CuNPs are comprised of high densities of small organometallic complexes that can be eliminated through the bile or urine, minimizing the risk potential for this agent.[80] In the present study, CuNPs offered comparable PA contrast enhancement, on an equal particle basis, to GNBs both *in vitro* and *in vivo*.

In vivo PA imaging was performed at 767 nm, which was optimal for the previously targeted GNB agent, but the spectral assessments of CuNP relative to blood and as a function of particle concentration suggest 740 or 750 nm may be preferred for targeting sparse epitopes like adhesion molecules. Also, the time for maximum neovascular signal was found to be nearly 4 hours in the Matrigel model, but similar particles administered *in vivo* for deeper-tissue angiogenesis imaging with MRI were shown to provide minimal targeting benefit after 2 hours. [81,82] The difference likely relates to vascular vasoconstriction with reduced blood flow to the skin in the subcutaneous Matrigel implant model, which is aggravated by the cooling effects of acoustically coupling the PA probe to the body during anesthesia, despite provision of supplemental heating to maintain core body temperatures. Lastly, CuNPs were designed to be vascular constrained agents to reduce nonspecific signal generated by interactions with extravascular cells expressing the $\alpha_v\beta_3$-integrin. Close examination of the 170-minute PA images in Figure 4.6 showed negligible extravasation of the particles. Although much attention has been attributed to the leakiness of angiogenesis, even in the sprouting regions where the neovasculature is essentially open-ended, no evidence of nanoparticle accumulation beyond the tips of the forming neovessel branches was noted. Moreover, this was a consistent observation, regardless of whether the nanoparticles were integrin-targeted or not.

Fumagillin prodrug was incorporated into the phospholipid surfactant of CuNPs and demonstrated to elicit anti-angiogenic effects in this Matrigel model. Microanatomically, the treatment virtually eliminated the rich web of sprouts in the mice receiving $\alpha_v\beta_3$-CuNPs without Fum-PD. “Pruning” of neovasculature was first suggested by Jain in a visionary manner, but in this study, the concept was visually apparent. [83-85] Despite all of the extensive clinical research on the effects and benefits of anti-angiogenesis therapy in cancer and selected other pathologies, virtually all of the work has centered on vascular endothelial growth factor (VEGF) inhibition. While VEGF is a clear driver of angiogenesis, it elicits pleotropic effects and is not solely responsible for neovascularization. [86] Moreover, VEGF is produced by a variety of cell types, making effective blockade of the growth factor challenging. Typically, relatively high dosages of medicants are used clinically and these treatments have well known side-effects. [87]

As reported by others, fumagillin is an antiangiogenic agent which is specific for proliferating endothelial cells, but its clinical analogue, TNP-470, possessed only antidotal effectiveness in the clinic at the high doses required, which were accompanied by numerous toxicities, including neurocognitive dysfunction. [88-90] Fumagillin can be effectively incorporated into the phospholipid surfactant of nanoparticles for targeted delivery of anti-angiogenesis therapy through a mechanism referred to as “contact facilitated drug delivery” (CFDD) at a small fraction of the dosages previously used systemically. [48,91,92] Tethering of the lipid-encapsulated nanoparticle to the target cell surface facilitates the interaction and hemifusion of the two lipid membranes, which affords the passive transfer of the drug and phospholipids from the nanoparticle surface to the outer leaflet of the target cell membrane. The drug is then translocated to the inner leaflet through an ATP-dependent mechanism. [93,94] CFDD eliminates the need for particle internalization with subsequent endosomal drug payload escape.

However, pharmacokinetic studies showed that fumagillin dissolved into the lipid membrane was substantially lost prematurely during circulation to the target neovasculature, despite its effectiveness *in vivo*. Fum-PD was developed to address this early release by coupling the drug through the Sn 2 acyl position (i.e., the stereospecific hydroxyl group of the second carbon of glycerol). Subsequent transfer of the monolayer components into the target cell membrane allows cytosolic phospholipases to enzymatically cleave the Sn 2 ester and release the drug, allowing it to diffuse into the cytosol for effect. Fum-PD as well as other similar prodrug compounds is incorporated stably into the hydrophobic aspects of the particle membrane. Importantly, Sn 2 lipase-labile prodrugs within the particle lipid membrane are stable in blood and plasma, even in the presence of excess exogenous lipase, and do not passively exchange to co-circulating RBC. [95] The results of the present research show the first example of a systemically targeted antiangiogenic drug delivery with a photoacoustic contrast nanoparticle. Given the rapid developments in hardware and software for PA imaging, one can envision numerous medical applications for low-cost CuNPs particles to target neovascular or alternative endothelial biosignatures for diagnostic and theranostic purposes.

Unlike current VEGF inhibitors, fumagillin-prodrug specifically targeted to angiogenic vessels suppresses angiogenesis, clinical disease, and inflammation in a preclinical model of rheumatoid arthritis (RA). [50] Enhanced endothelial nitric oxide (NO) modulates local macrophage inflammatory activity through NO activation of AMP-activated protein kinase (AMPK). *In vivo*, NO-induced AMPK activation increased autophagy by inhibiting mammalian target of rapamycin (mTOR) activity. Increased autophagy mediated the degradation of IkappaB kinase (IKK) and suppressed NF-κB. The suppression of NF-κB was associated with diminished inflammatory cytokine release. Importantly, the NO mediated inhibition of inflammation was reversed *in vitro* and *in vivo* by the co-administration of N(G)-nitro-L-arginine methyl ester (L-NAME), a nitric oxide synthase inhibitor. These unique anti-angiogenic and anti-inflammatory properties of Fum-PD nanotherapy may be applicable to the treatment of other angiogenesis-dependent diseases.

4.5 Conclusions

Soft copper oleate nanoparticles were synthesized and conceptually shown to offer effective photoacoustic contrast comparable to gold-based agents, but at a much lower cost and higher material availability. CuNPs possessed strong PA contrast relative to blood from 730 nm to 830 nm, which was similar to the PA signal response of gold nanobeacons relative to blood overall. In the Matrigel angiogenesis model, $\alpha_v\beta_3$-CuNPs markedly enhanced neovessel tubules and identified a myriad of incomplete emergent neovascular sprouts, which were not well detected or specifically differentiated as angiogenesis with inherent PA imaging. $\alpha_v\beta_3$-CuNPs effectively delivered fumagillin-prodrug, a potent anti-angiogenic therapy, *in vivo*, providing the first example of a systemically targeted drug delivery therapy with a photoacoustic contrast agent.

Chapter 5 Photoacoustic Voltage Imaging with a Synthetic Dye

In this chapter, we extend photoacoustic functional imaging, formerly based on hemoglobin to include a voltage sensitive dye. We validate dye functions in HEK293 cells, and mouse brains in a epilepsy model and a cortical electrical stimulation model. The work of this chapter is based on the joint work of Bin Rao and it is under review.

5.1 Background

A human brain generates thoughts, perceptions, memories, actions, and emotions based on environments and experiences, while defining each individual person. Despite the similarities of human brains, the detailed connections and interactions of brain neuron circuits are uniquely shaped by a person's life. Understanding the brain will not only significantly advance human knowledge, but also catalyze new treatment modalities for devastating brain diseases such as Parkinson's disease[96-98] and Alzheimer's disease[99,100].

To decipher human brains, we need to measure neuronal activity with higher precision, and over much larger spatial and temporal scales than currently achievable. However, current voltage recording tools, including electrodes and optical microscopes, are underdeveloped. Microelectrodes and macro-electrodes are workhorses in recording neural voltage response signals and stimulating neural tissue[101,102] in clinics and labs. But they are limited by the small number of practicable simultaneous recording points and they cannot interrogate tiny neuronal circuit components such as dendrites and axon terminals. More recently, non-invasive optical methods for recording activity in large numbers of neurons have been significantly improved[103,104]. Optical, chemical, and genetic sensors have enabled scientists to study microcircuits and understand sub-cellular neurochemical dynamics in dendrites and axons[103-108]. Despite recent innovations in optical sensors[18-19] and non-invasive optical imaging instruments, much brain research with non-invasive optical methods is confined to the neuronal circuits of the top layer of the brain[109]. *In vivo* imaging of deep brain neuronal tissue and neuronal activity remains an unmet challenge.

Photoacoustic tomography[6,59,110-112] (PAT) is a hybrid optical imaging method that detects acoustic responses excited by laser pulses of both ballistic and diffused photons and achieves high-resolution optical-contrast tomography at imaging depths beyond the optical diffusion limit. Specifically, optical absorbers at all imaging depths absorb pulsed laser energy and radiate photoacoustic waves that are detected by acoustic sensors for rendering three-dimensional images of the optical absorbers. Although PAT is a versatile optical imaging modality, its potential in imaging voltage responses of neuronal activities has never been explored.

In this communication, for the first time, we demonstrate photoacoustic voltage response imaging contrast by using a non-radiative voltage sensor (dipicrylamine, or DPA for short). By using spectroscopic photoacoustic tomography at isosbestic wavelengths, we can successfully separate the voltage response signals from the hemodynamic signals on live brain surfaces. We demonstrate the photoacoustic detection of HEK293 cell membrane voltages through 4.5 mm thick *ex vivo* rat brain tissue. Although the current voltage dye (DPA) does not immediately allow *in vivo* deep brain voltage response imaging, we believe our method opens up a feasible technical path for deep brain studies in the future.

5.2 Methods

5.2.1 Methods for Phantom Study and Live Cell Imaging

Method for recording DPA responses to different cell membrane resting potentials Cell membrane resting potentials were adjusted by changing the extracellular potassium ion concentration. The membrane potential change (ΔE) is roughly estimated by

$$\Delta E = \left(\frac{RT}{F}\right) \ln\left(\frac{K_a}{K_i}\right), \tag{5.1}$$

where R is the universal gas constant, T is the absolute temperature, F is the Faraday constant, and K_a and K_i are the adjusted and initial potassium concentrations. Equation (5.1) is derived from the Nernst equation, with the assumptions that the internal ion concentrations remain constant during the short exposure to increased extracellular potassium ion concentration and that the impact of the Na^+ channel is disregarded[113,114].

The stock DPA dye solution is 2 mM DPA (Biotium) in DMSO. The DPA stock solution was diluted to 5 µM for *in vitro* cell culture experiments. The initial extracellular medium was made by adding 20 mM HEPES and 5 µM DPA to Hanks' Balanced Salt Solution (1.3 mM $CaCl_2$, 5.4 mM KCl, 0.4 mM KH_2PO_4, 0.5 mM $MgCl_2$, 0.4 mM $MgSO_4$, 136.9 mM NaCl, 0.3 mM Na_2HPO_4, 4.2 mM $NaHCO_3$, and 5.5 mM glucose), and adjusting its pH to 7.4. Four adjusted extracellular media with potassium concentrations of 12.7 mM, 61.4 mM, 134.8 mM, and 296.0 mM were prepared by adding more KCl to the initial extracellular medium in order to adjust the cell membrane resting potentials by 20 mV, 60 mV, 80 mV, and 100 mV, according to Equation (5.1).

Human embryonic kidney 293 (HEK293) cells were cultured in DMEM (Invitrogen) supplemented with 10% fetal bovine serum and incubated at 37 °C with 5% CO_2. For photoacoustic microscopy, HEK293 cells were plated into a 35 mm glass-bottom petri dish (P35GCOL-0-14-C, MatTek) one day before the experiment. Prior to PAM imaging, 5 μM DPA was added to HEK293 cell culture medium (DMEM) and HEK293 cells were stained for 40 minutes. Baseline PAM images corresponding to a 0 mV cell membrane resting potential change were acquired with the initial extracellular medium. Then the medium was sequentially replaced by extracellular media with potassium concentrations of 12.7 mM, 61.4 mM, 134.8 mM, and 296 mM, and immediately imaged by a transmission-mode photoacoustic microscope (Figure 5.1) after each replacement. Before each replacement, we reset the DPA concentrations stained on the HEK293 cells by replacing the old medium with Hanks' Balanced Salt Solution (no DPA). A waiting time of 5–15 minutes, and occasionally multiple resets, were sometimes required for the photoacoustic signals from the HEK293 cells to subside to the baseline. The means and standard errors of photoacoustic signal amplitudes from the HEK293 cells corresponding to five different resting potentials were calculated and analyzed.

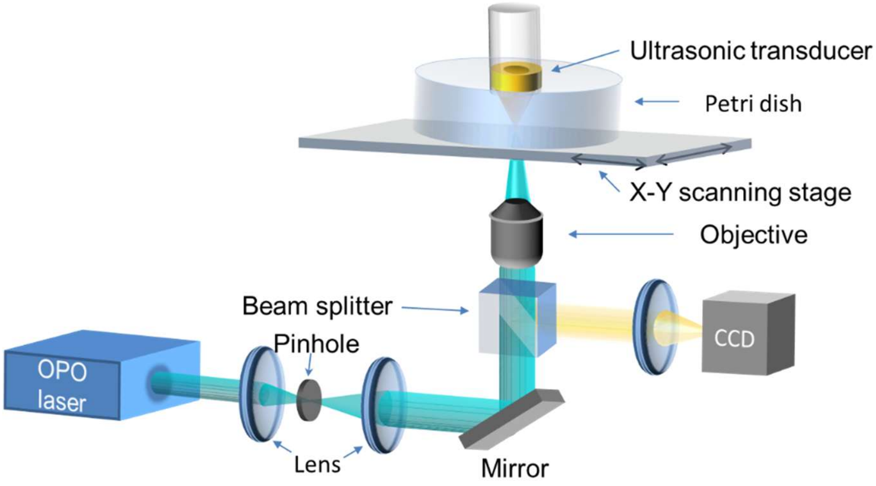

Figure 5.1 Experimental setup for in vitro photoacoustic cell membrane potential imaging

Experimental setup for *in vitro* photoacoustic cell membrane potential imaging A transmission-mode optical-resolution photoacoustic microscope (Figure 5.1) was used for *in vitro* voltage imaging of the HEK293 cell membranes. In Figure 5.1, an integrated diode-pumped Q-switched laser and optical parametric oscillator (OPO) system (NT242-SH, Ekspla) generate laser pulses (5 ns pulse width, 1 kHz pulse repetition rate) at 488 nm. The laser pulse is expanded and then focused by a 4x objective (Zeiss, 0.1 NA). The focused laser light induced an abrupt temperature rise in an illuminated absorber and excited photoacoustic waves, which are acoustically coupled by deionized water and detected by an ultrasonic transducer. The photoacoustic signal is amplified, digitized, and recorded. By raster scanning the sample with an X-Y scanning stage, a three-dimensional image of the sample is formed. A depth-encoded maximum-amplitude projection (MAP) image of the 3D data set shows the image in 2D format.

5.2.2 Methods for *In Vivo* Photoacoustic Voltage Imaging

Principle of separating voltage response signals from hemodynamic signals in live brain

The amplitudes of brain photoacoustic signals from hemoglobin and DPA dye excited by a nanosecond laser pulse are written as

$$\mathrm{p}_{Hb} = \alpha\xi\Gamma \mathrm{m}_{Hb}\mu_{Hb}F \tag{5.2}$$

$$\mathrm{p}_{DPA} = \alpha\xi\Gamma \mathrm{m}_{DPA}\mu_{DPA}F \tag{5.3}$$

where the subscripts Hb and DPA denote hemoglobin and DPA respectively, p denotes the amplitude of the photoacoustic signal, α is a spatially dependent factor, ξ is a coefficient representing distortion and attenuation of the photoacoustic signal, Γ denotes the Grϋneisen parameter of the medium, m denotes the molar concentration, μ denotes the molar optical absorption coefficient of hemoglobin, and F denotes the local optical fluence in J/m^2. The molar optical absorption coefficients of hemoglobin and DPA dye are known. The molar concentrations of hemoglobin and DPA are unknown. In order to separate DPA signals from hemodynamic signals, two measurements are required to solve the equations of the two absorbers.

For our two measurements, we selected two isosbestic wavelengths of hemoglobin (500 nm and 570 nm), where oxygenated and deoxygenated hemoglobin molecules have the same molar absorption coefficient values. Hence, the photoacoustic signals are dependent on the total concentration of hemoglobin only and are independent of the oxygen saturation of hemoglobin (i.e., the ratio of the concentration of oxygenated hemoglobin to the concentration of total hemoglobin). The laser fluence F was considered as constant after the calibration procedure described later in the *in vivo* experiments. We define $\mathrm{M}_{Hb} = \alpha\xi\Gamma \mathrm{m}_{Hb}F$ and $\mathrm{M}_{DPA} = \alpha\xi\Gamma \mathrm{m}_{DPA}F$ as the relative measurements of the concentrations. For the first measurement at 500 nm and the second measurement at 570 nm, we have the following:

$$\mu_{Hb500}\mathrm{M}_{Hb} + \mu_{DPA500}\mathrm{M}_{DPA} = \mathrm{p}_{500} \tag{5.4}$$

$$\mu_{Hb570}\mathrm{M}_{Hb} + \mu_{DPA570}\mathrm{M}_{DPA} = \mathrm{p}_{570} \tag{5.5}$$

Here, the subscripts 500 and 570 indicate the corresponding wavelengths in nm. The relative DPA and hemoglobin concentrations are computed as follows:

$$\mathrm{M}_{DPA} = \left(\mathrm{p}_{570} - \frac{\mu_{Hb570}}{\mu_{Hb500}}\mathrm{p}_{500}\right) / \left(\mu_{DPA570} - \frac{\mu_{Hb570}}{\mu_{Hb500}}\mu_{DPA500}\right) \tag{5.6}$$

$$\mathrm{M}_{Hb} = \left(\mathrm{p}_{500} - \frac{\mu_{DPA500}}{\mu_{DPA570}}\mathrm{p}_{570}\right) / \left(\mu_{Hb500} - \frac{\mu_{DPA500}}{\mu_{DPA570}}\mu_{Hb570}\right) \tag{5.7}$$

The method for separating DPA and hemoglobin signals with the above equations was successfully tested by measuring phantoms with preset concentrations, as detailed in the supplementary information.

Method of recording in vivo mouse brain response to electrical stimulation We constructed a PAM for *in vivo* mouse brain imaging. As shown in figure 5, the excitation light sources are (1) an OPO laser system (NT242-SH, Ekspla) and (2) a dye laser (Credo, Sirah) tuned to 570 nm and pumped by a 532 nm Nd:YLF laser (INNOSLAB, Edgewave). The 570 nm laser pulse is delayed by 1 μs relative to the 500 nm laser pulse. A dichroic mirror combines the 500 nm and 570 nm laser beams. To calibrate the fluctuations of laser pulse energy, a beam splitter splits 10% of the laser energies to a transmission-mode optical-resolution photoacoustic microscope that uses a black tape as sample. The remaining 90% of the laser energy is delivered to a miniature photoacoustic imaging probe comprising an achromatic lens (AC064-013-A, Thorlabs) and a customized ring-shaped focused ultrasonic transducer. The mechanical design of the miniature photoacoustic imaging probe allows adjusting the ring transducer for confocal optical and acoustic foci. During imaging, the ring transducer is immersed in the water tank, with a plastic membrane as its bottom. Electrical stimulation electrodes (MX216FW, FHC) are inserted around the edge of the cranial window. Stimulation pulses are sent by an electrical stimulator (Micro-stimu III, World Precision Instruments).

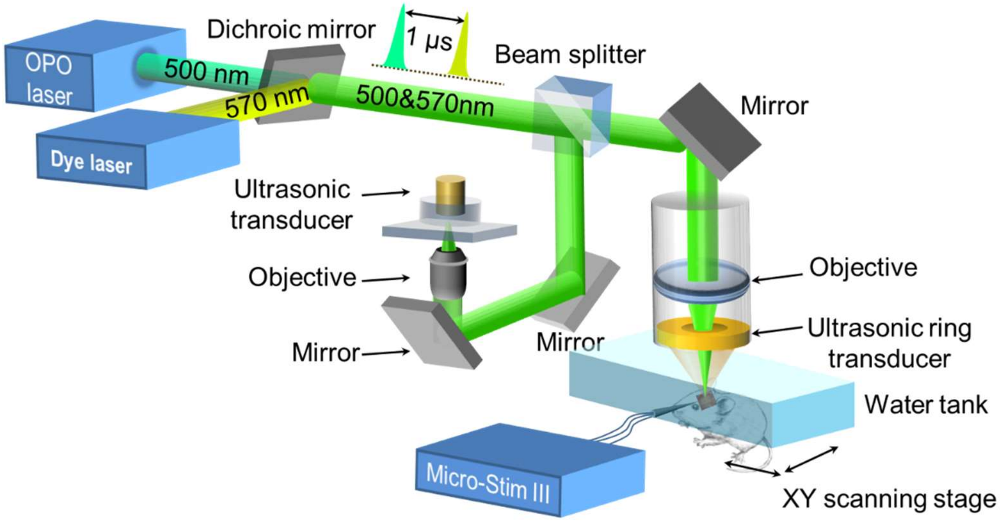

Figure 5.2 Experimental setup for *in vivo* photoacoustic mouse brain imaging

The animal preparation is detailed in the supplementary material. All experimental procedures were carried out in conformity with laboratory animal protocols approved by the Animal Studies Committee at Washington University in St. Louis. For *in vivo* mouse brain experiments, we diluted the stock DPA dye solution of 2 mM DPA (Biotium) in DMSO to 20 μM. Before photoacoustic imaging, 20 μM DPA was applied to the cranial window for 30 minutes of bath staining. For *in vivo* imaging, acoustic gels were placed between the plastic membrane of the water tank and the mouse brain. Initial 3D mouse brain imaging with the OPO laser tuned to 532 nm allowed us to select an M-mode imaging point that appeared to have minimum vasculature. To acquire baseline photoacoustic signals without stimulation, we performed M-mode recordings with dual wavelengths at the selected point. After that, M-mode recordings were collected at the same point during electrical stimulation, and then the photoacoustic responses from hemoglobin and DPA were calculated from Equations (5.6) and (5.7).

Method of recording in vivo mouse brain response to epilepsy induced by 4-Aminopyridine

We used the same PAM setup to image the mouse brain *in vivo* in response to epilepsy induced by 4-aminopyridine (4-AP). Similar to the method used in the electrical stimulation model, a cranial window was created in the mouse skull and 20 µM DPA was applied to the cranial window for 30 minutes of bath staining. After raster-scan imaging the mouse brain through the cranial window, we selected a point without noticeable interference from blood vessels. A baseline M-mode recording with dual wavelengths was obtained at that point, then 50 µL of 4-AP was injected through the cranial window into the brain cortex to induce focal seizure. After the injection, a raster-scanned image was acquired again to locate the M-mode imaging point. We waited until a visually observable seizure response occurred, and started M-mode recordings of the same location with dual wavelengths. Last, the photoacoustic responses from the hemoglobin and DPA were calculated from Equations (5.6) and (5.7).

Animal preparation Adult Swiss Webster (Hsd:ND4) mice were used for all *in vivo* imaging experiments. During the surgery, the mouse was first secured using a tooth bar on a platform and maintained under anesthesia with 1.5–2.0% vaporized isoflurane. The scalp of the mouse brain was removed. Then cyanoacrylate glue was applied to the gap between the back of the mouse's head and an aluminum plate with a "U" shaped dent as shown in Figure 5.3. Because the plate was secured to the platform, motions of the mouse head relative to the imaging setup were avoided. A 3 mm by 3 mm cranial window was then created on the mouse skull, and the isoflurane level was decreased to ~0.5% after surgery. For an electrical stimulation experiment, stimulation electrodes were inserted at the edge of the cranial window and fixed on the skull surface with cyanoacrylate glue. For a 4-Aminopyridine (4-AP) drug stimulation experiment, direct injection of 4-AP in the neocortex layer within the cranial window was used to induce epilepsy. 20 µM DPA dye was injected into the cranial window, and 20 minutes of staining time was waited before imaging. After the imaging procedures, the animal was euthanized. All experimental procedures were carried out in conformity with laboratory animal protocols approved by the Animal Studies Committee at Washington University in St. Louis.

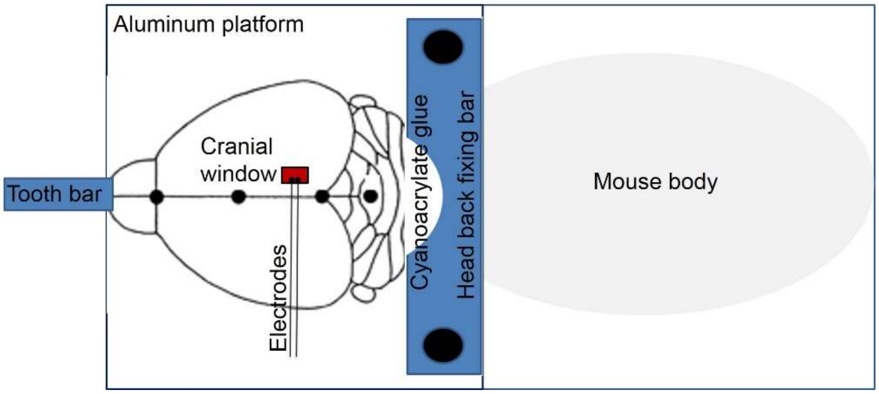

Figure 5.3 Schematic of animal preparation

5.2.3 Method of Imaging HEK293 Cell Clusters Through Thick *Ex Vivo* Brain Tissue

We used a photoacoustic computed tomography (PACT) system to demonstrate that PACT can potentially image deep brain voltage responses.

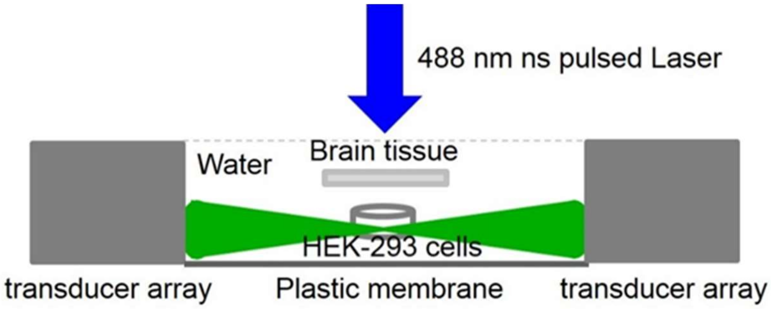

Figure 5.4 PACT setup for imaging in vitro HEK293 cell clusters through ex vivo thick brain tissue

The photoacoustic computed tomography (PACT) setup for imaging *in vitro* HEK293 cell clusters through *ex vivo* thick brain tissue is shown in Figure 5.4. 488 nm nanosecond (ns) pulsed laser (10 ns pulse width, 3 mJ laser pulse energy) is generated by an OPO laser. The collimated laser beam passed through *ex vivo* thick brain tissue before reaching the HEK293 cell clusters in an agarose tube. Upon laser excitation, photoacoustic waves generated by the HEK293 cells (stained with DPA) are detected by a circular transducer array (5 MHz central frequency, 512 elements). A back-projection algorithm is used to reconstruct PACT images

To mimic imaging through different thicknesses of brain tissue, a whole brain was harvested from a sacrificed rat (*Sprague Dawley*®, Charles River). The whole rat brain was embedded in agarose before being cut into slices either 1 mm or 0.5 mm thick by a vibrating blade microtome (Leica VT 1200 S). Only central slices with relatively large areas were used to construct *ex vivo* brain tissue layers between 2 mm to 5 mm thick. HEK293 cells that were initially grown in a T-75 flask were washed off with trypsin, immersed in Dulbecco's Modified Eagle's Medium (with no phenol red), stained with 5 μM DPA, incubated for 20 minutes in a CO_2 incubator (37° C, 5% CO_2), and distributed among six 15 ml agarose tubes. The HEK293 cell clusters in the first agarose tube were imaged through different thickness of brain tissue (0.0 mm, 2.0 mm, 3.0 mm, 4.5 mm, and 5. mm) in order to determine the maximum thickness of brain tissue through which HEK293 cell clusters remained visible. The extracellular potassium concentrations in five other agarose tubes were adjusted to achieve 0 mV, 40 mV, 60 mV, 80 mV, and 100 mV of cell membrane voltage changes. HEK293 cell clusters were then imaged through brain tissue of the determined maximum thickness. The calculation of CNR for figure 4a includes the following steps:

(1) We define the background:

backgr = mean (PA amplitudes outside the cell area).

(2) We define signals from the cell area:

signal = mean((PA amplitude>= backgr) within the cell area).

(3) We define the baseline signals from the cell area:

base = mean((PA amplitude < backgr) within the cell area).

(4) We define noise as the standard deviation within the background area:

noise = stdev(PA amplitudes outside the cell area).

(5) Last, we calculate the CNR:

CNR = (signal-base)/noise.

5.3 Results

5.3.1 Photoacoustic Imaging of Live Cell Membrane Potentials and Phantom Study

Hydrophobic anions, such as DPA and sodium tetraphenylborate (TphB), have extremely strong adsorption to plasma membranes, and their adsorption and transport mechanism in the lipid bilayer membrane have been well studied[115,116]. So far, DPA has been found to induce voltage-dependent membrane capacitance in the squid giant axon[29] and to report neuron cell membrane potentials[117-123] in fluorescence imaging. We wondered if it could be used as a voltage sensor for photoacoustic tomography. Thus, we conducted an *in vitro* HEK293 cell imaging experiment with a transmission mode optical-resolution photoacoustic microscope (Figure 5.1), as detailed in the Methods. With 0.3 NA objective, the PA images of HEK293 cells stained with DPA shows the dyes enhanced the PA signals of cell membrane. With the increased cell membrane potential, the PA signals of the cells also increased (Figure 5.5).

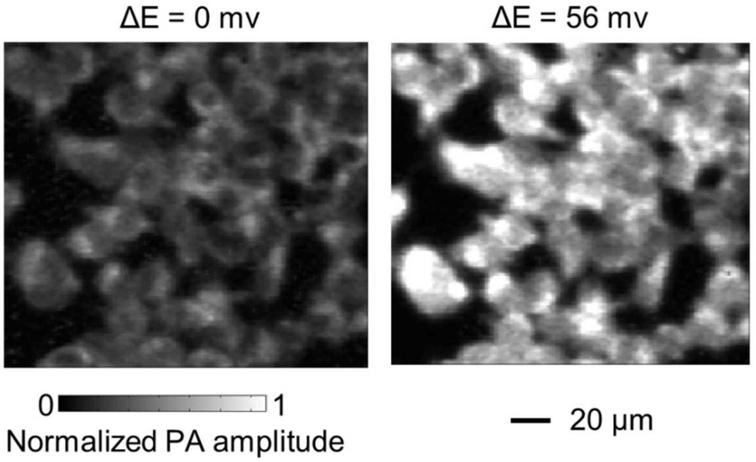

Figure 5.5 PAM of HEK293 cells stained with DPA at different membrane potentials

To quantify the relationship between PA signal change and cell membrane potentials, we measured the PA signals from a group of HEK293 cells at a series of different cell membrane potentials(Figure 5.6). The dashed ellipse in Figure 5.6(a) identifies a HEK293 cell cluster. The larger the HEK293 cell membrane resting potential change, the larger the photoacoustic signal change. Figure 5.6(b) quantifies the fractional photoacoustic signal changes due to cell membrane voltage changes estimated from the Nernst equation. First, we calculate the averaged PA signal for cells within the dashed ellipse for each image. Second, we compute the fractional PA signal change by normalizing the PA signal change by the initial PA signal under the initial membrane potential. A fractional photoacoustic signal increase greater than 40% was recorded for a 100 mV membrane resting potential change. Because the Nernst equation overestimates voltage change[114], an even larger fractional photoacoustic signal change was expected for a given membrane resting potential change. It is worth noting that we might have a slightly different PA voltage response curve in Figure 5.6(b) if the more accurate Goldman equation is used. Pursuing quantitative PA voltage imaging, which requires further calibration experiments with a voltage clamp instrument, is beyond our current scope.

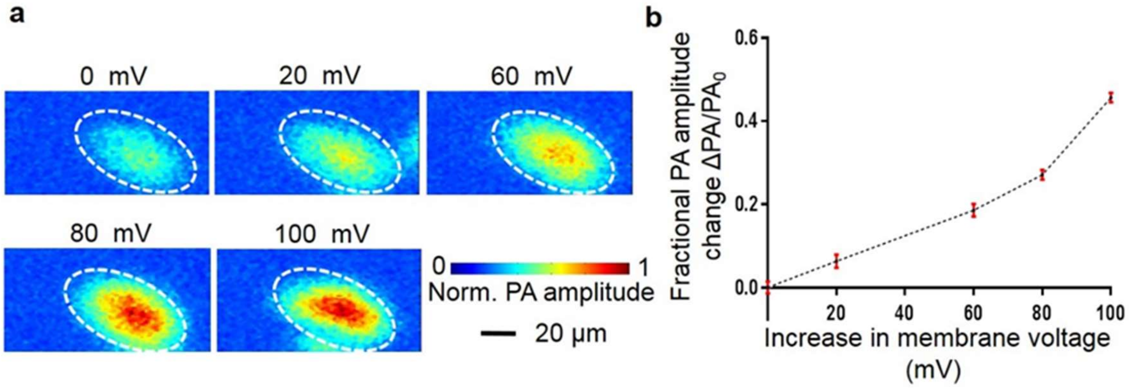

Figure 5.6 PAM of live HEK293 cells at different membrane potentials (a) Photoacoustic maximum-amplitude projection images of HEK293 cells demonstrate photoacoustic signal changes due to cell membrane voltage changes. (b) Fractional photoacoustic signal change versus cell membrane resting voltage changes.

The PA signal can be written as $p = \alpha\xi\Gamma m\mu F$, where p denotes the PA signal, α is a spatially dependent factor, ξ is a coefficient representing the distortion and attenuation of the photoacoustic signal, Γ denotes the Grüneisen parameter of the medium, m denotes the molar concentration of DPA, μ denotes the molar optical absorption coefficient of DPA, and F denotes the local optical fluence in J/m^2. Because α, ξ, Γ, and F are parameters not affected by plasma membrane voltage, the PA voltage response contrast must originate from either the molar concentration (m) or the molar optical absorption coefficient (μ). In the case of the voltage-dependent molar optical absorption coefficient (μ), a voltage-dependent optical absorption spectrum is expected. To investigate whether the voltage-sensitive mechanism is due to the molar optical absorption coefficient (μ), we performed photoacoustic spectroscopy of the DPA-stained HEK293 cell membrane under two different resting potentials.

To investigate whether the voltage-sensitive mechanism is due to μ, we first varied the excitation wavelength of the OPO laser from 400 nm to 570 nm to acquire the PA spectrum of DPA molecules stained on the HEK293 cell membrane under a 0 mv membrane potential. Next, we acquired the PA spectrum under a 56 mv membrane potential after the external K+ concentration was adjusted. Figure 5.7 shows two normalized PA spectra of DPA molecules in the HEK293 cell membrane between 400~570 nm for 0 mv (blue solid line) and 56 mv (red dashed line) cell membrane potentials. The error bars identify the standard deviation of the measurements. Statistically, we conclude that the normalized PA absorption spectrum remains unchanged when the two different membrane potentials are applied.

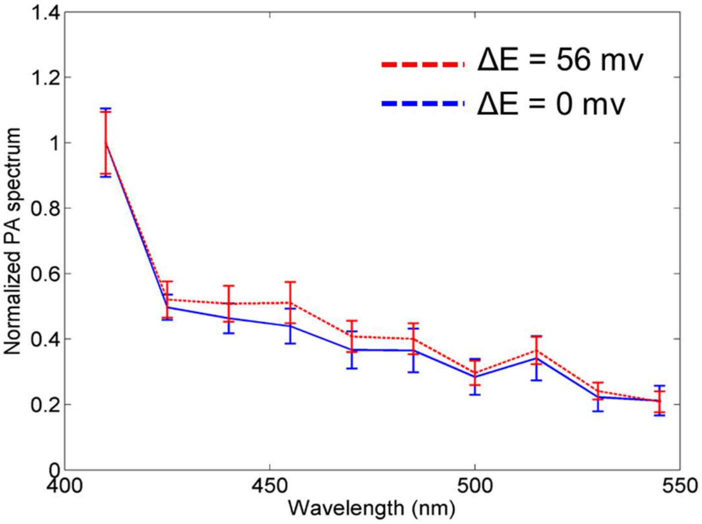

Figure 5.7 PA spectrum of HEK293 cells stained with DPA. (a) PA images of HEK293 cells at a wavelength of 488nm for 0 mv and 56 mv cell membrane potentials. (b) Two normalized PA spectra between 400 – 570 nm.

Therefore, we concluded that the normalized photoacoustic absorption spectrum did not change with membrane voltage, which leaves, as the other hypothesis, that the molar concentration (m) of DPA in lipid membrane is voltage-dependent. This voltage sensitive mechanism is very close to repartitioning[18], a fluorescent voltage sensitive scheme that solely involves dye molecules moving in and out of the lipid membrane with voltage changes. The only difference is that the dye molecules involved here are non-fluorescent.

To further prove the DPA voltage contrast mechanism, we performed another experiment based on spectrophotometry instead of photoacoustics. We stained HEK293 cells with 5 μM DPA solutions with different K^+ concentrations. The total number of DPA molecules, including DPA adsorbed onto plasma membrane and DPA in solution, remained constant. By quantitatively measuring the DPA molecules left in the solution with spectrophotometry, we calculated the DPA molecules adsorbed to the membrane under different membrane voltages. The number of DPA molecules adsorbed on HEK293 cell membranes equals the total number of DPA molecules minus the number of DPA molecules in the solvent. The number of DPA molecules in the solvent was measured by a spectrophotometer after centrifuging and sampling operations. The measurement results, shown in Figure 5.8, agree with the photoacoustic measurement results. More DPA molecules are adsorbed to cell membranes as the cell membrane voltage change increases.

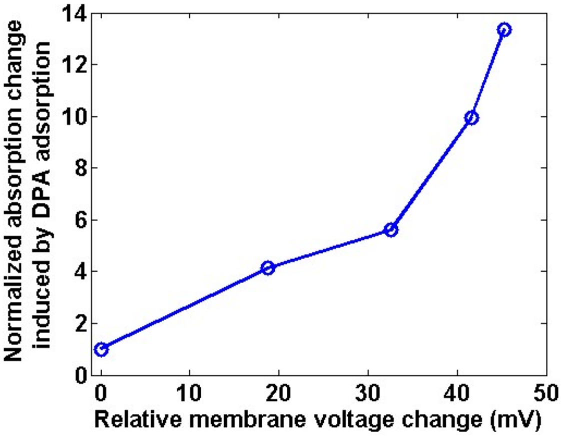

Figure 5.8 Normalized DPA absorption change versus relative membrane voltage change

Both spectrophotometric results and photoacoustic results agreed well. Thus, the spectrophotometry confirmed repartitioning, i.e., that more DPA molecules are adsorbed to the cell membrane when the resting potential change is higher, which leads to stronger photoacoustic signals. Finally, we conclude that repartitioning of DPA molecules is the voltage sensitive mechanism behind the PA voltage response contrast. This type of voltage sensitive mechanism is considered not fast enough for imaging dynamic action potentials of neurons. The frequency response of the DPA dye could be modeled as the low-pass filtered frequency response of an ordinary voltage dye.

Calculating blood and DPA concentration in mixed solutions in tubes To prove the accuracy of differentiating blood and DPA signals spectrally using our theories, we perform the phantom study for mixtures of blood and DPA. A 20 mM DPA solution was purchased from Biotium Inc. Lysed bovine blood was purchased from QuadFive.com. DPA and blood mixture phantoms were made by mixing varied concentrations of DPA in a diluted lysed blood solution and injecting it into a laboratory tube (CAT. No. 508-001, Dow Corning) with 0.3 mm inner diameter and 0.64 mm outer diameter. The preset DPA molar concentrations and blood volume concentrations for two groups of phantoms are shown in table 1.

Table 5.1 Preset DPA and blood volume concentrations for two groups of phantoms

Group 1	**Tube 1**	**Tube 2**	**Tube 3**	**Tube 4**	**Tube 5**
DPA	0 mM	0.1 mM	0.2 mM	0.5 mM	1.0 mM
Blood	10%	10%	10%	10%	10%
Group 2	**Tube 6**	**Tube 7**	**Tube 8**	**Tube 9**	**Tube 10**
DPA	0.2 mM	0.2 mM	0.2 mM	0.2 mM	0.2 mM
Blood	10%	90%	20%	40%	80%

We performed calibration with two phantoms in each group and plotted both preset points and measured points in 2D concentration-space. Figure 5.9 shows the measured DPA molar concentration of tubes of group 1 versus the preset values. Figure 5.9b shows the measured volume concentrations of blood in tubes of group 2 versus the preset values. The phantom experimental results prove that our method of separating DPA and blood signal is valid.

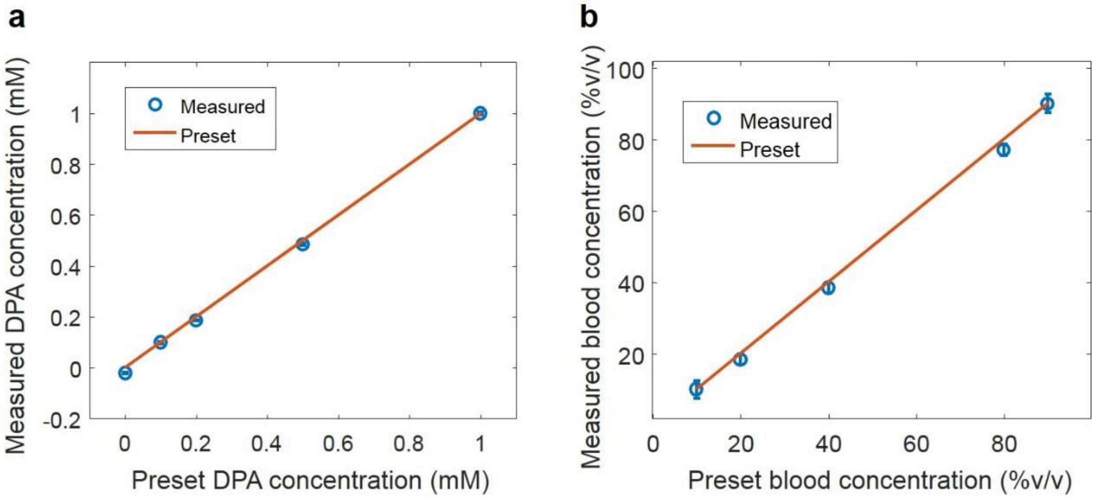

Figure 5.9 Measured DPA and blood concentrations versus preset values

Estimating DPA concentration in cell membranes in vivo For *in vivo* experiments, 20 µM DPA was used to stain mouse brain through the cranial window. However, the effective DPA concentration on the brain surface was significantly higher than 20 µM because of the strong adsorption of DPA by the lipid membrane. To estimate the effective DPA concentration in lipid membrane, the ratio of the PA signal from 1 mM DPA dye and the PA signal from 20 µM DPA stained lipid membrane of HEK293 cells was measured as 8.3. Thus, the effective DPA concentration of the 20 µM DPA stained lipid membrane is 1 / 8.3 = 0.12 mM. Next, we performed phantom experiments to test our method for separating DPA and hemoglobin signals.

5.3.2 *In Vivo* Mouse Brain Surface Voltage Response to Electrical Stimulation

Although DPA voltage dye is slow, we still could use it to record voltage responses in mouse brains *in vivo*. One obstacle for PA voltage response imaging is the interference of hemoglobin in blood. Deán-Ben XL *et al.* reported *in vivo* PAT imaging of GCaMP5G (a genetic calcium indicator) zebrafish[37]. However, the contributions of hemoglobin and GCaMP5G in the PA signal were mixed because of the well-known neuronal-vascular coupling effect. Here, we considered a simplified case where the imaging target is the DPA stained dura layer immediately beneath the mouse skull instead of neuron circuits inside the live brain. The laser fluence in the imaging voxel, which includes both the dura and cortex tissue, is a constant after normalization against the photodiode recording of laser pulse energy. For this simplified case, a spectroscopic method provides exact solutions for both the hemodynamic signal, and voltage response signal, as detailed in the Methods section. The analysis of calculation error presented in the SI, section VII, shows that the calculation errors are less than 1.5 times the noise. This spectroscopic voltage response imaging method is very similar to the spectroscopic oxygen saturation imaging method[38-39] that was first verified with *in vitro* phantoms and then applied to *in vivo* applications. The technical verification experimental results for the spectroscopic voltage response imaging method are provided in the SI, section V. The voltage response signal is a low-pass filtered local field potential signal, which has a high similarity within a relatively large area. Thus, we expect that motion artifacts caused by respiration have minor effect on the measured voltage response signal.

As we know, electrical stimulation can change the neuronal membrane voltage and trigger a neuronal response to extracellular electrical currents near the neuron[124-126]. This stimulation approach has been used to identify the motor cortex, map neural connections between brain regions, modulate attention, increase the speed of learning, identify neural subtypes, record movement sequences, study somatosensory perception, and introduce signals directly into the brain in brain-machine interface models. It was shown that micro-electrical stimulation sparsely activates neurons around the electrode up to millimeters away from the point of stimulation[124]. Although we have a limited understanding of the effects of electrical stimulation on individual neurons, it serves well for our purpose of voltage response signal imaging. DPA dye was applied outside the intact dura matter. The depth-resolved photoacoustic microscopy image indicated that photoacoustic signals come from the surface of the brain, including micro-vessels within the M-mode imaging voxel volume, where the laser fluence is a constant after normalization against the photodiode recording of the laser pulse energy.

We also investigated the PA signal ratio between blood vessels and DPA stained tissues to make sure that PA signals are not overwhelmed by the hemoglobin signals at 500 nm. Figure 5.10 compares the brain images at 500 nm before and after 20 μM DPA dye staining. The PA signal change due to DPA dye staining is obvious because of the strong lipid membrane adsorption effect. The mean PA signal before staining, from region d1, is dominantly from capillary blood vessels. For region d1, the mean PA signal after DPA staining is dominantly from capillary blood vessels and adsorbed DPA dyes. Thus, the dye signal at 500 nm is 730-603 = 127 (a.u.). We can estimate the ratio of the hemoglobin signal to the DPA signal within region d1 as Equation (5.8).

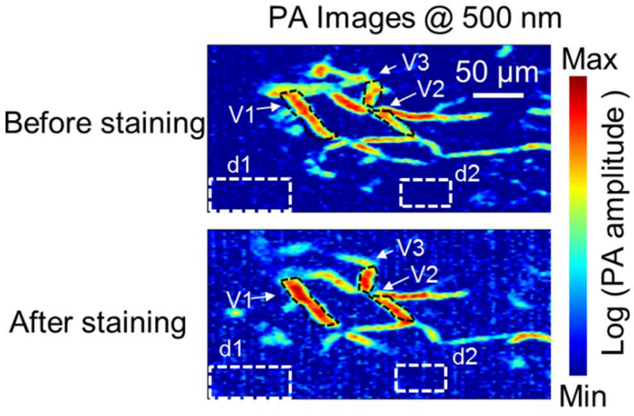

Figure 5.10 Effects of DPA staining on mouse cranial window

$$\frac{PA_{Hb500}}{PA_{DPA500}} = 603/127 = 4.7 \tag{5.8}$$

We can estimate the ratio at 570 nm from the known absorption curves of Hb and DPA:

$$\frac{PA_{Hb570}}{PA_{DPA570}} = \frac{PA_{Hb570}}{PA_{Hb500}} \times \frac{PA_{Hb500}}{PA_{DPA500}} \times \frac{PA_{DPA500}}{PA_{DPA570}} \tag{5.9}$$

$$\frac{PA_{Hb570}}{PA_{DPA570}} = \frac{\mu_{aHb570}}{\mu_{aHb500}} \times \frac{PA_{Hb500}}{PA_{DPA500}} \times \frac{\mu_{aDPA500}}{\mu_{aDPA570}} = 2.143 * 4.7 * 19.8 = 200 \tag{5.10}$$

At 570 nm, the hemoglobin signal is dominant. However, at 500 nm, the DPA dye contribution is significant. With the spectroscopic method, the contributions from Hb and DPA can be separated. At other labeled areas of Table 5.2, the ratio of $\frac{PA_{Hb500}}{PA_{DPA500}}$ at 500 nm varies from 3.3 to 6.6.

Table 5.2 PA signals of blood vessels before and after staining with DPA

Mean PA signals (a.u.)	**d1**	**d2**	**v1**	**v2**	**v3**
Before	603	557	2469	2171	2652
After	730	677	3089	2826	3053
Difference	127	120	620	655	401
Ratio (Before/Diff.)	4.7	4.6	4.0	3.3	6.6

The fact that PA signals from DPA stained tissue are not overwhelmed by the hemoglobin signals at 500 nm allows the separation of the voltage response signal from the hemoglobin signal.

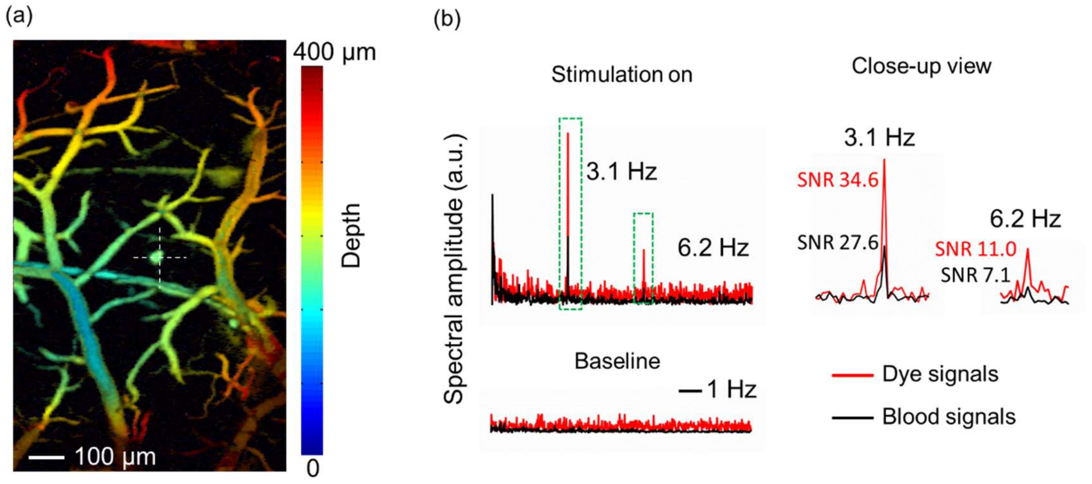

Figure 5.11 *In vivo* PA response of mouse brain before and during electrical stimulation at a minimally vascularized point. (a) The exact M-mode imaging location is identified by the yellow cross in the depth-coded maximum amplitude projection image of the DPA-stained mouse cranial window. (b) A 63 second stimulation sequence comprises 189 electrical stimulation pulses with a pulse width of 300 µs and a pulse period of 333 ms. (c) Baseline (before electrical stimulation) and response (during stimulation) of voltage and hemodynamic signals in the frequency domain. Both the voltage response signal (red) and hemodynamic response signal (black) have observable frequency components at 3.1 Hz and 6.2 Hz. The SNRs of the voltage and hemodynamic response peaks are respectively labeled with red and black text.

Then, we recorded *in vivo* mouse brain responses before and during electrical stimulation at a point with minimum vasculature. In Figure 5.11(a), the exact M-mode imaging location is identified by the yellow cross in the depth-coded maximum amplitude projection image of the DPA-stained mouse cranial window. Figure 5.11(b) shows a 63-second electrical stimulation sequence that comprises 189 electrical stimulation pulses with a pulse width of 300 µs and a pulse period of 333 milliseconds. There are no observable features in either the baseline (before electrical stimulation) or response (during stimulation). We analyzed the baseline and response of the voltage and hemodynamic signals in the frequency domain. Compared to the noise-like baseline signals, both the voltage response signal (red) and hemodynamic response signal (black) have observable frequency components at 3.1 Hz and 6.2 Hz, as shown in Figure 5.11(c). The signal-to-noise ratios (SNR) of the voltage and hemodynamic response peaks are labeled with red and black text, respectively, next to the peaks. Because the voltage response signal (red trace) is stronger than hemodynamic signal for both frequency components, the voltage response is dominant at this minimally vascularized M-mode imaging point.

On the other hand, we can also estimate the PA signal response under electrical stimulation. We assume the single pulse electrical stimulation function is written as:

$$g(t) = \begin{cases} A, & |t| \leq \frac{T}{2} \\ 0, & |t| > \frac{T}{2}. \end{cases} \tag{5.11}$$

The Fourier-transformation of $g(t)$ is the frequency-domain signal:

$$G(f) = AT\frac{\sin(\pi f T)}{\pi f T} \tag{5.12}$$

The electrical stimulation pulse train is written as the convolution of $g(t)$ with a comb function:

$$h(t) = g(t) * comb(t) \tag{5.13}$$

$$comb(t) = \sum_{n=-\infty}^{+\infty} \delta(t - nT') \tag{5.14}$$

Here T is 300 μs and T’ is 333 ms, so $\frac{1}{T'}$ is 3 Hz. The Fourier-transformation of the pulse train h(t) is

$$H(f) = G(f)\,\frac{1}{T'}\,\sum_{k=-\infty}^{+\infty} \delta\left(f - k\frac{1}{T'}\right) \tag{5.15}$$

$$H(f) = AT\frac{\sin(\pi f T)}{\pi f T}\,\frac{1}{T'}\,\sum_{k=-\infty}^{+\infty} \delta\left(f - k\frac{1}{T'}\right) \tag{5.16}$$

Thus, the pulse train stimulation has frequency components only at $k\frac{1}{T'}$, which is an integer multiple of 3 Hz. If we model the voltage response of DPA dye on the dura layer as a linear low pass filter for all frequency components less than 8 Hz, we end up with two frequency components at 3 Hz and 6 Hz. Our analysis based on the model agrees with the observed PA voltage response peaks at 3.1 Hz and 6.2 Hz. The experimental results have clearly shown that DPA is a slow dye, which is not suitable for dynamic action potential imaging experiments.

5.3.3 *In Vivo* Mouse Brain Voltage Response Signal Imaging Before and During 4-aminopyridine-induced Epilepsy

The drug 4-aminopyridine (4-AP) was used to induce epileptic seizure in various models of epileptic seizure[127-131]. Epileptiform activity has been extensively studied using different optical imaging methods[132-141]. Among these, photoacoustic tomography has the potential to record deep brain voltage response signals and hemodynamic signals in parallel and to become a new tool for understanding the induction, maintenance, and propagation of seizure discharges. Here, in an animal model, we demonstrated the recording of both neuronal and hemodynamic responses to epileptic seizure induced by 4-AP.

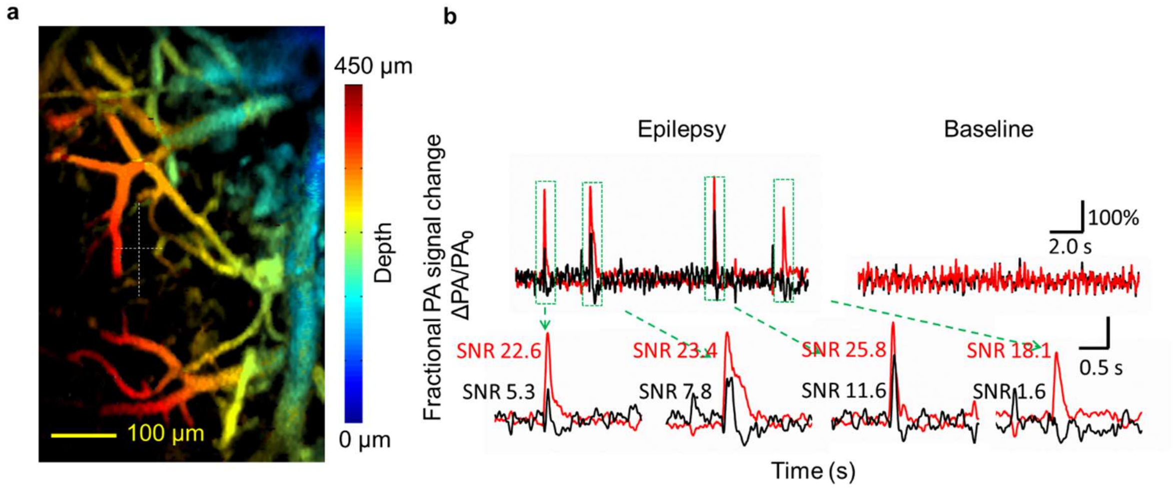

Figure 5.12 *In vivo* mouse brain response before and during epilepsy. (a) The white cross identifies the M-mode recording point on the depth-encoded maximum amplitude projection image of the mouse brain through the cranial window. The color represents depth. (b) Fractional voltage and fractional hemodynamic signal changes in the time domain for the baseline (before 4-AP stimulation) and response (during 4-AP induced epilepsy). The SNRs of the voltage and hemodynamic response peaks are labeled with red and black text. The fractional voltage response signal change shows stronger responses (spike amplitudes) than the fractional hemodynamic signal change.

Figure 5.12 shows a maximum amplitude projection image of a mouse brain through a skull window after staining with DPA. The white cross identifies the location of M-mode imaging. Figure 5.12(b) shows the calculated fractional photoacoustic voltage response signal change (red trace) and the fractional hemodynamic signal change (black trace) before and after 4-AP induced epilepsy. Before the induction of epilepsy, both the fractional voltage response signal change and the fractional hemodynamic signal change show no observable events. However, the induced epilepsy after the injection of 4-AP within the skull window generated significant spikes at the same M-mode imaging location. We recorded a fractional photoacoustic voltage response signal change of more than 300% and a fractional photoacoustic hemodynamic signal change of more than 200%. We hypothesize that the significant voltage response signal change could be due to synchronized neuronal firing during 4-AP induced epilepsy and that the significant hemodynamic signal change could be related to the recruitment of capillaries during epilepsy and the neuronal-vascular coupling. We note that the voltage-sensitive mechanism of DPA dye reflects its voltage-dependent adsorption to the lipid membrane. This mechanism is considered too slow to catch the single action potentials fired by the epileptic neurons. The calculated fractional voltage response signal change that has been low-pass filtered by the DPA dye could show only the entire epileptic spike envelopes. Both the fractional voltage response signal change (red) and the fractional hemodynamic response signal change (black) show spikes that are not necessarily always synchronous. Over all, at the recording point, the fractional voltage response signal change shows stronger responses than the fractional hemodynamic signal change.

5.3.4 Imaging HEK293 Cell Clusters Through Thick *Ex Vivo* Brain Tissue

In the above two *in vivo* imaging experiments, we demonstrated PA imaging of voltage responses as a function of the brain surface voltage. In addition to the easy dye delivery and robustness against respiration-caused motion artifacts, both animal models allow exact solutions of the voltage response signal and the hemoglobin signal. *In vivo* deep brain voltage response imaging remains very challenging without a long-wavelength voltage sensor whose optical absorption spectrum can be separated from that of hemoglobin. However, the DPA voltage dye still allows us to demonstrate *in vitro* PA voltage response imaging at depths beyond the optical diffusion limit. A photoacoustic computed tomography system (see Methods) was used for this demonstration experiment.

As described in the methods section, we first imaged HEK293 cell clusters through different thicknesses of rat brain tissue. Figure 5.13(a) shows PACT images of HEK293 cell clusters acquired through 4.5 mm and 5.0 mm thick rat brain tissues. The contrast-to-noise ratios (CNR) of the cell cluster images acquired through 0.0 mm, 2.0 mm, 3.0 mm, 4.5 mm, and 5.0 mm thicknesses decrease with increasing thickness of brain tissue, as shown by Figure 5.13(b). The calculation of CNR is detailed in the Methods section. We define the cell cluster visibility threshold as CNR of at least 2. Consequently, the HEK293 cell clusters remain visible through 4.5 mm thick rat brain tissue and become invisible through 5 mm thick rat brain tissue.

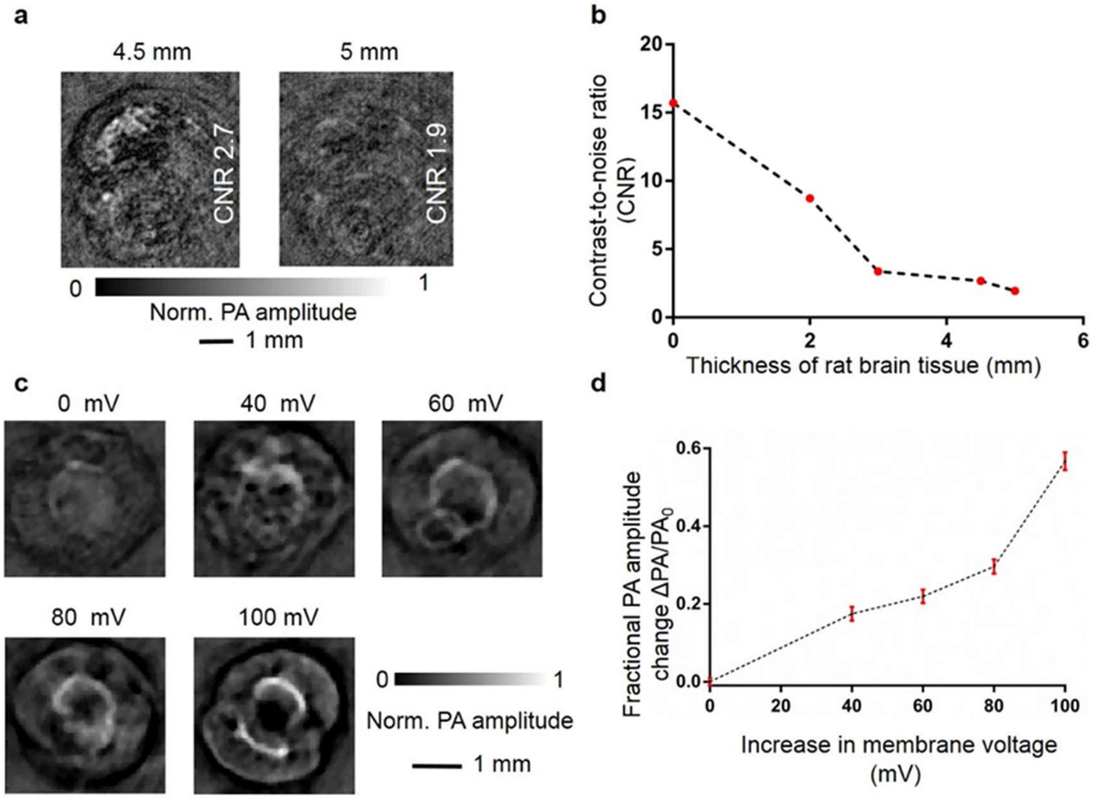

Figure 5.13 Imaging cell clusters through different thicknesses of ex vivo brain tissue with different resting potentials. (a) HEK293 cell cluster PACT images through 4.5 mm and 5.0 mm thick brain tissue. (b) The contrast-to-noise ratios of the HEK293 cell cluster images acquired through 0.0 mm, 2.0 mm, 3.0 mm, 4.5 mm, and 5.0 mm thick brain tissue decrease as the brain tissue thickness increases. (c) Photoacoustic images of HEK293 cell clusters acquired through 4.5 mm thick brain tissue in response to cell membrane voltage changes. (d) Fractional photoacoustic signal change versus cell membrane voltage change.

Second, we imaged HEK293 cell clusters in response to different cell membrane voltage changes through 4.5 mm thick rat brain tissue. In Figure 5.13(c), stronger photoacoustic signals were observed due to larger cell membrane voltage changes. The fractional photoacoustic amplitude change versus voltage change is plotted in Figure 5.13(d). There is more than a 60% fractional PA amplitude change with 100 mV of cell membrane voltage change, which might have been caused by the longer staining time when cell clusters were bathed in DPA solutions during the imaging procedures.

Our results are still limited by the sensitivity and density of the ultrasonic transducer array device. High-sensitivity, high-frequency optical sensors with excitation wavelengths outside of the hemoglobin absorption spectrum will maximize the achievable imaging depth of PACT imaging.

5.4 Conclusions and Discussion

We report the first demonstration of photoacoustic voltage response imaging in both *in vitro* HEK293 cell cultures and *in vivo* mouse brain surfaces. Using spectroscopic photoacoustic tomography at isosbestic wavelengths, we separated voltage response signals and hemodynamic signals on live brain surfaces. By imaging HEK293 cell clusters through 4.5 mm thick *ex vivo* rat brain tissue, we demonstrated photoacoustic tomography of HEK293 cell membrane voltage responses beyond the optical diffusion limit. Although the current voltage dye does not allow *in vivo* deep brain voltage response imaging immediately, we believe our method opens up a feasible technical path for deep brain studies in the future.

Chapter 6 Photoacoustic Calcium Imaging with a Genetically-encoded Indicator

In addition to voltage indicators, calcium indicators are also popular indicators for neural imaging. Though calcium signals cannot faithfully represent membrane voltage changes, they are closely associated with neural activities. With a large absorption coefficient and a strong signal change, calcium indicators are widely used for measurements in highly scattering media. However, their use for photoacoustic imaging was not demonstrated before this work. In this chapter, we use PAM and PACT systems for calcium imaging with a genetically encoded indicator, GCaMP, and achieve calcium imaging in a fly brain and live mouse brain slices.

6.1 Background

Monitoring the neural activity of large populations of neurons with fine spatial and temporal resolution is arguably one of the most important challenges in neuroscience[142-144]. To achieve this goal, several multi-unit electrophysiological recording techniques [145-147] and optical imaging methodologies[148-150] have been developed in recent decades. Electrophysiological recording methods are still considered the gold standard because they directly monitor intracellular or extracellular neural signals from individual neurons or small groups of neurons with high sensitivity and temporal fidelity[151]. Complementing these techniques, noninvasive optical imaging techniques that allow larger spatial coverage with finer spatial resolution have been used to study computations performed by neural networks[148,152,153]. In particular, two-photon microscopy, combined with fluorescent calcium and voltage indicators, has enabled optical mapping of neural circuits from hundreds to thousands of neurons, with high spatiotemporal resolution in optically scattering brain tissue[150,154-157]. However, several limitations still exist. For example, the point-by-point scanning of confocal microscopy and two-photon microscopy creates a tradeoff between spatial coverage and temporal resolution. More importantly, light scattering in the neural tissue fundamentally restricts the current optical neural imaging methods to the superficial tissue layer (~1 mm)[59,158] To address this issue, invasive techniques using deeply implanted fiber-optic probes have been recently used to image non-superficial regions inside the mouse brains[159-162]. Therefore, there is a strong need for noninvasive optical imaging methods that can break the optical diffusion limit and provide rapid depth-resolved monitoring of neural activity.

Alternative to conventional optical imaging methods, photoacoustic tomography (PAT) has been demonstrated as a powerful brain imaging technique capable of providing high-resolution images with optical absorption contrast at depths far beyond the optical diffusion limit[59,163,164]. Briefly, PAT is based on the photoacoustic (PA) effect, which starts with optical absorption by molecules in tissue and ends with ultrasonic emission through thermoelastic expansion[59]. Similar to ultrasound imaging, PAT has inherent depth-resolved imaging capability based on the acoustic arrival time or acoustic focusing. Because PAT is sensitive to optical absorption contrast (both endogenous and exogenous), it is well suited for functional, molecular, and metabolic brain imaging[165]. In addition, PAT is highly scalable in its spatial resolution, penetration depth and imaging speed. Previous endeavors in PA brain studies have focused on measuring hemodynamic parameters, including the blood vessel diameter, blood flow, total hemoglobin concentration, and the oxygenation saturation of hemoglobin[166-178], which are usually slow and indirect indicators of neural activities through neurovascular coupling[179]. In contrast, intracellular calcium signals respond to neural activities faster than hemodynamic signals, and can be recorded optically with the help of intracellular calcium indicators[180]. Among all the calcium indicators, GCaMP, with its relatively fast conformational change upon calcium binding during action potentials, is by far the most widely used genetically encoded calcium-sensitive protein[181]. The conformational change of GCaMP results in a substantial increase in its optical absorption, which is ideal for PAT imaging of calcium signals with high sensitivity. Still, it is yet to be determined whether experimental results support this hypothesis and how the PA signals compare to the fluorescence signals.

Here, for the first time, we clearly demonstrate that PAT can be used to monitor neural activities in select neurons expressing GCaMP indicators in transgenic invertebrate (fly) and vertebrate (mouse) models expressing GCaMP indicators in selected neurons. To accommodate different spatial scales, we adapted two PAT embodiments—photoacoustic microscopy (PAM) and photoacoustic computed tomography (PACT). With PAM, we demonstrate high-resolution depth-resolved neural imaging without depth scanning, which is desired for monitoring neural activities with high temporal resolution. With PACT, we demonstrate wide-field imaging of GCaMP calcium signals at depths beyond the optical diffusion limit. The combination of PAT and GCaMP or other potential calcium indicators provides a promising platform for functional brain imaging at different spatial scales.

6.2 Methods

PAT of neuronal calcium signals with GCaMP In PAT, as tissues are excited by laser pulses, laser energy is absorbed by biomolecules, and converted through both the fluorescence channel by radiative relaxation and the PA channel by non-radiative relaxation. An ultrasonic transducer or transducer array is used to detect the PA waves as they propagate out of the tissue. The detected

PA signals are used to reconstruct an image that maps the original optical energy deposition due to non-radiative relaxation in the tissue.

Based on the image formation methods, PAT has two major implementations. The first combines mechanical scanning of a focused single-element ultrasonic transducer with direct image formation, and is commonly used in PAM. The second combines parallel detection by a multi-element ultrasonic transducer array or a mechanical/electronic scanning equivalent with image reconstruction, and is used in PACT. In both PAM and PACT, the PA amplitude is proportional to the optical absorption coefficient of the absorber in the unit of m^{-1}, its non-radiative quantum yield (approximately equal to 1 – the fluorescence quantum yield if the photochemical channel is negligible), and the local optical fluence (or exposure) in the unit of J/m^2.

Two GCaMP variants were used in this study, GCaMP5G for fly brain imaging, and GCaMP6f for mouse brain slice imaging. In general, GCaMP consists of a circularly permuted EGFP, an M13 fragment of myosin light chain kinase, and a calcium binding site of calmodulin. Action potentials trigger a large and rapid influx of Ca^{2+} [182]. In the presence of calcium, calmodulin interacts with the M13 fragment, eliciting a conformational change in EGFP and resulting in an increase in its optical absorption coefficient [183,184]. Because the PA signal of GCaMP is proportional to its absorption coefficient, PAT has a 100% sensitivity to the absorption change of GCaMP upon the binding of Ca^{2+}.

PAM of the fly brain *in vivo* A dual-modality PA and epi-fluorescence microscopy system shown schematically in Figure 6.1(a) was used to image the fly brain. A tunable OPO laser (a 1-kHz pulse repetition rate, 5-ns pulse width; NT242-SH, Ekspla, Ltd.) provided 488-nm–wavelength excitation light, which was collimated and coupled into a miniature imaging probe containing an achromatic focusing lens with a 13-mm focal length and a customized ring-shaped ultrasonic transducer (a 40-MHz central frequency, ~100% bandwidth, and 6.2-mm focal length). The laser beam formed a 6-µm optical focal spot confocally aligned with the acoustic focus of the ring transducer. The axial resolution of the PAM, determined by the ultrasonic transducer bandwidth, was calculated to be ~21 µm [185]. A beam splitter reflected the fluorescent light for fluorescence imaging. The fluorescent light passed through another focusing lens (a 50-mm focal length) and a bandpass filter (a 525-nm central wavelength, 39-nm bandwidth; Thorlabs, Inc.) before being collected by an EMCCD camera (iXon Ultra 888, Andor, Ltd.). PA signals were sampled by a 200-MHz data acquisition (DAQ) system (National Instruments, Corp.), and fluorescence signals were recorded by the EMCCD camera's onboard DAQ system. For each M-mode recording, PA signals before and after odor stimulation from a volume (~6 µm × ~6 µm × ~200 µm) of neurons inside the brain tissue were acquired at a 1D imaging rate of 1 kHz. To form a 3D image of the fly brain, 2D raster scanning was performed by motor stages. A photodiode (not shown) was used to compensate for the laser pulse energy fluctuation.

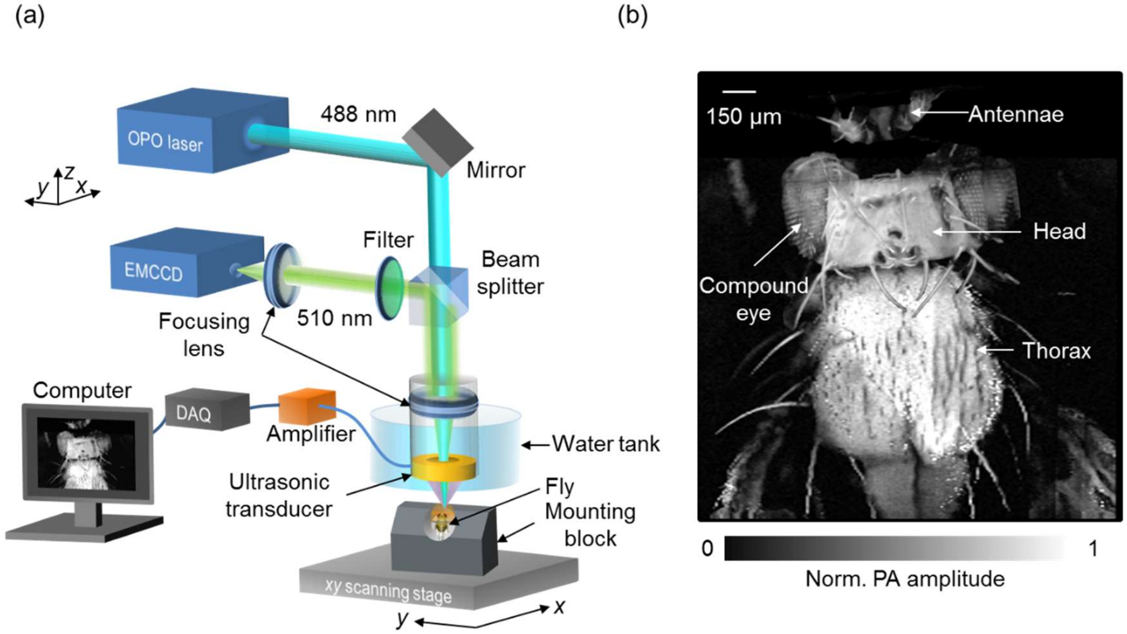

Figure 6.1 PAM of the GCaMP5G-expressing fly brain. (a) Schematic of the dual-modality PAM and epi-fluorescence microscopy (EFM) system. PAM and EFM share the same light path for excitation. While the photoacoustic (PA) signal is detected by a ring-shaped ultrasonic transducer, the fluorescence signal is detected by an EMCCD. (b) PAM image of a fly with endogenous contrast, showing the major parts of the fly, including the antennae, compound eyes, head, and thorax. The PA signals mostly come from pigments (e.g., melanin) on the fly cuticle.

Fly preparation and odor stimulation GCaMP5G flies were purchased from the Bloomington Drosophila Stock Center at Indiana University. Flies were anesthetized by CO_2 until their movement stopped, and were moved to a customized fly mount (a block setup[186] or a foil setup[187]). For the block setup(Figure 6.1(a)), the fly was mounted and head-fixed using a two-component silicone glue (KWIK-SIL, World Precision Instruments, Inc.). A thin wire was used to pull the antennae plate forward and make space between the antennae plate and the head. A small rectangular hole was created on the bottom of a 60 mm × 15 mm petri dish (Falcon®, Corning, Inc.). Four sections of double-sided tape were used to create a rectangular window slightly larger than the head of the fly. The petri dish with the small rectangular open window at the bottom was placed on top of the fly's head and fixed onto the mounting block by double-sided tape. The interior rectangular edges were then sealed with two-component silicone glue. For the foil setup, a piece of aluminum foil was glued to the top of a supporting plate. A 60 mm × 15 mm petri dish (Falcon®, Corning, Inc.) with its bottom removed was attached to the top of the supporting plate to form a saline chamber. A hole was made in the foil according to the fly's size. The fly was then wedged into the hole with its dorsal side facing upwards. The gap between the fly and foil was sealed using epoxy (Permatex, Inc.). The ventral side, especially the antennae, of the fly was kept underneath the foil. The fly was then transferred to the PA/fluorescence imaging setup for experiments with the cuticle intact.

For experiments with the cuticle removed, a fine forceps (Dumont #5sf, Fine Science Tools, Inc.) was used to cut and remove the cuticle above the brain. Connective tissue and the trachea above the brain were also removed. The petri dish was then filled with fly Ringer's solution (103 mM NaCl, 3 mM KCl, 5 mM TES, 10 mM trehalose, 10 mM glucose, 9 mM sucrose, 26 mM $NaHCO_3$, 1 mM NaH_2PO_4, 1.5 mM $CaCl_2$, 4 mM $MgCl_2$, adjusted to 275–280 mOsm, bubbled with 95% O_2/5% CO_2) for acoustic coupling. Note that both during the preparation and during olfactory stimulation experiments, the antennae remained completely dry. A constant air flow (carrier stream; 0.8 L/min) was maintained across the fly antenna. For odor stimulation, a constant volume of headspace (0.5 L/min) above an odor bottle containing ethyl acetate was injected into the carrier stream.

PACT of acute mouse brain slices An optical parametric oscillator (OPO) laser (basiScan, Spectra-Physics, Inc.), pumped by an Nd:YAG laser (Qsmart 850, Quantel, Inc.), provided 488-nm-wavelength pulses with a 10-Hz pulse repetition rate. The laser beam was homogenized by an optical diffuser (EDC-5, RPC Photonics, Inc.). The PA signals were detected by a full-ring ultrasonic transducer array (Imasonic, Inc.) with a 10-cm diameter, 5-MHz central frequency, >90% one-way bandwidth, and 512 elements. Each element (20-mm height, 0.61-mm pitch, and 0.1-mm inter-element space) was cylindrically focused to produce an axial focal length of 40 mm (acoustic NA: 0.25). The combined foci of all 512 elements formed a field of view of ~20 mm diameter with an approximately isotropic in-plane resolution of ~100 µm, while the elevational resolution was ~1 mm. The wide-field imaging exposure time was under 20 µs with a frame rate of 10 Hz. The raw data from each element was first Wiener deconvolved to account for the ultrasonic transducer's impulse response and then reconstructed based on the universal back-projection algorithm [188].

A brain slice holder made of 4% agarose was placed in the center of the imaging chamber of the PACT system. A silicone tube was used for high-potassium perfusion (150 mM KCl concentration) in the imaging chamber. During imaging, the chamber was filled with regular aCSF solution and continuously bubbled with 5% CO_2 and 95% O_2. A peristaltic pump circulated and homogenized the aCSF solution within the imaging chamber.

Brain slice preparation The protocol for mouse brain slice preparation was approved by the Animal Studies Committee at Washington University in St. Louis.

Acute coronal brain slices were prepared from 3 months old GCaMP6f (C57BL/6J-Tg) mice, which were purchased from the Jackson Laboratory. The GCaMP6f labeled mice were anesthetized with isoflurane and decapitated. The brain was removed and glued onto a vibratome (Leica VT1200s, Leica Microsystems, Inc.) specimen holder. Coronal slices (300 µm thick) were cut in ice-cold modified aCSF solution (125 mM NaCl, 25 mM glucose, 25 mM $NaHCO_3$, 2.5 mM KCl, 1.25 mM NaH_2PO_4, 0.5 mM $CaCl_2$, and 3 mM $MgCl_2$) equilibrated with 5% CO_2 and 95% O_2. Slices were then transferred to choline-based aCSF solution (92 mM choline chloride, 2.5 mM KCl, 1.2 mM NaH2PO4, 30 mM NaHCO3, 20 mM HEPES, 25 mM glucose, 5 mM Na-ascorbate, 2 mM thiourea, 3 mM Na-pyruvate, 2 mM $CaCl_2$, and 1 mM $MgCl_2$) equilibrated with 5% CO_2 and 95% O_2, incubated at 32°C for 30 min, and subsequently stored in regular aCSF solution (125 mM NaCl, 25 mM glucose, 25 mM $NaHCO_3$, 2.5 mM KCl, 1.25 mM NaH_2PO_4, 2 mM $CaCl_2$, and 1 mM $MgCl_2$) equilibrated with 5% CO_2 and 95% O_2 at room temperature for more than an hour, and imaged with the PACT system.

Wide-field fluorescence imaging of the fly brain and acute mouse brain slices Wide-field fluorescence imaging was performed on an Olympus Fluoview 1000 system (excitation wavelength at 488 nm, emission filter wavelength centered at 510 nm; Olympus, Corp.). The fluorescence images were captured by an EMCCD camera (iXon Ultra 888, Andor, Ltd.). A 10×

water immersion objective (0.3 NA, UMPLFLN, Olympus, Corp.) was used for GCaMP5G-expressing fly brain imaging. A 2× objective (0.14 NA, XLFluor2X/340, Olympus, Corp.) was used for GCaMP6f-expressing mouse brain slice imaging.

Data analysis Image processing was performed in MATLAB (Mathworks, Inc.). In all experiments, the baseline PA and fluorescence signals were calculated as the averaged signals acquired before the simulation. The fractional changes in PA and fluorescence signals, compared with the baselines values, were then calculated.

6.3 Results

6.3.1 PAM of GCaMP5G-expressing Fruit Fly Brains *In Vivo*

One challenge for imaging GCaMP in live brains with PAT is the interference signals from hemoglobin, which has a strong optical absorption at the peak wavelength of the GCaMP absorption spectrum (488 nm). To overcome this challenge [189] and unequivocally demonstrate the feasibility of GCaMP imaging with PAT, we chose a simple and well-established transgenic invertebrate model, *Drosophila melanogaster* (i.e., fruit fly), which does not have hemoglobin in its brain. For the proof-of-concept experiments, we used a transgenic fly line that expresses GCaMP5G pan-neutrally in all cholinergic neurons.

To image neural calcium signals in the fly brain, we developed a PA and epi-fluorescence dual-modality microscope (Figure 6.1(a),Methods). The dual-modality microscope can simultaneously record the odor-evoked neural activities in the fly brain *in vivo*, with an automatically co-registered field of view and complementary image contrasts. When a 488-nm–wavelength laser pulse excites the GCaMP molecules in the brain, the captured laser energy is transformed partially into fluorescence signals and partially into PA signals, with a 67% fluorescence quantum yield[190]. It is worth noting that the ultrasonic transducer in our microscope temporally resolves PA signals from different depths along the acoustic axis, and no additional depth-scanning is required. Moreover, only a two-dimensional (2D) raster scan is needed for PAM to form a 3D image. The PAM system and the epi-fluorescence microscopy (EFM) system share the same optical focusing pathway and thus have the same lateral resolution. The axial resolution of PAM is acoustically determined, while EFM lacks axial resolution over planar targets.

Using PAM, we first imaged the whole fly brain with the cuticle intact as well as the adjacent body parts. A maximum amplitude projection (MAP) image clearly shows the brain cuticle, antennae, compound eyes, and thorax (Figure 6.1(b), Methods). The strong PA signals mostly come from the pigments of the cuticle. To gain direct optical access to neurons in the fly brain, we removed the cuticle posterior to the two antennae and the underlying connective tissue surrounding the

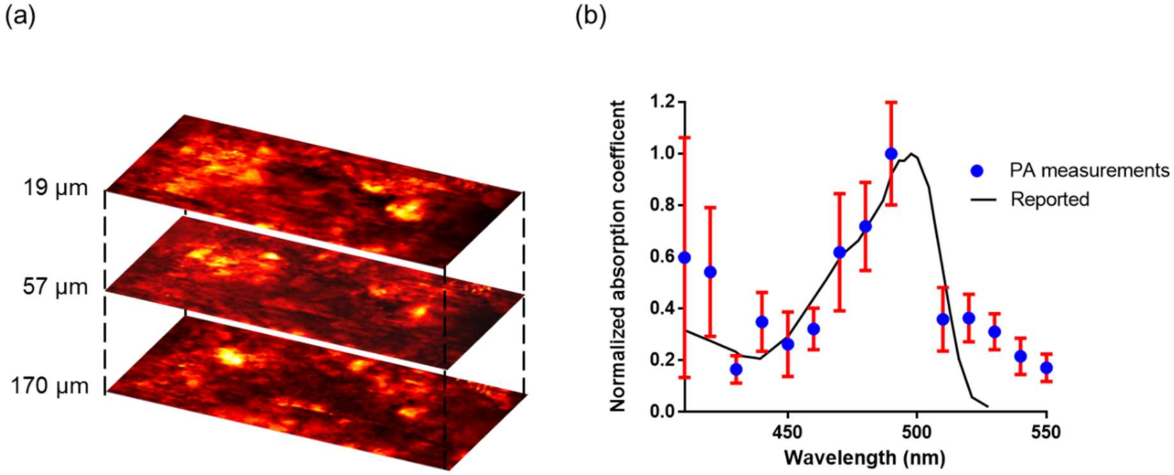

Figure 6.2 Spectral characterization of a fly brain. (a) Cross-sectional photoacoustic microscopy images of the brain at different depths, acquired at 488 nm. The cuticle was surgically removed. The labeled depths indicate the axial distances from the brain surface. (b) PA spectrum (blue dots) of the fly brain, which correlates well with the reported absorption spectrum (black curve) of GCaMP5G[190].

brain[186]. The PA depth-resolved images of the exposed fly brain show heterogeneous GCaMP expression levels in the brain (Figure 6.2(a)). The strongest PA signals came from putative neural cell bodies. To confirm that the PA signal was generated by GCaMP, we used PAM to measure the absorption spectrum of the brain tissue by tuning the laser wavelength from 410 nm to 550 nm (Figure 6.2(b)). The spectrum measured by PAM agrees well with that measured purely optically elsewhere[190]. This result is strong evidence that GCaMP is the major chromophore in the fly brain in the visible spectral range. In addition, fluorescence signals from GCaMP were simultaneously acquired by the EFM channel (Figure 6.3(a)) to further confirm the origin of the PA signals.

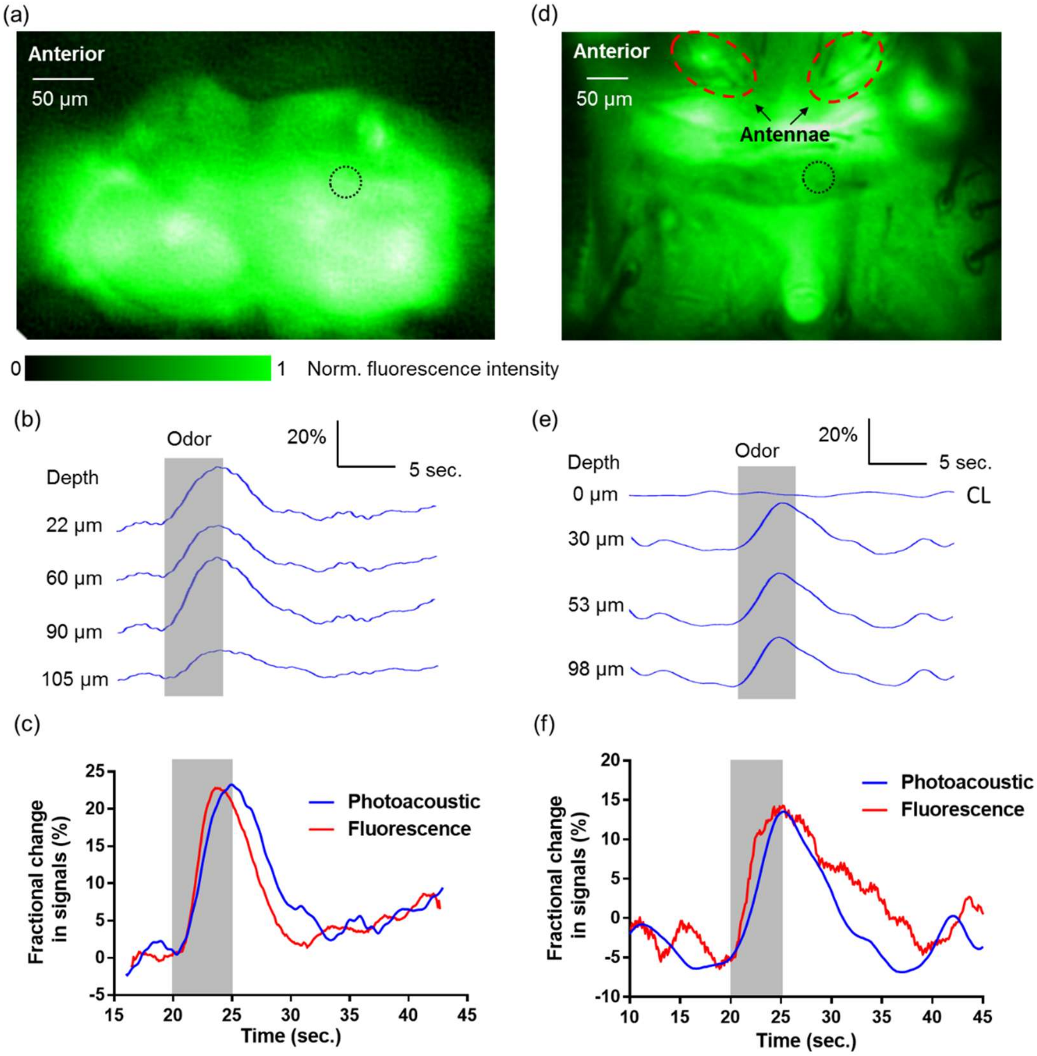

Figure 6.3 PA imaging of odor-evoked neural activity in the fly brain without and with cuticle. (a) Epi-fluorescence image of a GCaMP5G-expressing fly brain with the cuticle surgically removed. The dashed

circle identifies the lateral location of M-mode PA recording. (b) Fractional PA amplitude changes from representative neuron layers in the glomerular region of the fly antennal lobe, showing varied response amplitudes and durations at different depths. Note that the depth in this panel is measured from the surface of the fly brain. The gray bar indicates when a puff of ethyl acetate was delivered to the fly antenna. (c) Averaged fractional PA amplitude response and the concurrently recorded fluorescence intensity response to odor stimulation with the cuticle removed. (d) Epi-fluorescence image of a GCaMP5G-expressing fly brain with the cuticle intact (i.e., not surgically removed). The lateral location of the M-mode PA recording is marked by the dashed circle. (e) Fractional PA amplitude changes from representative neuron layers in the fly brain with its cuticle intact. Note that the lack of response in the cuticle layer (CL) is shown here as a control. Depth in this panel is measured from the cuticle layer. The gray bar indicates the duration of the ethyl acetate delivery to the fly antennae. (f) Averaged fractional PA amplitude response from the fly brain with intact cuticle and the concurrently recorded fluorescence intensity response to odor stimulation. Although the fractional changes in PA amplitude and fluorescence intensity are comparable in magnitude, depth-resolved measurements of neural activity were made only by the PA system.

We monitored neural activities in the fly brain evoked by a sensory stimulus. We administered a 5 sec. long puff of ethyl acetate to the fruit fly antenna while monitoring the changes in the GCaMP signals in the glomerular regions of the antennal lobe (a region where olfactory sensory neuron axon terminals converge and synapse with the downstream neural populations). M-mode recording (i.e., repeated 1D depth-resolved PA imaging at the same lateral location) was performed in the fruit fly antennal lobe. Depth-resolved PA signals from different layers in the brain (~200 μm thick) were acquired at a 1D imaging rate of 1 kHz (Figure 6.3(b)). The increase in GCaMP's optical absorption coefficient led to the same fractional PA and fluorescent signal changes. In response to the odor stimulation, we observed an ~23% PA signal increase on average (Figure 6.3(c)), which indicated elevated neural activities. The strongest fractional PA signal change (~34%) was observed at 90 μm beneath the brain surface. We observed different response durations at different depths from the PAM channel, which clearly indicates the heterogeneity in the dynamics of odor-evoked responses from sensory neuron axonal terminals. Ethyl acetate strongly activates different types of sensory neurons and in particular those housed in the large basiconic sensilla. The axonal terminals of these sensory neurons are known arborize in different glomeruli at different depths in the fly antennal lobe[191,192] The PA response time course averaged over all depths correlates well with the fluorescence response (Figure 6.3(c)) simultaneously recorded at the same lateral location. This correlation indicates that the same neuronal events were being imaged by both PAM and EFM channels. More importantly, depth-resolved signals were only obtained using PAM, clearly illustrating the benefit of the proposed approach. We also recorded similar PA and fluorescence responses in the lateral horn region of the fly brain (Figure 6.4).

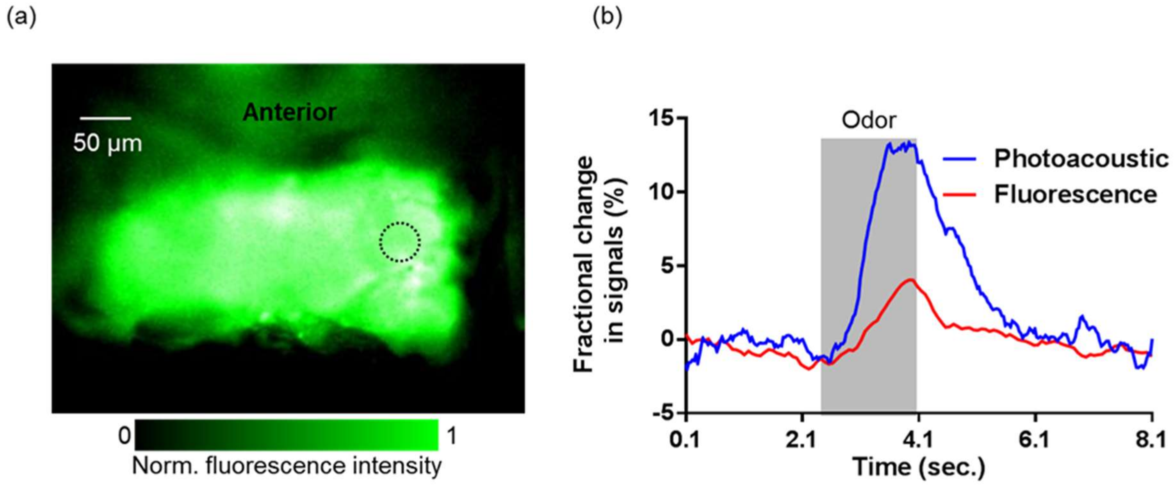

Figure 6.4 Fluorescence and PA recording of neural activities in the lateral horn region of a fly brain. (a) Epi-fluorescence image of a GCaMP5G-expressing fly brain with cuticle removed. The location of the M-mode PA recording is marked by the dashed circle. (b) Averaged fractional M-mode PA signal change and concurrent fluorescence response to odor stimulations in the fly brain, with cuticle removed.

Next, taking advantage of the depth-resolving and scattering-tolerant capabilities of PAM, we sought to obtain whether such depth-resolved signals can be obtained from flies with intact cuticles (i.e., without any surgical preparations) (Figure 6.3(d)). Although light was attenuated by the cuticle and connective tissue, PAM still detected signals from all neuron layers in the brain. We recorded concurrent M-mode PA and fluorescence signals upon odor stimulation . Similar to the results acquired with the cuticle removed, different PA responses were recorded from different neuronal layers (Figure 6.3(e)). The PA signals from the surface layer of the cuticle, served as a built-in control and indeed failed to show any changes during odor stimulation as expected. Note that even with the intact cuticle, the fractional signal change was observed reliably (Figure 6.3(e)-(f), Figure 6.5). Again, the PA results were confirmed by the concurrent fluorescence recording (Figure 6.3(f)).

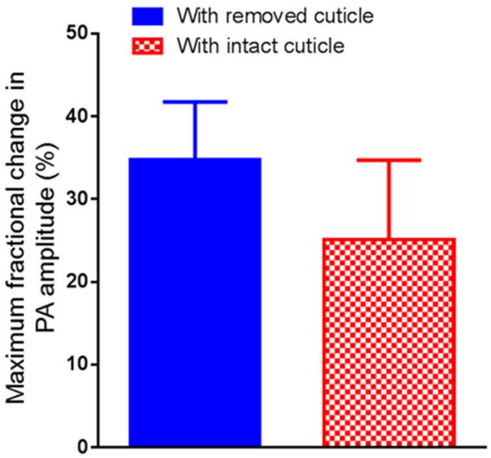

Figure 6.5 Odor-evoked maximum fractional change in PA amplitude in the fly brain, with removed and intact cuticle, respectively. Error bars, standard deviations. n = 3.

As mentioned earlier, PAM can render a 3D calcium image with only a 2D scan. To illustrate this, we imaged a volume of 100 μm (*x* axis) by 40 μm (*y* axis) by 270 μm (*z* axis) in the antennal lobe region of the fly brain (with the cuticle removed), at a volumetric imaging rate of 1 Hz (Figure 6.6, Figure 6.7). Both anatomical structures and the functional activity of neurons expressing GCaMP5G in the putative glomerular layers of the fly antennal lobe were clearly imaged (Figure 6.6(a)). The diversity of odor-evoked responses at different depths were still captured (Figure

6.6(b)-(c)). In sum, these results convincingly show that PAM can monitor depth-resolved calcium signals from neurons with high spatial and temporal resolutions.

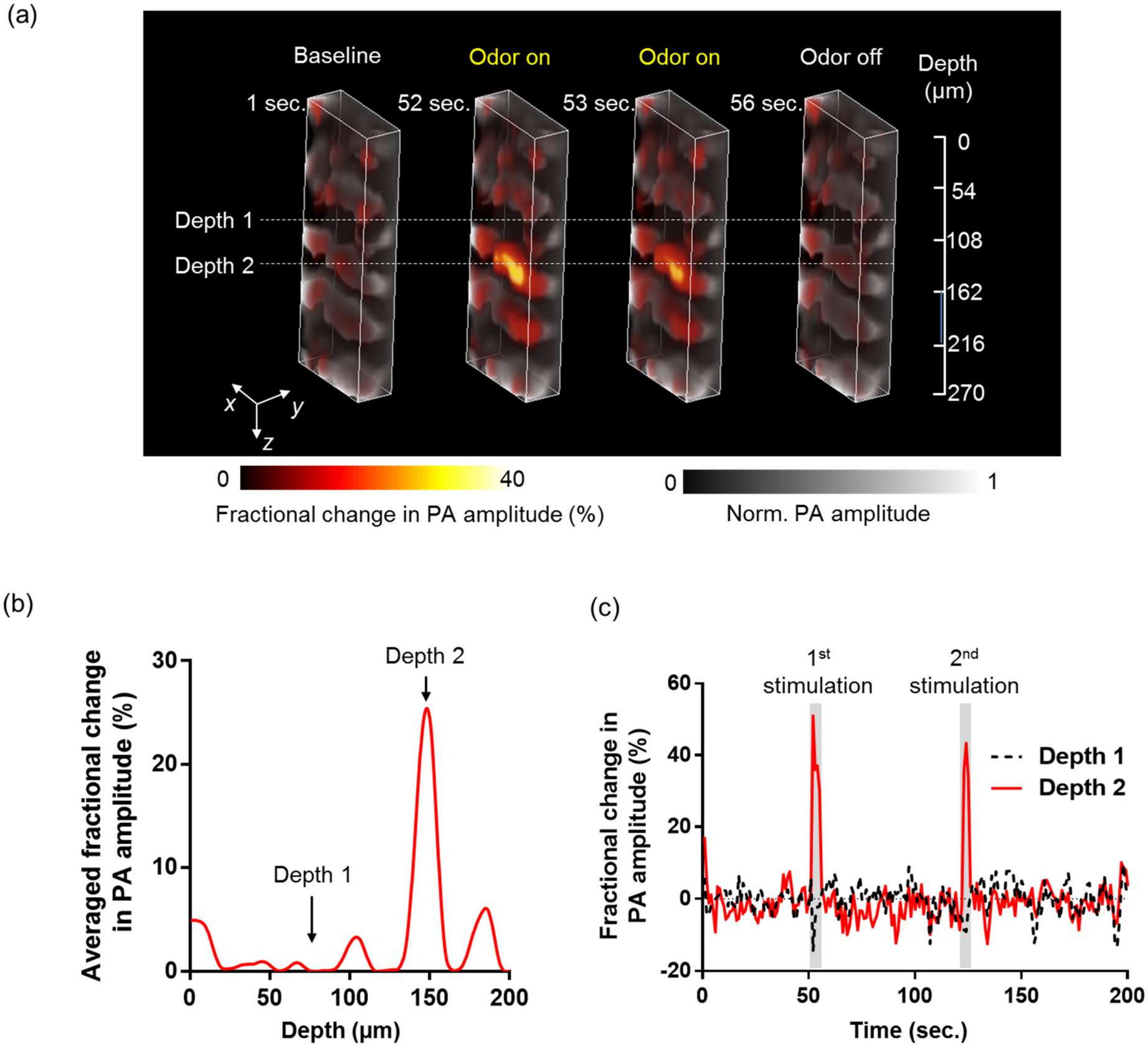

Figure 6.6 Volumetric PAM of odor-evoked neural activities in the glomerular antennal lobe region of a fly brain. (a) Volumetric images of the fly brain with the cuticle removed, before, during, and after the odor stimulation. The fractional changes in PA amplitude (shown in color) are overlaid on the structural image (shown in gray). (b) Depth-wise averaged fractional changes in PA amplitude during odor stimulations. The changes are averaged over the two stimulations. (c) Time courses of averaged fractional PA amplitude changes from two representative layers (labeled in (a)) of neurons. The gray bars indicate two successive puffs of ethyl acetate.

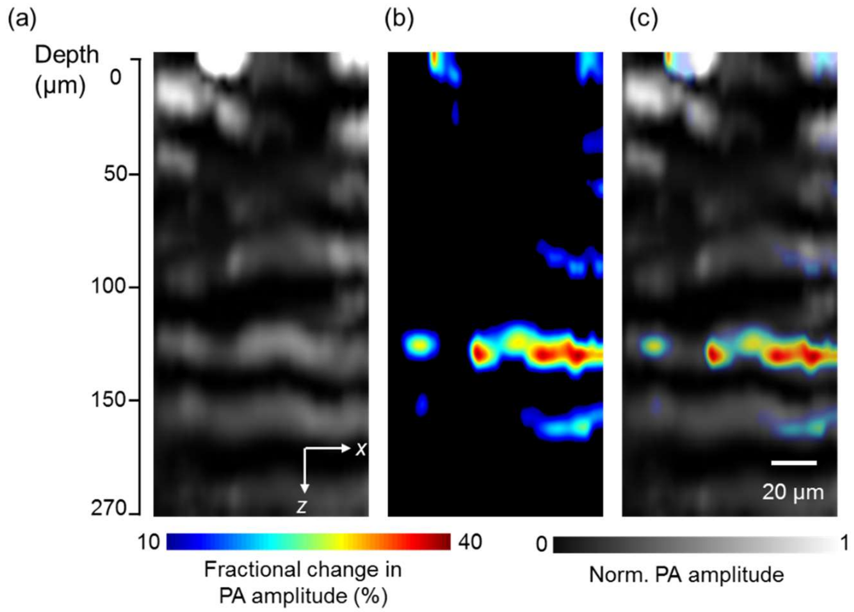

Figure 6.7 Cross-sectional view of PAM of odor-evoked neural activity in the antennal lobe region of a fly brain with the cuticle removed. (a) Cross-sectional structural image of the antennal lobe region of a fly brain with the cuticle removed. (b) Fractional change in PA amplitude in the region shown in (a), during odor stimulation. (c) Fractional change in PA amplitude overlaid with the cross-sectional structural image of the fly brain.

6.3.2 PACT of Live GCaMP6f-expressing Mouse Brain Slices

Taking advantage of PACT's deep imaging capability, we used our recently developed high-speed PACT system to image neural activity at depths greater than the optical diffusion limit of ~1 mm (Figure 6.8(a)). With wide-field illumination and parallel acoustic detection, the newly developed PACT system features high spatiotemporal resolution, deep penetration, and full-view fidelity. PACT acquires a 2D cross-sectional image with a 100-μm resolution at a 10-Hz frame rate. Further, only a single laser pulse is used to generate each 2D image, and thereby greatly reducing unnecessary light exposure and resultant photobleaching. In the absence of hemodynamically induced PA signal changes in the brain slice, GCaMP6f is the chromophore that can generate dynamic PA signals upon 488 nm laser excitation during neural activities.

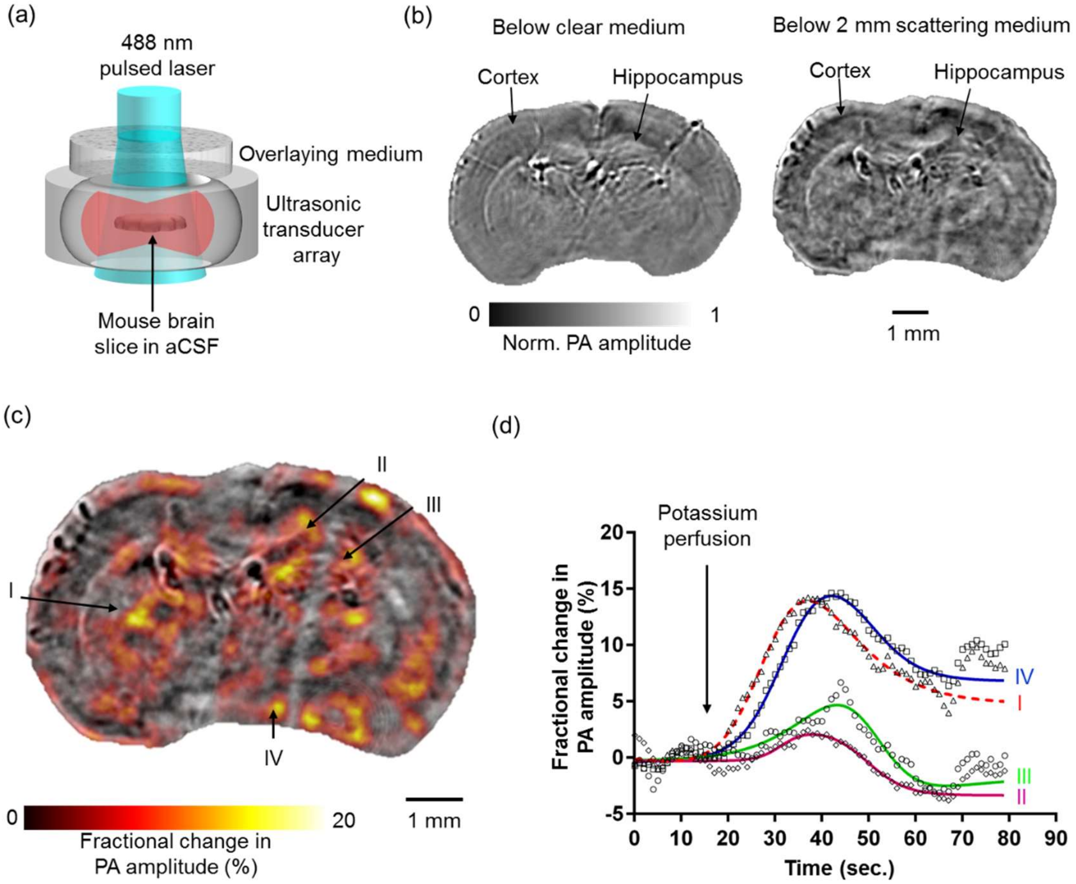

Figure 6.8 PACT monitoring of *in vitro* neural activities in GCaMP6f mouse brain slices. (a) Schematic of the high-speed PACT system, with wide-field illumination and parallel acoustic detection. The GCaMP6f-expressing brain slice was immersed in regular aCSF solution in the imaging chamber. (b) PACT images of the GCaMP6f-expressing brain slice in a clear medium (left) and through a 2-mm-thick scattering Intralipid solution (right, reduced optical scattering coefficient 10 cm−1). (c) PACT of the neural activity in a GCaMP6f-expressing mouse brain slice in response to high-potassium perfusion. The fractional PA amplitude change (shown in color) is superimposed on the baseline image (shown in gray). (d) Time courses of fractional PA amplitude changes from four representative regions (I, II, III and IV) as indicated in (c). The solid lines are fittings using a bell-shaped dose-response model.

We imaged neural activity in acute coronal slices (300 μm thick) of a GCaMP6f-expressing mouse brain. The brain slice was mounted in the PACT imaging chamber, which was filled with regular artificial cerebro-spinal fluid (aCSF), and imaged either without any scattering medium or through a 2-mm-thick tissue-simulating scattering medium (Figure 6.8(b)). In PACT images acquired without an overlying scattering medium, major brain structures expressing GCaMP6f, such as the cortex and hippocampus, were clearly resolved. Notably, even when the brain slice was covered with a 2-mm-thick scattering medium (1% Intralipid in deionized water, with a reduced scattering coefficient ~10 cm^{-1}), GCaMP6f-rich brain structures were still observable (Figure 6.8(b)).

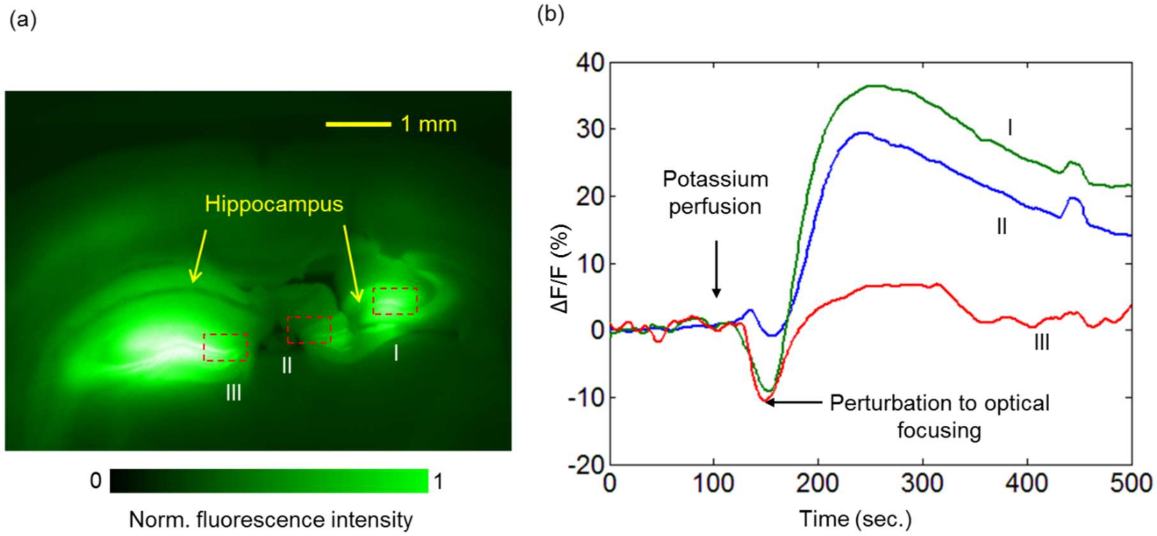

Figure 6.9 Wide-field fluorescence microscopy of a GCaMP6f-expressing mouse brain slice. (a) Fluorescence image of a GCaMP6f-expressing mouse brain slice, showing that the hippocampus area had a high expression level of GCaMP6f. (b) Averaged fractional fluorescence intensity changes after high-potassium perfusion, from the three regions marked in (a). The short-period signal decrease right after the perfusion started was due to optical defocusing caused by the perfusion perturbation.

To stimulate the neurons in the brain slice, we performed high-concentration potassium perfusion in the PACT imaging chamber (Methods). The elevated extracellular potassium depolarized neurons in the brain slice and induced action potentials. Upon high-potassium perfusion, increased PA signals were recorded from multiple areas within the brain slice (Figure 6.8(c)). The fractional PA amplitude changes shown in Figure 6.8(d) were averaged over representative regions of interest. The fractional PA amplitude increased by up to ~15% during the potassium perfusion. After the potassium perfusion, the intracellular calcium concentration gradually returned to the baseline level through diffusion and sodium-calcium exchanges, resulting in decreased PA amplitudes in the originally responding areas. In another experiment with a mouse brain slice covered with 1.5-mm-thick mouse brain tissue, we also observed a similar PA signal increase upon high-potassium perfusion. The PA response was independently validated by monitoring the fluorescence response of a brain slice in regular aCSF, measured with a commercial wide-field fluorescence microscope. The same sample preparation and stimulation procedures were used (Methods). In sum, our results confirm that PACT is a unique and effective calcium imaging technique with an image depth beyond the optical diffusion limit.

6.4 Conclusions and Discussion

We have demonstrated, for the first time, that multiscale PAT can be used for imaging neuronal calcium signals, with high spatiotemporal resolution and deep penetration. With fast dynamics, high photostability, and a large fractional absorption response, GCaMP or its variants offers an ideal optical contrast for PAT as PA signal is exquisitely sensitive to optical absorption. With the depth-resolved imaging capability, we showed that PAM can perform fast 3D calcium imaging in fruit flies expressing genetically encoded calcium indicators. Notably, using PAM we were able to monitor depth-resolved odor-evoked neural activities from the fly brain, without the need for invasive surgery, which could compromise experimental reproducibility [193]. While we focused on the feasibility of PAM for neural imaging here, the imaging rate can be readily increased by utilizing a higher pulse-repetition-rate laser and an optimized scanning mechanism[5].

Optical scattering of light severely limits high-resolution optical imaging techniques to superficial tissue layers. Our results clearly demonstrate that by utilizing diffused photons, PACT can image neural responses beyond the optical diffusion limit. Prior work has shown that PACT can provide a penetration depth of 8 mm in a rat brain[168]. Although, the imaging depth of PACT demonstrated in this study was largely limited by the relatively short absorption wavelength of GCaMP, it can be further improved by using calcium indicators that absorb strongly at longer wavelengths[180,194,195], especially in the near-infrared wavelength region (700–1100 nm). The combination of near-infrared calcium indicators and PACT can potentially enable small-animal whole-brain neural imaging.

So far, a variety of imaging modalities have been explored for brain studies, especially two-photon microscopy and functional magnetic resonance imaging (fMRI). At the microscopic scale, two-photon microscopy allows detailed and direct examination of neural activities in small animal models [196]. At the macroscopic scale, fMRI has been extensively used to map human or large-animal brain activities, allowing indirect coarse-grained localization of cognitive functions with hemodynamic signals. However, correlating the two imaging scales still remains a major challenge due to the different signal-contrast sources of these two modalities. Therefore, there is a gap in our understanding between the macroscopic activity patterns in humans or large animals and the microscopic activity details in small-animal models. PAT has been scaled up for multiple-centimeter penetration and can provide multiscale imaging for not only small animals but also potentially large animals (at least with open skulls)[59,158,197] . Multi-wavelength PAT can be implemented to simultaneously record and unmix hemodynamic and calcium signals, enabling studies of neurovascular coupling. Therefore, PAT is uniquely positioned to bridge this contrast gap across the length scales, facilitating correlative neuroscience studies in various animal models of brain diseases such as Alzheimer's disease and stroke[148].

In conclusion, we have shown that PAT holds great promise for neuronal calcium imaging in the brains of transgenic invertebrate and vertebrate models expressing GCaMP indicators. With PAM, we demonstrate *in vivo* high-resolution depth-resolved neural imaging without depth scanning, which enables 3D imaging of neural activities at high temporal resolution. With PACT, we demonstrate neural activity imaging with GCaMP beyond the optical diffusion limit. The combination of advanced PAT technologies and genetically encoded neural activity indicators optimized for PA imaging offers the neuroscience community a new methodology for studying neural networks *in vivo*.

Chapter 7 Summary and Outlook

In this dissertation, we have applied novel PA contrasts for homogenous flow measurements, label-free macrophage imaging, automated 3D cell nuclei imaging of whole organs, targeted imaging/therapy of angiogenesis, and neural imaging of calcium/voltage signals in brains through thick scattering medium.

In Chapter 2, with structured illumination, we demonstrated flow speed measurement in a homogenous medium based on the photoacoustic Doppler frequency shift. Next, by optically encoding a thermal pattern in the flowing medium, we successfully measured the flow speed in a blood vessel in mouse ear vasculature *in vivo*.

In Chapter 3, we first demonstrated the use of PAM for spectral characterization of macrophages. Then, with the assistance of a microtome, we demonstrated automated PAM of whole organs with subcellular resolution.

In Chapter 4, we applied novel near-infrared copper nanoparticles for targeted imaging and therapy of angiogenesis in mice *in vivo* for the first time.

In Chapter 5, we demonstrated the first use of DPA and characterized it for photoacoustic neural imaging. We applied the dye to live cell imaging, and to *in vivo* mouse brain neural activity imaging during epilepsy and cortical electrical stimulation.

In Chapter 6, on the microscopic scale, we unambiguously demonstrated PA imaging of a genetically encoded calcium indicator in a fly brain without interference signals from hemoglobin.

On the macroscopic scale, we demonstrated wide-field neural activity imaging of a live GCaMP brain slice.

The exploration of novel contrasts of PAT is still going on. For endogenous contrast imaging, we expect to include more endogenous contrasts, such as lipid in the near infrared range for label-free mouse brain imaging, and specific biological molecules at their “fingerprint” wavelengths in the mid-infrared range. By extending the wavelength palette from UV to mid-infrared, we expect to provide a more complete map of biomolecules without labeling and with minimal processing.

With the development of more long-wavelength exogenous probes (dyes, proteins and nanoparticles) for PA, we seek to push the penetration depth to above 1 mm in the mouse brain for neural activity imaging *in vivo*, and to unambiguously un-mix dye/protein signals from hemodynamic signals.

Combined with advanced contrasts, rapidly developing PAT systems with higher frame rates and improved resolution, can potentially enable deep, fast, and high-resolution imaging of diverse biological and physiological processes for basic neuroscience studies and preclinical/clinical trials in cancer diagnostics/treatment and immunotherapy.

References

1. Lihong V Wang and Hsin-i Wu, *Biomedical optics: principles and imaging*. (John Wiley & Sons, 2012).
2. J. Yao and L. V. Wang, *Contrast Media Mol Imaging* **6** (5), 332 (2011).
3. Da-Kang Yao, Konstantin Maslov, Kirk K Shung et al., *Opt Lett* **35**, 4139 (2010).
4. Lihong V Wang, Chi Zhang, Shrike Zhang et al., *J Biomed Opt* **18**, 020504 (2013).
5. J. J. Yao, L. D. Wang, J. M. Yang et al., *Nature Methods* **12** (5), 407 (2015).
6. Hao F. Zhang, Konstantin Maslov, George Stoica et al., *Nat Biotech* **24** (7), 848 (2006).
7. T. P. Matthews, C. Zhang, D. K. Yao et al., *J Biomed Opt* **19** (1), 16004 (2014).
8. J. Weber, P. C. Beard, and S. E. Bohndiek, *Nat Methods* **13** (8), 639 (2016).
9. R. Zhang, J. Yao, K. I. Maslov et al., *Appl Phys Lett* **103** (9), 94101 (2013).
10. R. Zhang, L. Wang, J. Yao et al., *Opt Lett* **39** (13), 3814 (2014).
11. Wilmer W. Nichols and Donald A. McDonald, *McDonald's blood flow in arteries : theoretic, experimental, and clinical principles*, 6th ed. (Hodder Arnold, London, 2011).
12. K Kirk Shung, *Diagnostic ultrasound: Imaging and blood flow measurements*. (CRC press, 2015).
13. Richard Goldstein, *Fluid mechanics measurements*. (CRC Press, 1996).
14. DN White, *Ultrasound in medicine & biology* **8** (6), 583 (1982).
15. David H Evans and W Norman McDicken, *Doppler ultrasound: physics, instrumentation and signal processing*. (John Wiley & Sons, 2000).
16. Zhongping Chen, Yonghua Zhao, Shyam M Srinivas et al., *Ieee Journal of Selected Topics in Quantum Electronics* **5** (4), 1134 (1999).

17. P Ake Oberg, *Critical reviews in biomedical engineering* **18** (2), 125 (1989).

18. Adi Sheinfeld, Sharon Gilead, and Avishay Eyal, *J Biomed Opt* **15** (6), 066010 (2010).

19. Lihong V Wang and Song Hu, *Science* **335** (6075), 1458 (2012).

20. Junjie Yao, Konstantin I Maslov, Yu Zhang et al., *J Biomed Opt* **16** (7), 076003 (2011).

21. Junjie Yao and Lihong V Wang, *J Biomed Opt* **15** (2), 021304 (2010).

22. Adi Sheinfeld, Sharon Gilead, and Avishay Eyal, *Opt Express* **18** (5), 4212 (2010).

23. Hui Fang, Konstantin Maslov, and Lihong V Wang, *Applied Physics Letters* **91** (26), 264103 (2007).

24. Hui Fang, Konstantin Maslov, and Lihong V Wang, *Phys Rev Lett* **99** (18), 184501 (2007).

25. Joanna Brunker and Paul Beard, *The Journal of the Acoustical Society of America* **132** (3), 1780 (2012).

26. L. D. Wang, J. Xia, J. J. Yao et al., *Phys Rev Lett* **111** (20) (2013).

27. L. D. Wang, G. Li, J. Xia et al., *Optica* **2** (4), 307 (2015).

28. J. J. Yao, K. I. Maslov, and L. H. V. Wang, *Technol Cancer Res T* **11** (4), 301 (2012).

29. J. Brunker and P. Beard, *J Acoust Soc Am* **132** (3), 1780 (2012).

30. J. J. Yao, K. I. Maslov, Y. F. Shi et al., *Opt Lett* **35** (9), 1419 (2010).

31. P. Beard, *Interface Focus* **1** (4), 602 (2011).

32. Adi Sheinfeld and Avishay Eyal, presented at the SPIE BiOS, 2013 (unpublished).

33. Lidai Wang, Guo Li, Jun Xia et al., *Optica* **2** (4), 307 (2015).

34. S. Hu, K. Maslov, and L. V. Wang, *Opt Lett* **36** (7), 1134 (2011).

35. Chenghung Yeh, Brian Soetikno, Song Hu et al., *Journal of biophotonics* **8** (4), 303 (2015).

36. J. J. Yao, C. H. Huang, L. D. Wang et al., *J Biomed Opt* **17** (8) (2012).

37. David M Mosser and Justin P Edwards, *Nature reviews immunology* **8** (12), 958 (2008).

38. Scott Prahl, Available at http://omlc.org/spectra/hemoglobin/summary.html.

39. Eli Gibson, Mena Gaed, José A Gómez et al., *J Pathol Inform* **4:31** (2013).

40. Tao Ju, Joe Warren, James Carson et al., *J Neurosci Meth* **156**, 84 (2006).

41. Nicholas Roberts, Derek Magee, Yi Song et al., *Am J Pathol* **180**, 1835 (2012).

42. Yi Song, Darren Treanor, Andrew J Bulpitt et al., *J Pathol Inform* **4:7** (2013).

43. Ching-wei Wang, Eric Budiman Gosno, and Yen-sheng Li, *Sci Rep-Uk* **5**, 15051 (2015).

44. Yiwen Xu, J Geoffrey Pickering, Zengxuan Nong et al., *Plos One* **10**, e0126817 (2015).

45. D. K. Yao, R. Chen, K. Maslov et al., *J Biomed Opt* **17** (5), 056004 (2012).

46. R. Zhang, D. Pan, X. Cai et al., *Theranostics* **5** (2), 124 (2015).

47. Peter C Brooks, RA Clark, and David A Cheresh, *Science* **264** (5158), 569 (1994).

48. Patrick M Winter, Anne M Neubauer, Shelton D Caruthers et al., *Arterioscler Thromb Vasc Biol* **26** (9), 2103 (2006).

49. Patrick M Winter, Anne H Schmieder, Shelton D Caruthers et al., *Faseb J* **22** (8), 2758 (2008).

50. Oliver Schnell, Bjarne Krebs, Janette Carlsen et al., *Neuro Oncol* **11** (6), 861 (2009).

51. A. J. Beer, R. Haubner, M. Goebel et al., *J Nucl Med* **46** (8), 1333 (2005).

52. L. M. Kenny, R. C. Coombes, I. Oulie et al., *J Nucl Med* **49** (6), 879 (2008).

53. C. T. Pham, L. M. Mitchell, J. L. Huang et al., *The Journal of biological chemistry* **286** (1), 123 (2011).

54. Nick G Costouros, Felix E Diehn, and Steven K Libutti, *J Cell Biochem* **87** (S39), 72 (2002).

55. M. Neeman, *Journal of cellular biochemistry. Supplement* **39**, 11 (2002).

56. Justin D Pearlman, Roger J Laham, Mark Post et al., *Curr Pharm Des* **8** (16), 1467 (2002).

57. Ralph Weissleder, *Nat Rev Cancer* **2** (1), 11 (2002).

58. Ralph Weissleder and Vasilis Ntziachristos, *Nat Med* **9** (1), 123 (2003).

59. L. H. V. Wang and S. Hu, *Science* **335** (6075), 1458 (2012).

60. D. Pan, M. Pramanik, A. Senpan et al., *Faseb J* **25** (3), 875 (2011).

61. Adam De La Zerda, Cristina Zavaleta, Shay Keren et al., *Nat Nanotechnol* **3** (9), 557 (2008).

62. Liangzhong Xiang, Yi Yuan, Da Xing et al., *J Biomed Opt* **14** (2), 021008 (2009).

63. Dipanjan Pan, Manojit Pramanik, Angana Senpan et al., *Angew Chem Int Ed* **48** (23), 4170 (2009).

64. Y. Li, W. Lu, Q. Huang et al., *Nanomedicine (London, England)* **5** (8), 1161 (2010).

65. Dipanjan Pan, Nibedita Sanyal, Anne H Schmieder et al., *Nanomedicine* **7** (10), 1507 (2012).

66. David F Meoli, Mehran M Sadeghi, Svetlana Krassilnikova et al., *J Clin Invest* **113** (12), 1684 (2004).

67. K. H. Song and L. V. Wang, *J Biomed Opt* **12** (6), 060503 (2007).

68. Dipanjan Pan, Manojit Pramanik, Samuel A Wickline et al., *Contrast Media Mol Imaging* **6** (5), 378 (2011).

69. Dipanjan Pan, Manojit Pramanik, Angana Senpan et al., *Biomaterials* **31** (14), 4088 (2010).

70. Katsuichi Sudoi, Tsuneo Kanamarui, Harold Brem et al., *Nature* **348**, 6 (1990).

71. Shenping Liu, Joanne Widom, Christopher W Kemp et al., *Science* **282** (5392), 1324 (1998).

72. Hui-fang Zhou, Huimin Yan, Angana Senpan et al., *Biomaterials* **33** (33), 8632 (2012).

73. S. Hu and L. V. Wang, *J Biomed Opt* **15** (1), 011101 (2010).

74. Li Meng-Lin, Oh Jung-Taek, X. Xie et al., *Proceedings of the IEEE* **96** (3), 481 (2008).

75. Leonie Rouleau, Romain Berti, Vanessa WK Ng et al., *Contrast Media Mol Imaging* **8** (1), 27 (2013).

76. Chulhong Kim, Eun Chul Cho, Jingyi Chen et al., *ACS nano* **4** (8), 4559 (2010).

77. Pai-Chi Li, Churng-Ren Chris Wang, Dar-Bin Shieh et al., *Opt Express* **16** (23), 18605 (2008).

78. A Agarwal, SW Huang, M O'Donnell et al., *J Appl Phys* **102** (6), 064701 (2007).

79. Adam de la Zerda, Zhuang Liu, Sunil Bodapati et al., *Nano letters* **10** (6), 2168 (2010).

80. Dipanjan Pan, Shelton D Caruthers, Angana Senpan et al., *J Am Chem Soc* **133** (24), 9168 (2011).

81. A. H. Schmieder, P. M. Winter, S. D. Caruthers et al., *Magnetic resonance in medicine : official journal of the Society of Magnetic Resonance in Medicine / Society of Magnetic Resonance in Medicine* **53** (3), 621 (2005).

82. P. M. Winter, S. D. Caruthers, A. Kassner et al., *Cancer Res* **63** (18), 5838 (2003).

83. R. K. Jain, *Nat Med* **7** (9), 987 (2001).

84. R. K. Jain, *Scientific American* **298** (1), 56 (2008).

85. R. K. Jain, A. V. Finn, F. D. Kolodgie et al., *Nature clinical practice. Cardiovascular medicine* **4** (9), 491 (2007).

86. J. Lee, T. Ku, H. Yu et al., *Cancer letters* **318** (2), 221 (2012).

87. F. A. Eskens and J. Verweij, *European journal of cancer (Oxford, England : 1990)* **42** (18), 3127 (2006).

88. R. Offodile, T. Walton, M. Lee et al., *Tumori* **85** (1), 51 (1999).

89. R. S. Herbst, T. L. Madden, H. T. Tran et al., *Journal of clinical oncology : official journal of the American Society of Clinical Oncology* **20** (22), 4440 (2002).

90. C. J. Logothetis, K. K. Wu, L. D. Finn et al., *Clinical cancer research : an official journal of the American Association for Cancer Research* **7** (5), 1198 (2001).

91. P. M. Winter, S. D. Caruthers, H. Zhang et al., *JACC. Cardiovascular imaging* **1** (5), 624 (2008).

92. P. M. Winter, A. H. Schmieder, S. D. Caruthers et al., *Faseb J* **22** (8), 2758 (2008).

93. N. R. Soman, S. L. Baldwin, G. Hu et al., *J Clin Invest* **119** (9), 2830 (2009).

94. K. C. Partlow, G. M. Lanza, and S. A. Wickline, *Biomaterials* **29** (23), 3367 (2008).

95. D. Pan, A. H. Schmieder, K. Wang et al., *Theranostics* **4** (6), 565 (2014).
96. Michelle Grayson, *Nature* **466** (7310), S1 (2010).
97. Marios Politis, *Nat Rev Neurol* **10** (12), 708 (2014).
98. R. P. Munhoz, A. Moro, L. Silveira-Moriyama et al., *Arquivos de neuro-psiquiatria* **73** (5), 454 (2015).
99. Martin Citron, *Nat Rev Drug Discov* **9** (5), 387 (2010).
100. Yadong Huang and Lennart Mucke, *Cell* **148** (6), 1204 (2012).
101. G. Buzsaki, *Nature Neuroscience* **7** (5), 446 (2004).
102. V. Marx, *Nature Methods* **11** (11), 1099 (2014).
103. B. J. Baker, E. K. Kosmidis, D. Vucinic et al., *Cellular and molecular neurobiology* **25** (2), 245 (2005).
104. R. Homma, B. J. Baker, L. Jin et al., *Philosophical transactions of the Royal Society of London. Series B, Biological sciences* **364** (1529), 2453 (2009).
105. A. Grinvald, R. D. Frostig, E. Lieke et al., *Physiological reviews* **68** (4), 1285 (1988).
106. Robert D. O'Neill, *Analyst* **119** (5), 767 (1994).
107. Rajendra D. Badgaiyan, *Current Medical Imaging Reviews* **7** (2), 98 (2011).
108. R. Liang, G. J. Broussard, and L. Tian, *ACS chemical neuroscience* **6** (1), 84 (2015).
109. Nicholas G. Horton, Ke Wang, Demirhan Kobat et al., *Nat Photon* **7** (3), 205 (2013).
110. E. Zhang, J. Laufer, and P. Beard, *Appl Opt* **47** (4), 561 (2008).
111. L. V. Wang, *Nat Photonics* **3** (9), 503 (2009).
112. J. Laufer, E. Zhang, G. Raivich et al., *Appl Opt* **48** (10), D299 (2009).
113. A. L. Hodgkin and A. F. Huxley, *The Journal of physiology* **116** (4), 449 (1952).
114. Richard Fairless, Andreas Beck, Mykola Kravchenko et al., *Plos One* **8** (3), e58260 (2013).

115. O. S. Andersen, S. Feldberg, H. Nakadomari et al., *Biophysical Journal* **21** (1), 35.

116. S. W. Feldberg and A. B. Delgado, *Biophys J* **21** (1), 71 (1978).

117. J. M. Fernandez, R. E. Taylor, and F. Bezanilla, *The Journal of general physiology* **82** (3), 331 (1983).

118. Baron Chanda, Rikard Blunck, Leonardo C. Faria et al., *Nature Neuroscience* **8** (11), 1619 (2005).

119. M. DiFranco, J. Capote, M. Quinonez et al., *The Journal of general physiology* **130** (6), 581 (2007).

120. L. Sjulson and G. Miesenbock, *Physiology* **22**, 47 (2007).

121. J. Bradley, R. Luo, T. S. Otis et al., *J Neurosci* **29** (29), 9197 (2009).

122. A. E. Fink, K. J. Bender, L. O. Trussell et al., *Plos One* **7** (8), e41434 (2012).

123. N. Ghitani, P. O. Bayguinov, Y. Ma et al., *Journal of neurophysiology* **113** (4), 1249 (2015).

124. M. H. Histed, V. Bonin, and R. C. Reid, *Neuron* **63** (4), 508 (2009).

125. Svenja Borchers, Marc Himmelbach, Nikos Logothetis et al., *Nat Rev Neurosci* **13** (1), 63 (2012).

126. D. T. Brocker and W. M. Grill, *Handbook of clinical neurology* **116**, 3 (2013).

127. P. A. Rutecki, F. J. Lebeda, and D. Johnston, *Journal of neurophysiology* **57** (6), 1911 (1987).

128. T. J. Chesnut and J. W. Swann, *Epilepsy research* **2** (3), 187 (1988).

129. S. N. Hoffman and D. A. Prince, *Brain research. Developmental brain research* **85** (1), 64 (1995).

130. F. Pena and R. Tapia, *Neuroscience* **101** (3), 547 (2000).

131. G. F. Tian, H. Azmi, T. Takano et al., *Nat Med* **11** (9), 973 (2005).

132. P. Federico, S. G. Borg, A. G. Salkauskus et al., *Neuroscience* **58** (3), 461 (1994).

133. F. Weissinger, K. Buchheim, H. Siegmund et al., *Neurobiology of disease* **7** (4), 286 (2000).

134. T. H. Schwartz and T. Bonhoeffer, *Nat Med* **7** (9), 1063 (2001).

135. M. M. Haglund and D. W. Hochman, *Epilepsia* **45 Suppl 4**, 43 (2004).

136. Sonya Bahar, Minah Suh, Ashesh Mehta et al., in *Bioimaging in Neurodegeneration*, edited by PatriciaA Broderick, DavidN Rahni, and EdwinH Kolodny (Humana Press, 2005), pp. 149.

137. M. M. Eberle, C. L. Reynolds, J. I. Szu et al., *Biomedical optics express* **3** (11), 2700 (2012).

138. V. Tsytsarev, B. Rao, K. I. Maslov et al., *J Neurosci Methods* **216** (2), 142 (2013).

139. Edgar Guevara, Philippe Pouliot, Dang Khoa Nguyen et al., *J Biomed Opt* **18** (7), 076021 (2013).

140. A. G. Daniel, P. Laffont, M. Zhao et al., *Epilepsy & behavior : E&B* **49**, 61 (2015).

141. M. M. Eberle, M. S. Hsu, C. L. Rodriguez et al., *Biomedical optics express* **6** (5), 1812 (2015).

142. L. L. Looger and O. Griesbeck, *Curr Opin Neurobiol* **22** (1), 18 (2012).

143. A. Devor, P. A. Bandettini, D. A. Boas et al., *Neuron* **80** (2), 270 (2013).

144. M. E. Raichle and M. A. Mintun, *Annu Rev Neurosci* **29**, 449 (2006).

145. T. A. Christensen, V. M. Pawlowski, H. Lei et al., *Nat Neurosci* **3** (9), 927 (2000).

146. R. Eckhorn and U. Thomas, *J Neurosci Meth* **49** (3), 175 (1993).

147. D. Saha, K. Leong, N. Katta et al., *Jove-J Vis Exp* (71) (2013).

148. E. M. C. Hillman, *J Biomed Opt* **12** (5), 051402 (2007).

149. B. Kuhn, W. Denk, and R. M. Bruno, *P Natl Acad Sci USA* **105** (21), 7588 (2008).

150. J. N. D. Kerr and W. Denk, *Nat Rev Neurosci* **9** (3), 195 (2008).

151. M. Scanziani and M. Hausser, *Nature* **461** (7266), 930 (2009).

152. R. Cossart, D. Aronov, and R. Yuste, *Nature* **423** (6937), 283 (2003).

153. R. Yuste and L. C. Katz, *Neuron* **6** (3), 333 (1991).

154. R. Yuste and W. Denk, *Nature* **375** (6533), 682 (1995).

155. W. Akemann, M. Sasaki, H. Mutoh et al., *Sci Rep-Uk* **3**, 2231 (2013).

156. Y. Y. Gong, C. Huang, J. Z. Li et al., *Science* **350** (6266), 1361 (2015).

157. D. G. Ouzounov, N. Horton, Wang Tianyu et al., presented at the 2014 Conference on Lasers and Electro-Optics (CLEO) - Laser Science to Photonic Applications, 2014 (unpublished).

158. L. V. Wang and J. Yao, *Nat Methods* **13** (8), 627 (2016).

159. B. A. Flusberg, A. Nimmerjahn, E. D. Cocker et al., *Nature Methods* **5** (11), 935 (2008).

160. K. K. Ghosh, L. D. Burns, E. D. Cocker et al., *Nature Methods* **8** (10), 871 (2011).

161. T. Berdyyeva, S. Otte, L. Aluisio et al., *Plos One* **9** (11), e112068 (2014).

162. L. A. Gunaydin, L. Grosenick, J. C. Finkelstein et al., *Cell* **157** (7), 1535 (2014).

163. D. Razansky, M. Distel, C. Vinegoni et al., *Nat Photonics* **3** (7), 412 (2009).

164. J. J. Yao, A. A. Kaberniuk, L. Li et al., *Nature Methods* **13** (1), 67 (2016).

165. C. Kim, C. Favazza, and L. H. V. Wang, *Chem Rev* **110** (5), 2756 (2010).

166. S. Hu, K. Maslov, V. Tsytsarev et al., *J Biomed Opt* **14** (4), 040503 (2009).

167. E. W. Stein, K. Maslov, and L. H. V. Wang, *Journal of Applied Physics* **105** (10), 102027 (2009).

168. X. D. Wang, Y. J. Pang, G. Ku et al., *Nat Biotechnol* **21** (7), 803 (2003).

169. M. Nasiriavanaki, J. Xia, H. L. Wan et al., *P Natl Acad Sci USA* **111** (1), 21 (2014).

170. J. J. Yao, J. Xia, K. I. Maslov et al., *Neuroimage* **64**, 257 (2013).

171. Z. L. Deng, Z. Wang, X. Q. Yang et al., *J Biomed Opt* **17** (8), 081415 (2012).

172. J. Jo and X. Yang, *J Biomed Opt* **16** (9), 090506 (2011).

173. L. D. Liao, M. L. Li, H. Y. Lai et al., *Neuroimage* **52** (2), 562 (2010).

174. Y. Y. Liu, X. Q. Yang, H. Gong et al., *J Biomed Opt* **18** (7), 076007 (2013).

175. M. C. Pilatou, E. Marani, F. F. M. de Mul et al., *Archives of Physiology and Biochemistry* **111** (4), 389 (2003).

176. V. Tsytsarev, B. Rao, K. I. Maslov et al., *J Neurosci Meth* **216** (2), 142 (2013).

177. L. D. Wang, K. Maslov, and L. H. V. Wang, *P Natl Acad Sci USA* **110** (15), 5759 (2013).

178. Q. Z. Zhang, Z. Liu, P. R. Carney et al., *Phys Med Biol* **53** (7), 1921 (2008).

179. P. O'Herron, P. Y. Chhatbar, M. Levy et al., *Nature* **534** (7607), 378 (2016).

180. J. Akerboom, N. Carreras Calderon, L. Tian et al., *Frontiers in molecular neuroscience* **6**, 2 (2013).

181. T. W. Chen, T. J. Wardill, Y. Sun et al., *Nature* **499** (7458), 295 (2013).

182. Lin Tian, S. Andrew Hires, Tianyi Mao et al., *Nat Meth* **6** (12), 875 (2009).

183. Jing W. Wang, Allan M. Wong, Jorge Flores et al., *Cell* **112** (2), 271 (2003).

184. Jörg Mütze, Vijay Iyer, John J Macklin et al., *Biophysical Journal* **102** (4), 934 (2012).

185. L. D. Wang, K. Maslov, W. X. Xing et al., *J Biomed Opt* **17** (10) (2012).

186. A. F. Silbering, R. Bell, C. G. Galizia et al., *Jove-J Vis Exp* (61) (2012).

187. M. Murthy and G. Turner, *Cold Spring Harb Protoc* **2013** (2), 134 (2013).

188. M. Xu and L. V. Wang, *Physical review. E, Statistical, nonlinear, and soft matter physics* **71** (1 Pt 2), 016706 (2005).

189. B. Cox, J. G. Laufer, S. R. Arridge et al., *J Biomed Opt* **17** (6), 061202 (2012).

190. J. Akerboom, T. W. Chen, T. J. Wardill et al., *The Journal of neuroscience : the official journal of the Society for Neuroscience* **32** (40), 13819 (2012).

191. A. Couto, M. Alenius, and B. J. Dickson, *Curr Biol* **15** (17), 1535 (2005).

192. A. A. Dobritsa, W. van der Goes van Naters, C. G. Warr et al., *Neuron* **37** (5), 827 (2003).

193. Supriyo Sinha, Liang Liang, Eric T. W. Ho et al., *Proceedings of the National Academy of Sciences* **110** (46), 18374 (2013).

194. M. Inoue, A. Takeuchi, S. Horigane et al., *Nature Methods* **12** (9), 893 (2015).

195. H. Dana, B. Mohar, Y. Sun et al., *Elife* **5** (2016).

196. F. Helmchen and W. Denk, *Nature Methods* **2** (12), 932 (2005).

197. L. M. Nie, X. Cai, K. Maslov et al., *J Biomed Opt* **17** (11) (2012).

Vita

Ruiying Zhang

EDUCATION

- **Ph.D. in Biomedical Engineering (Dec., 2016)**
  Optical Imaging Laboratory, Advisor: Lihong V. Wang
  Washington University in St. Louis, St. Louis, MO, USA

- **B.S. in Optical Information Science and Technology (Jun., 2011)**
  School of Electronic Information, Wuhan University, Wuhan, Hubei, China

Publications and work submitted (Square brackets denote equal contribution)

1. **R. Zhang**, B. Rao, H. Rong, L Li, M. Sun, J. Yao, R. Chen, Q. Zhou, S. Mennerick, R. Barani, L. V. Wang, "Multiscale Photoacoustic Tomography of Neural Activities with GCaMP Calcium Indicators", in revision.
2. **R. Zhang**, L. Wang, C. Zhang, L. V. Wang. "Label-free photoacoustic detection of macrophages". (In preparation)
3. **[**T. T. Wong**, R. Zhang],** C. Zhang, H. Hsu, K. Maslov, L. Wang, J. Shi, Y. Li, R. Chen, K.K, Shung, Q. Zhou, L. V. Wang, "Label-free, automated three-dimensional imaging of whole organs by microtomy-assisted photoacoustic microscopy". (In preparation)
4. T. T. Wong, **R. Zhang,** C. Zhang, P. Hai, M. A. Pleitez, R. L, Alf, N. V. Deborah, L. V. Wang, "Label-free instant histology of human breast cancer by photoacoustic microscopy", Science Advances, under review.
5. Y. He, L. Wang, J. Shi, J. Yao, **R. Zhang**, L. Li, J. Zou, L. V. Wang, "Real-time label-free imaging and deconstruction of circulating melanoma cells *in vivo*", Scientific Reports, accepted.
6. T. Imai, B. Muz, C. Yeh, J. Yao, **R. Zhang**, A. K. Azab, L.V. Wang, "Direct measurement of hypoxia in a xenograft multiple myeloma model by optical-resolution photoacoustic microscopy", Cancer Biology&Therapy, under review.
7. [L. Lin, J. Yao], L. Wang, **R. Zhang**, C. Chen, C. Huang, Y. Li, W. Chapman, J. Zou, L. V. Wang, "High-speed photoacoustic microscopy of mouse cortical microhemodynamics, Journal of Biophotonics, accepted.
8. [B. Rao, **R. Zhang]**, J. Shao, L. V. Wang, "In vivo photoacoustic imaging of brain voltage response signals beyond optical diffusion limit", Scientific reports, under review.
9. P. Hai, Y. Zhou, **R. Zhang**, J. Ma, Y. Li, J. Shao, L. V. Wang. "Label-free high-throughput detection and quantification of circulating melanoma tumor cell clusters by linear-array-based photoacoustic tomography". Journal of Biomedical Optics, in press.
10. L. Li, L. Zhu, C. Ma, J. Yao, J. Xia, L. Wang, K. Maslov, **R. Zhang**, Y. Li, W. Chen, J. Shi, L. V. Wang. "Single-impulse panoramic photoacoustic computed tomography of small-animal wholebody dynamics at spatiotemporal resolution", submitted.
11. J. Yao, A. A. Kaberniuk, L. Li, D. M. Shcherbakova, **R. Zhang**, L. Wang, G. Li, V. V. Verkhusha, L.V. Wang. "Multi-scale photoacoustic tomography using reversibly switchable bacterial phytochrome as a near-infrared photochromic probe". Nature Methods, 2015. (***Highlighted in ScienceDaily: Flipping the switch to see cancer cells better***)
12. M. Tang, Y. Zhou, **R. Zhang**, L. V. Wang. "Noninvasive photoacoustic microscopy of methemoglobin in vivo". Journal of Biomedical Optics, 20(3), 2015.
13. **R. Zhang**, D. Pan, X. Cai, X. Yang, A. Senpan, J. S. Allen, G., M. Lanza, L. V. Wang. "*αvβ3*-targeted

copper nanoparticles incorporating an sn 2 lipase-labile fumagillin prodrug for photoacoustic neovascular imaging and treatment". Theranostics, 5(2), 124, 2015.

14. **R. Zhang**, L. Wang, J. Yao, C. Yeh, L. V. Wang. *"In vivo* optically encoded photoacoustic flowgraphy*"*. Opt. Lett. 39(13), 3814-3817, 2014.
15. **R. Zhang**, J. Yao, K. I. Maslov, L. V. Wang. "Structured-illumination photoacoustic Doppler flowmetry of axial flow in homogenous scattering media". Appl. Phys. Lett. 103, 094101, 2013.
16. L. Wu, X. Cai, K. Nelson, W. Xing, J. Xia, **R. Zhang** and et al. "A green synthesis of carbon nanoparticles from honey and their use in real time photoacoustic imaging". Nano Research, 6(5), 312-325. (***Front cover article, highlighted***)
17. J. Zhao, G. Zheng, S. Li, H. Zhou, Y. Ma, **R. Zhang**, Y. Shi, P. He. "A hyperlens-based device for nanoscale focusing of light". 10(4), Chinese Optics Letters, 042302 (2012).
18. G. Zheng, **R. Zhang**, S. Li, P. He, H. Zhou, *"*Focusing beam beyond the diffraction limit using a hyperlens-based device*"*. Chinese Physics B, 20, 117802, 2011.
19. G. Zheng, **R. Zhang**, S. Li, P. He, H. Zhou, J. Yang, Y. Shi, *"*A hyperlens-embedded solid immersion lens for beam focusing beyond the diffraction limit*"*, Photonics Technology Letters, IEEE, Vol. 23 (17), 2011.
20. **R. Zhang**, P. Zhou, X. Feng, S. Li, Q. Shu, *"*Rapid extraction of line-structured light stripe in a large field of view*"*, Journal of Applied Optics, Vol 31, No 3, pp. 432-436, May, 2010
21. X. Feng, **R. Zhang**, P. Zhou, S. Li, *"*Image analysis of high power semiconductor line-laser*"*, Laser Technology, Vol 34 (5), pp.624-627, 2010

FIRST-AUTHORED CONFERENCE PROCEEDINGS AND ABSTRACTS

1. **R. Zhang**, R. Bin, H. Rong, B. Raman, L. V. Wang, "In vivo photoacoustic imaging of odor-evoke neuronal signals in the drosophila model". Proc. SPIE, Photons Plus Ultrasound: Imaging and Sensing 2016. (Talk)
2. **R. Zhang**, T. T. Wong, C. Zhang, K. Maslov, L. Wang, R. Chen, D. Novack, R. Aft, Q. Zhou, L. V. Wang. "Margin analysis of biological specimens with photoacoustic microscopy". Proc. SPIE, Photons Plus Ultrasound: Imaging and Sensing 2015. (Talk)
3. **R. Zhang**, L. Wang, C. Zhang, L. V. Wang. "Label-free photoacoustic detection of macrophages". Proc. SPIE, Photons Plus Ultrasound: Imaging and sensing 2015. (Poster)
4. **R. Zhang**, J. Yao, K. I. Maslov, L. V. Wang. *"*Structured-illumination photoacoustic Doppler flowmetry of axial flow in homogeneous scattering media*"*. Proc. SPIE, Photons Plus Ultrasound: Imaging and Sensing 2014. (Talk)
5. **R. Zhang**, X. Cai, X. Yang, A. Senpan, J. S. Allen, G. Lanza, D. Pan, L. V. Wang. *"*Photoacoustic molecular imaging of angiogenesis using theranostic *αvβ3*-targeted copper nanoparticles incorporating a Sn 2 lipase-labile fumagillin prodrug*"*. Proc. SPIE, Photons Plus Ultrasound: Imaging and Sensing 2014. (Poster)

PATENT

- G. Zheng, **R. Zhang**, S. Li, P. He, H. Zhou, J. Yang, *"*A super-resolution plano-convex focusing lens based on metamaterials*"*, China Patent: CN202141822U. Feb., 8th, 2012.

PROFESSIONAL ACTIVITIES

- Reviewer for Applied Optics, NeuroImage, Biomedical Optics Express, Journal of Biophotonics, IEEE Transactions on Medical Imaging, Journal of Medical Imaging.
- Member of American Heart Association
- Member of SPIE and OSA